TU Delft

Delft University of Technology

Emission Modelling from a Multi-Fuel Dual Combustor Gas Turbine

Augusto Viviani Perpignan, André

DOI
10.4233/uuid:094af2d0-3fb0-4067-9706-888592d15760

Publication date
2020

Document Version
Final published version

Citation (APA)
Augusto Viviani Perpignan, A. (2020). *Emission Modelling from a Multi-Fuel Dual Combustor Gas Turbine*. [Dissertation (TU Delft), Delft University of Technology]. https://doi.org/10.4233/uuid:094af2d0-3fb0-4067-9706-888592d15760

Important note
To cite this publication, please use the final published version (if applicable).
Please check the document version above.

Copyright
Other than for strictly personal use, it is not permitted to download, forward or distribute the text or part of it, without the consent of the author(s) and/or copyright holder(s), unless the work is under an open content license such as Creative Commons.

Takedown policy
Please contact us and provide details if you believe this document breaches copyrights.
We will remove access to the work immediately and investigate your claim.

This work is downloaded from Delft University of Technology.
For technical reasons the number of authors shown on this cover page is limited to a maximum of 10.

Emission Modelling from a Multi-Fuel Dual Combustor Gas Turbine

Emission Modelling from a Multi-Fuel Dual Combustor Gas Turbine

Proefschrift

ter verkrijging van de graad van doctor
aan de Technische Universiteit Delft,
op gezag van de Rector Magnificus prof.dr.ir. T.H.J.J. van der Hagen
voorzitter van het College voor Promoties,
in het openbaar te verdedigen op
donderdag 5 maart 2020 om 10:00 uur

door

André AUGUSTO VIVIANI PERPIGNAN

Master of Science in Mechanical Engineering,
University of São Paulo, Brazil.

Dit proefschrift is goedgekeurd door de promotoren:

promotor	Dr. A. Gangoli Rao
promotor	Prof. dr. ir. P. Colonna

Samenstelling promotiecommissie bestaat uit:

Rector Magnificus	voorzitter
Dr. A. Gangoli Rao	Technische Universiteit Delft
Prof. dr. ir. P. Colonna	Technische Universiteit Delft

Onafhankelijke leden:

Dr. ir. J. van Oijen	Technische Universiteit Eindhoven
Prof. dr.-ing. C.O. Paschereit	Technische Universität Berlin, Duitsland
Dr. M. de Joannon	Consiglio Nazionale delle Ricerche, Italië
Prof. dr. ir. S. Klein	Technische Universiteit Delft
Prof. dr. ir. G. Eitelberg	Technische Universiteit Delft, reservelid

Overig lid:

Prof. dr. ir. D.J.E.M. Roekaerts TU Delft / TU Eindhoven

The research leading to these results has received funding from National Council for Scientific and Technological Development (CNPq), Brazil, under the Science without Borders program.

Key-words: Flameless Combustion, Chemical Reactor Networks, MILD Combustion, NO_x Formation

ISBN/EAN 978-94-6384-109-2

Published and distributed by André A. V. Perpignan
Email: andreperpignan@gmail.com

Cover design by Elisa A. Perpignan

Copyright © 2019 by André A. V. PERPIGNAN.

All rights reserved. No part of the material protected by this copyright notice may be reproduced or utilized in any form or by any means, electronic or mechanical, including photocopying or by any information storage and retrieval system, without the prior written permission of the author.

Printed in the Netherlands by Ridderprint BV

SUMMARY

Future transport and energy systems will still rely on gas turbines for energy conversion. The contribution of aviation to the emission of greenhouse gases and other pollutant species is predicted to increase in the near future, both in absolute quantities as well as relative to other sources. Despite historically being one of the greatest contributors to innovation and technology, the aeronautical industry has faced difficulties in implementing radical changes in aircraft configuration, engine architecture and fuel flexibility. Likewise, stationary gas turbines are predicted to be used in energy generation to compensate for the inherently intermittent solar and wind energy sources. This could be done with the utilization of unconventional fuels like hydrogen, biofuels or synthetic fuels. Therefore, gas turbines will play a major role in energy transition and gas turbine performance should be improved and their pollutant emissions decreased.

As an attempt to provide a comprehensive option for future civil aviation, an aircraft concept was developed in the EU-funded AHEAD (Advanced Hybrid Engines for Aircraft Development) project. The concept makes use of several promising features such as the multi-fuel blended wing body fuselage, the use of cryogenic fuels, the adoption of boundary layer ingestion and finally, the subject of this thesis, a dual combustor engine capable of burning two different fuels.

The dual combustor configuration involves having a (lean-premixed) main combustor followed by the high pressure turbine and subsequently by an Inter-Turbine Burner (ITB) before the low pressure turbine. An engine configuration with ITB is better suited to attain the Flameless Combustion (FC) regime as compared to other engine configurations. The FC combustion mode is characterized by well-distributed reaction zones with reduced temperature gradients, acoustic oscillations and NO_x emissions compared to conventional combustion.

The computational modelling performed in this thesis is focused on understanding the parameters that affect the formation of pollutant emissions and the prediction of these emissions in the ITB. The models were compared to data acquired on a laboratory scale ITB combustor. The emission behaviour of this scaled combustor is analysed using a joint Computational Fluid Dynamics (CFD) and Chemical Reactor Networks (CRN) approach. While the CFD was able to provide information regarding the flow field in the combustor, the CRN was built using the flow field from CFD to model and predict emissions. The CRN approach allowed the analysis of various NO_x formation pathways, indicating that the prompt NO_x was the dominant pathway in the combustor. Subsequently, five chemical reaction mechanisms were employed. All of them overpredicted NO_x emissions and the overprediction is likely to be caused by the prompt NO_x subset implemented

in these mechanisms. Higher temperature of reactants and operational pressures were also investigated. With an increase in temperature, the NO_x emissions were predicted to increase and NO_x emissions peaked at lower equivalence ratios. Operational pressure changed the trend of emissions with global equivalence ratio. The trend of NO_x emissions at leaner conditions was found to be similar to that of conventional combustors. However, it was found that the NO_x emissions drop with further increase in equivalence ratio due to suppression of the prompt NO_x production, as well as due to an increase in NO reburning. These trends highlight the differences between the emission behaviour of an ITB and that of a conventional combustion system.

Additionally, an investigation on the evolution of chemical species within the high pressure turbine section was conducted. Usually, the composition at the outlet of the combustion chamber is considered to be chemically "frozen". However, this assumption is not necessarily valid, especially with the increasing turbine inlet temperatures and operating pressures. Again, utilizing a combined CFD and CRN approach, simulations were performed to analyse the progress of NO_x and CO in the high pressure turbine. Simulations considering turbulence-chemistry interaction were performed utilizing the Eddy Dissipation Concept and were compared with a finite-rate chemistry approach without turbulence interaction. The results show that the stator can act as an extension of the combustion chamber and emissions continue to evolve in the turbine stator.

Lastly, in order to predict emissions from combustion systems better by facilitating the CFD-CRN approach, the present thesis explores an automatic CFD to CRN computational tool (AGNES – Automatic Generation of Networks for Emission Simulation). In this approach, a CFD solution with simplified chemistry is generated and its computational cells are subsequently clustered to form ideal reactors following user-defined criteria. The resulting CRN is then solved with a detailed chemical reaction mechanism. The capabilities of the clustering and CRN solving are explored with a test case related to FC. The test case used is a non-premixed burner based on jet mixing and fuelled with CH_4. Results show that the prediction of CO emissions was improved significantly with AGNES and are in good agreement with the experimental data. As for the NO_x emissions, the CFD-CRN results were capable of predicting the non-monotonic behaviour with equivalence ratio, which the CFD simulations were not able to capture. However, the agreement between experimental values and those predicted by CFD-CRN approach for NO_x was not fully satisfactory. The clustering criteria employed to generate the CRNs from the CFD solutions were shown to significantly affect the results, thereby suggesting that the NOx emissions is a non-linear function of clustering criteria. The work carried out in this thesis on the CFD-CRN approach indicates future opportunities in improving this multi-step procedure and its application in emission prediction of combustion systems.

SAMENVATTING

Toekomstige transport- en energiesystemen zullen nog steeds gebaseerd zijn op gasturbines voor de omzetting van energie. De voorspelling is dat de bijdrage van luchtvaart aan de uitstoot van broeikasgassen en andere vervuilende stoffen toeneemt in de nabije toekomst, zowel in absolute hoeveelheid als relatief tot andere vervuilende bronnen. Ondanks dat de luchtvaartindustrie historisch gezien veel heeft bijgedragen aan innovatie en technologische voortuitgang, ondervindt de sector uitdagingen omtrent het doorvoeren van radicale veranderingen aan de vliegtuigconfiguratie, het motorontwerp en de brandstof. Stationaire gasturbines zullen worden gebruikt voor energieopwekking om te compenseren voor de inherent fluctuerende zonne- en windenergiebronnen. Dit is mogelijk door onconventionele brandstoffen zoals waterstof, biobrandstoffen of synthetische brandstoffen te gebruiken. Daarom zullen gasturbines een belangrijke rol spelen in energieomzetting. Echter, de gasturbine prestaties moeten worden verbeterd, terwijl hun schadelijke uitstoot moet worden verminderd.

In een poging een uitgebreide optie voor de toekomstige civiele luchtvaart te leveren, is een vliegtuigconcept ontwikkeld binnen het, door de EU gefinancieerde, AHEAD (Advanced Hybrid Engines for Aircraft Development) project. Het vliegtuigconcept omvat enkele veelbelovende kenmerken zoals een blended wing body met meerdere brandstoffen, waaronder cryogene brandstoffen, het gebruik van boundary layer ingestion en tot slot het onderwerp van deze thesis: een motor met een dubbele verbrander die in staat is met twee verschillende brandstoffen te werken.

De configuratie met dubbele verbrander heeft een (lean-premixed) hoofdverbrander, gevolgd door een hogedruk turbine en vervolgens een inter-turbine verbrander (ITB) voor de lagedruk turbine. Een motorconfiguratie met ITB is meer geschikt om vlamloze verbranding (FC) te bewerkstelligen dan andere motorconfiguraties. De vlamloze verbranding wordt gekenmerkt door goed verdeelde reactiezones met gereduceerde temperatuurgradiënten, akoestische oscillaties en NOx uitstoot, in vergelijking met conventionele verbranding.

In deze thesis is numerieke modellering uitgevoerd, gefocust op het begrijpen van de parameters die de formatie van vervuilende uitstoot beïnvloeden en het voorspellen van deze uitstoot in de ITB. De modellen zijn vergeleken met data verkregen uit een laboratoriumschaal ITB. Het uitstootgedrag van deze geschaalde verbrander is geanalyseerd met een combinatie van numerieke stromingsleer (CFD) en Chemical Reaction Networks (CRN). Terwijl CFD in staat was om informatie omtrent het stromingsveld in de verbrander te leveren, is het CRN gebouwd op basis van het stromingsveld uit CFD om de uitstoot te modelleren en voorspellen. De CRN aanpak maakte het mogelijk

de verschillende mogelijkheden van NOx formatie te analyseren, wat aantoonde dat prompt NOx dominant is in de verbrander. Vervolgens zijn vijf chemische reactiemechanismen gebruikt. Allemaal overschatten ze de NOx uitstoot en die overschatting wordt waarschijnlijk veroorzaakt door het prompt NOx deel dat in deze mechanismen is geïmplementeerd. Hogere temperaturen van de reactanten en operationele druk zijn ook onderzocht. Met een toename in temperatuur werd ook een toename in de NOx uitstoot voorspeld en de NOx uitstoot had een piek bij lagere equivalence ratios. De operationele druk veranderde de trend van de uitstoot met de globale equivalence ratio. De trend van NOx uitstoot bij armere condities bleek vergelijkbaar met die van conventionele verbranders. Daarentegen bleek dat de NOx uitstoot daalt met een verdere toename in equivalence ratio door de onderdrukking van de prompt NOx productie, alsmede een toename in herverbranding van NO. Deze trends benadrukken de verschillen tussen het uitstootgedrag van een ITB en die van een conventioneel verbrandingssysteem.

Daarnaast is een onderzoek naar de ontwikkeling van chemische stoffen in de hogedruk turbine sectie uitgevoerd. Normaal gesproken wordt de compositie bij de uitlaat van de verbrandingskamer als chemisch “bevroren” beschouwd. Echter, deze aanname is niet per se valide, vooral met de toenemende turbine inlaat temperaturen en operationele druk. Weer gebruik makend van de combinatie van CFD en CRN zijn er simulaties uitgevoerd om de ontwikkeling van NOx en CO in de hogedruk turbine te analyseren. Simulaties die de turbulentie-chemie interactie in rekening nemen werden uitgevoerd met het Eddy Dissipation Concept en vergeleken met een eindige-reactiesnelheid aanpak zonder de interactie met turbulentie. De resultaten laten zien dat de stator als verlenging van de verbrandingskamer kan dienen en dat de uitstoot zich blijft ontwikkelen in de stator van de turbine.

Tot slot, om beter in staat te zijn de uitstoot van verbrandingssystemen te voorspellen door middel van de CFD-CRN aanpak, wordt in deze thesis een automatische omzetting van CFD naar CRN door middel van een computer methode onderzocht (AGNES – Automatic Generation of Networks for Emission Simulation). In deze benadering wordt een CFD oplossing met versimpelde chemie gegenereerd en de rekencellen worden vervolgens gegroepeerd om ideale reactoren te vormen die voldoen aan door gebruikers bepaalde criteria. Het resulterende CRN wordt opgelost met een gedetailleerd chemische reactiemechanisme. De mogelijkheden van het groeperen en oplossen van de CRN zijn uitgezocht met een test casus gerelateerd aan FC. De test casus maakte gebruik van een non-premixed verbrander gebaseerd op jet mixing en gevoed met methaangas. Resultaten laten zien dat de voorspelling van de CO uitstoot aanzienlijk verbeterde met AGNES en in overeenstemming is met experimentele data. Wat betreft de NOx uitstoot, waren de CFD-CRN resultaten in staat om het niet-monotone gedrag met equivalence ratio te voorspellen, wat de CFD simulaties niet konden vastleggen. Desalniettemin was de overeenkomst tussen de experimentele

waardes en die voorspeld door de CFD-CRN methode voor NOx niet heel bevredigend. Het is aangetoond dat de gebruikte groeperingscriteria om de CRNs uit de CFD resultaten te genereren een grote invloed hadden op de resultaten, wat suggereert dat de NOx uitstoot een niet-lineaire functie is van de groeperingscriteria. Het werk omtrent de CFD-CRN methode dat is uitgevoerd in deze thesis geeft aan dat er toekomstige kansen zijn om deze procedure en de toepassing ervan in de uitstootvoorspelling van verbrandingssystemen te verbeteren.

Contents

Summary v

Samenvatting vii

Nomenclature xv

Acronyms xv
Latin Symbols xvi
Greek Symbols xvii
Subscripts xviii
Superscripts xix

List of Figures xx

List of Tables xxviii

Chapter 1 Introduction 1

1.1 The role of aviation in climate change and pollution 1
1.2 Reducing aviation's and gas turbines environmental impact 2
1.3 Thesis structure and objectives 6

Chapter 2 Flameless Combustion 9

2.1 Definition of Flameless Combustion 9
2.2 Conceptual Designs for Gas Turbine FC Combustors 16
2.3 Summary 29

Chapter 3 Computational Modelling of Combustion and Emissions 31

3.1 Introduction 31
3.2 Combining CFD and CRN 33
3.3 CFD Models 34
3.3.1 Eddy Dissipation Model 35
3.3.2 Flamelet Generated Manifolds 35
3.3.3 Eddy Dissipation Concept 36

3.4 Chemical Reactor Networks 37
Chapter 4 The Dual Combustor System 39
4.5 The Lean-Premixed Combustor 41
4.6 The High-Pressure Turbine 44
4.7 The Inter-Turbine Burner 44
Chapter 5 Emissions along the High Pressure Turbine 45
5.1 Introduction 45
5.2 Test Case Geometry 47
5.3 Numerical Modelling Setup and Validation 47
5.3.4 Computational Fluid Dynamics 47
5.3.5 Operating Conditions and Calculation of Initial Composition 50
5.3.6 Chemical Reactor Network 51
5.4 Results and Discussion 53
5.4.1 NO_x Chemistry 54
5.4.2 CO Chemistry 58
5.4.3 Overall Observations 61
5.5 Conclusions & Recommendations 61
Chapter 6 Analysis of the Inter-Turbine Burner 63
6.1 Introduction 63
6.2 Combustor Experiments 65
6.3 Computational Modelling Objectives 69
6.4 CFD Simulations 70
6.4.1 Flow Field Analysis 71
6.5 Chemical Reactor Network of the ITB 76
6.6 Comparison between CFD and CRN 78
6.7 NO_x Formation Analysis 81
6.8 Suggested ITB Design Modifications 83

6.9 Considerations & Conclusions 84
Chapter 7 Effects of Operating Conditions on the ITB Emissions 87
7.1 Chemical Kinetics under the FC Regime 87
7.2 Four-reactor CRN 89
7.2.1 Four-Reactor CRN Results and Limitations 90
7.3 Effects of Different Chemical Reaction Mechanisms 92
7.4 Effect of Different Operating Conditions 94
7.5 Overall Comments 96
7.6 Conclusions 97
Chapter 8 Automatic CRN Generation 99
8.1 Introduction 99
8.2 The Test Case 101
8.3 Computational Modelling 103
8.3.1 Computational Fluid Dynamics 104
8.3.2 Chemical Reactor Networks 106
8.4 Results 109
8.4.1 CFD Results 109
8.4.2 AGNES Results 115
8.5 Conclusions & Recommendations 122
Chapter 9 Conclusions and Recommendations 125
9.1 Conclusions 125
9.2 Recommendations 127
Appendix A Deactivated Reactions to Calculate NO_x Formation Pathways Contributions 129
A.1 GRI 2.11 129
A.2 GRI 3.0 130
A.3 Konnov 131
A.4 GDF-Kin ® 3.0 134

A.5 POLIMI C1C3HT 135
Bibliography 137
Acknowledgements 151
Publications Related to this Thesis 153
Curriculum Vitae 154

NOMENCLATURE

ACRONYMS

ACARE	Advisory Council for Aviation Research and Innovation in Europe
AGNES	Automatic Generation of Networks for Emission Simulation
AHEAD	Advanced Hybrid Engines for Aircraft Development
BFS	Breadth First Search
CFD	Computational Fluid Dynamics
CMC	Conditional Momentum Closure
CRN	Chemical Reactor Network
CSE	Conditional Source-term Estimation
DNS	Direct Numerical Simulation
EDC	Eddy Dissipation Concept
EDM	Eddy Dissipation Model
EGR	Exhaust Gas Recirculation
FC	Flameless Combustion
FGM	Flamelet Generated Manifolds
FLOX	Flameless Oxidation
FPVA	Flamelet/Progress Variable Approach
FRC	Finite Rate Chemistry
GHG	Greenhouse Gases
GT	Gas Turbine
HPT	High-Pressure Turbine
ICAO	International Civil Aviation Organization
IPCC	International Panel on Climate Change
ITB	Inter-Turbine Burner
LDI	Lean Direct Injection
LES	Large-Eddy Simulation
LTO	Landing and Take-Off
NASA	National Aeronautics and Space Administration

NG	Natural Gas
OPR	Overall Pressure Ratio
PaSR	Partially Stirred Reactor
PDF	Probability Density Function
PFR	Plug Flow Reactor
PLIF	Planar Laser-Induced Fluorescence
PSR	Perfectly Stirred Reactor
PVA	Principal Variable Analysis
RANS	Reynolds-averaged Navier-Stokes
RQL	Rich-Burn, Quick-Quench, Lean-Burn
SST	Shear-Stress Transport
TIT	Turbine Inlet Temperature
TVC	Trapped Vortex Combustor

LATIN SYMBOLS

A	Area of the defined surface for calculating the recirculation ratio [m^2]
C	Stoichiometric coefficient [-]
C_τ	Eddy Dissipation Concept model constant [-]
C_γ	Eddy Dissipation Concept model constant [-]
c	Progress variable [-]
ch	Stator vane chord [m]
c_p	Specific heat capacity at constant pressure [J/gK]
c_v	Specific heat capacity at constant volume [J/gK]
D	Diameter [m]
Da	Damköhler number [-]
E	Activation energy [J]
f	Mixture fraction [-]
h	Specific enthalpy [J/kg]
Ka	Karlovitz number [-]
k	Turbulent kinetic energy [m^2/s^2]

l_t	Turbulence length scale [m]
M	Molar mass [kg/mol]
m	Mass [kg]
$\dot{m}$	Mass flow [kg/s]
$\mathbf{N}$	Unit vector normal to the area
p	Pressure [Pa]
Q	Heat of combustion [J]
$\dot{Q}$	Heat flux [W]
R	Reaction rate [kg/m^{3}s]
Re	Reynolds number [-]
RR	Recirculation ratio [-]
r	Radial coordinate [m]
S	Source-term [kg/m^{3}s]
s	Flame speed [m/s]
T	Temperature [K]
t	Time [s]
U	Total internal energy [J]
u	Specific internal energy [J/kg]
u'	Velocity fluctuation [m/s]
$\mathbf{V}$	Velocity vector
V	Reactor volume [m^3]
w	Axial velocity [m/s]
x	Axial position in the HPT stator [m]
Y	Mass fraction [-]
z	Axial coordinate [m]

GREEK SYMBOLS

α	Diffusivity [m^2/s]
γ	Ratio of specific heats [-]
γ_λ	Turbulent fine scales length fraction [-]

δ	Flame thickness [m]
ε	Turbulent dissipation rate [m^2/s^3]
η_V	Vane efficiency [-]
θ	Generic CFD variable treated by AGNES [-]
μ	Tolerance for AGNES clustering [-]
υ	Kinematic viscosity [m^2/s]
ξ	Range of a given quantity for AGNES clustering [-]
ρ	Density [kg/m3]
τ	Chemical Time scale [s]
τ_t	Turbulence time scale [s]
ϕ	Global equivalence ratio [-]
χ	Scalar dissipation rate [1/s]
ω	Rate of turbulent kinetic energy dissipation [1/s]

SUBSCRIPTS

0	Turbine inlet
1	Stator outlet
ent	Entering the reactor
F	Fuel
I	Ignition
i	Chemical species
in	Reactants
L	Laminar flame
loc	Local
out	Leaving the reactor
oxid	Oxidiser
prod.	Products
Q	Quenching
r	Reaction
reac.	Reactants
S	Static

T	Integral scale
To	Total
tr	Transport scale

SUPERSCRIPTS

*	Non-dimensional
$'$	Fine turbulence structures
eq	Chemical equilibrium
u	Unburnt reactants

LIST OF FIGURES

Figure 1.1: Percentage of direct annual GHG global emissions measured in CO_2 equivalent per sector in 2010. Data from Blanco et al. [13]. 2

Figure 1.2: Variation of overall pressure ratios and NO_x emissions index for aero engines over time. Data from ICAO Aircraft Engine Emissions Databank [19]. Representation of the ACARE Goal for 2050 [20]. 3

Figure 1.3: Schematics of some of the existing and proposed combustor concepts for gas turbines. 4

Figure 1.4: Outline of the thesis. 7

Figure 2.1: Combustion regimes diagram proposed by Rao and Levy [34]. 10

Figure 2.2: The S-shaped curve displaying ignition (I) and quenching (Q). The ordinate axis (reaction rate) can be also expressed in $T*.Da$ is the Damköhler number. 11

Figure 2.3: Calculated regions where the FC regime occurs in relation to reactants temperature (Tin), molar concentration of O_2 in the oxidiser, and equivalence ratio (Φ) according to the definitions of Caveliere and de Joannon [30], Oberlack et al. [35], and Evans et al. [33]. 13

Figure 2.4: Combustion regime diagrams for premixed flames (left) and for non-premixed flames, based on the diagrams proposed by Borghi [41], Peters [42] and Law [43]. If the FC regime is considered related to distributed reaction zones, the regions highlighted by the dashed lines are relevant for the regime. 14

Figure 2.5: Species emission results of CO and NO_x of a FLOX® setup as functions of the equivalence ratio for three different jet velocities. Adapted from Lückerath [61]. The vertical axis was split to aid visualization and clearly show the low emissions window. 19

Figure 2.6: FLOX® combustor employed by Sadanandan et al. [65] and the two nozzle configurations.....20

Figure 2.7: The configurations of the partially premixed nozzles studied by Schütz et al. [66] in the EZEE® concept.....21

Figure 2.8: The 8-nozzle square-shaped FLOX® combustor employed by Gounder et al. [72] to study fuel spray characteristics. Top view (left) and lateral view (right). 22

Figure 2.9: Cross-section of the 60º sector employed by Melo et al. [81]. .24

Figure 2.10: The concept proposed by Levy et al. [83]. The numbers refer to the regions simulated in their analyses. 25

Figure 2.11: The FOGT concept [84]. 25

Figure 2.12: The engine concept present along with the AHEAD project [86]. 26

Figure 3.1: Schematic of the most used approaches for modelling FC in relation to turbulence, chemistry, turbulence-chemistry interaction, and computational costs. 32

Figure 4.1: The aircraft concept developed by the AHEAD project [18]. ..39

Figure 4.2: The hybrid dual combustor engine. Courtesy of Pratt and Whitney Rzeszów S.A., Copyright 2014. 40

Figure 4.3: Engine concept with an inter-turbine burner. Courtesy of Pratt and Whitney Rzeszów S.A., Copyright 2014. 41

Figure 4.4: Geometry of the burner employed for the experiments carried out by Reichel et al. [115]. 42

Figure 4.5: Mean OH signal for different values of ϕ and fuel momentum (J) [115]. 42

Figure 4.6: Schematic of the CRN employed to estimate the composition of the gases leaving the lean-premixed combustor. 43

Figure 4.7: Comparison between experimental [118] and calculated values of NO_x for the lean-premixed H_2 combustor for two different reactants temperatures. 43

Figure 5.1: Fully hexahedral computational mesh of the a stator blade passage employed for the CFD simulations.....48

Figure 5.2: Comparison of isentropic Mach number at three different blade spans between experimental [127] and CFD values.....49

Figure 5.3: Comparison between experimental [127] and CFD values of vane efficiency at a plane located 10.16 mm downstream of the vane trailing edge. 49

Figure 5.4: Profiles of cross-sectional area, static pressure, temperature and density imposed to the CRN for conditions A and B (cruise). 52

Figure 5.5: Temperature contours for a simulation without chemical reactions (above) and an EDC simulation (below) for condition A. 54

Figure 5.6: Cross-sectional average of NO mass fraction for condition A (cruise, H_2) calculated utilizing the CFD model with different chemical reaction mechanisms and chemistry modelling. 55

Figure 5.7: NO mass fraction contours in ppm for condition A with the FRC approach and the San Diego mechanism. A top view plane (above) and an axial plane (below). 56

Figure 5.8: NO mass fractions for condition A (cruise, H_2) calculated utilizing the CRN model with three different chemical reaction mechanisms. 57

Figure 5.9: Mass-averaged NO mass fractions as functions of the axial location. 57

Figure 5.10: NO mass fraction contours in ppm for condition C with the EDC approach and the POLIMI H_2CO mechanism. 58

Figure 5.11: CO mass fractions for condition B calculated utilizing the CFD model with FRC and the EDC. 59

Figure 5.12: CO mass fraction contours in ppm for condition B with the EDC approach and the POLIMI H_2CO mechanism. The maximum CO mass fractions can be seen in the boundary layer of the blade. 60

Figure 5.13: CO mass fractions for conditions C and D calculated utilizing the CFD model with the EDC, and the CRN model. 60

Figure 6.1: Geometry of the 18-degree combustor sector employed in the experiments. Geometry is cut in half along the longitudinal axis, with the quartz window depicted in blue [138]. 66

Figure 6.2: Photographs of the combustor for different amounts of N_2 addition [138]. For 0 LPM, 40 LPM and 100 LPM steps (from a to c). Fuel mass flow of $5.91 \cdot 10^{-5}$ kg/s. The incandescent filament on the right-hand-side is a thermocouple. Please note that the photographs are meant for visual representation only. 67

Figure 6.3: Experimental results of NO_x and CO emissions with a variation of global equivalence ratio A (values of local equivalence ratio also indicated), N_2 addition to the oxidiser B, and H_2O addition to the oxidiser C. [derived from 138].....68

Figure 6.4: Variation in the emissions with mesh density (results for 2.1 million elements as reference). Data points in red indicate the utilized mesh. 70

Figure 6.5: Computational mesh. Side view (left) and fuel injection region (right). 71

Figure 6.6: Temperature field with ϕ = 0.235. Non-adiabatic CFD simulations.....72

Figure 6.7: Example of a defined surface for the calculation of the recirculation ratio for the case with ϕ = 0.254. Velocity vectors on the central plane of the combustor. The dot depicts the centre of the recirculation zone, where velocity is equal to zero. Isometric (left) and lateral (right) views...73

Figure 6.8: Recirculation ratio and local recirculation ratio as functions of the global equivalence ratio.....74

Figure 6.9: Calculated Da for the without nitrogen addition (left), with 80 LPM N_2 addition (middle) and 100 LPM (right). Lateral (up) and isometric (down) views. Non-adiabatic CFD simulations. 75

Figure 6.10: The O_2 mass fraction for two different equivalence ratios with no air dilution. ϕ = 0.165 (left) and ϕ = 0.235 (right). Isometric view. Non-adiabatic CFD simulations. 75

Figure 6.11: Regions of the inter-turbine combustor divided into idealized reactors in the designed CRN. 76

Figure 6.12: Structure of the designed CRN. 77

Figure 6.13: CO emissions as a function of the global equivalence ratio. Comparison between experimental data [121] and modelled results. 78

Figure 6.14: NO_x emissions as a function of the global equivalence ratio. Comparison between experimental data [121] and modelled results. 79

Figure 6.15: CO emissions as a function of N_2 addition to the oxidiser. Fixed fuel and air mass flow. Comparison between experimental data [138] and modelled results.....80

Figure 6.16: NO_x emissions as a function of N_2 addition to the oxidiser. Fixed fuel and air mass flow. Comparison between experimental data [138] and modelled results.....80

Figure 6.17: Relative (left) and absolute (right) contributions of NO_x formation pathways for different global equivalence ratios. Results from the CRN model with the GRI 2.11 mechanism. 81

Figure 6.18: Prompt NO_x emissions and the C/O mass ratio (excluding H_2O and CO_2) for the Combustion PSRs as functions of the global equivalence ratio using the GRI 2.11 mechanism. 82

Figure 6.19: The mass fractions of HCN and CH in the Combustion 1 (left) and Combustion 2 (right) PSRs as a function of the global equivalence ratio, using the GRI 2.11 mechanism. 83

Figure 6.20: Dimensions that can be modified in order to improve the combustor design. 84

Figure 7.1: Measured NO_x emissions as a function of the equivalence ratio for three different systems with high recirculation: a combustion chamber with jet-induced stabilization [62], the ITB, and a cyclonic prismatic chamber for two different estimated residence times [154]. The values related to the ITB are plotted as a function of the local equivalence ratio, and not of the global equivalence ratio, as defined in Section 6.2. 88

Figure 7.2: Scheme of the CRN designed to investigate the effect of recirculation of products in the behaviour of NO_x emissions. 89

Figure 7.3: NO_x emissions as a function of RR for the four-reactor CRN. Four different ϕ. Mean residence time = 0.12 s. T_{in} = 600 K. 90

Figure 7.4: NO_x emissions as a function of ϕ for the four-reactor CRN, three different reactor volume settings. Values of residence time shown in seconds for each data-point. T_{in} = 600 K. RR = 0.2. 91

Figure 7.5: NO_x emissions as a function of the global equivalence ratio for various chemical reaction mechanisms. 93

Figure 7.6: Total NO_x emissions and relative prompt NO_x contribution as functions of global equivalence ratio for various Tin. 95

Figure 7.7: NO_x emissions as a function of the global equivalence ratio for various operational pressure values of the ITB CRN. Dashed lines represent the values obtained when considering the correlation of Eq. 7.2. 96

Figure 8.1: Mean OH* images for diverse global equivalence ratio values. From left to right, $\phi \cong 0.91, 0.77, 0.67, 0.59, 0.53, 0.48$ (above). Emissions of NO_x and CO in dry volumetric ppm adapted from Veríssimo et al. [62] (below).....102

Figure 8.2: Hexahedral mesh employed for CFD simulations. 105

Figure 8.3: Flowchart of the calculation procedure implemented in AGNES. 107

Figure 8.4: Experimental and CFD temperature results along the centreline of the combustor (above) and temperature contour plots (below) for condition b ($\phi \cong 0.77$) using FGM and EDM. Error bars represent experimental uncertainty. 110

Figure 8.5: Experimental and CFD temperature results along the axial line where r = 45 mm for conditions b ($\phi \cong 0.77$) and d ($\phi \cong 0.59$). Error bars represent experimental uncertainty.....111

Figure 8.6: Experimental and CFD results along the centreline of the combustor for O_2 and CO_2 concentrations for conditions b ($\phi \cong 0.77$) and d ($\phi \cong 0.59$). Error bars represent experimental uncertainty. 111

Figure 8.7: Comparisons of experimental and CFD (FGM) parameters: temperature, O_2 concentration, and CO_2 concentration results along radial lines for condition b ($\phi \cong 0.77$). Error bars represent experimental uncertainty. 113

Figure 8.8: Comparisons of experimental and CFD (FGM) parameters: temperature, O_2 concentration, and CO_2 concentration results along radial lines for condition d ($\phi \cong 0.59$). Error bars represent experimental uncertainty. 114

Figure 8.9: Outlet CO and NO results from CFD performed with FGM compared with experimental values. CO values come from tabulated FGM calculations. NO values come from the transported NO calculation.....115

Figure 8.10: Outlet CO results from AGNES compared with experimental results. Different input simulations for AGNES (FGM or EDM) and post-processing options (GRI 3.0 or GRI 2.11, as well as clustering criteria). Error bars represent experimental uncertainty. 116

Figure 8.11: Outlet NO_x results from AGNES having CFD simulations performed with EDM as input compared with experimental results. 116

Figure 8.12: Outlet NO_x results from AGNES having CFD simulations performed with FGM as input compared with experimental results. Two different clustering criteria sets. Error bars represent experimental uncertainty. 117

Figure 8.13: Reactors on a plane of the combustor for condition b ($\phi \cong 0.77$). Reactors clustered utilizing T, velocity direction, H_2O and CH_4 (above), and T, velocity direction, H_2O, CH_4 and O_2 (below). Each PSR is represented by a dot located at its centre. The colour scale is arbitrary and was generated based on reactor numbers attributed during the clustering. 118

Figure 8.14: NO_x values at selected local profiles. Comparison between experimental data and AGNES results obtained using an FGM simulation as input, GRI 2.11 and T, velocity direction, Y_{H2O}, Y_{CH4}, and Y_{O2} as clustering criteria for condition b ($\phi \cong 0.77$). Error bars represent experimental uncertainty. 119

Figure 8.15: NO formation rates at r = 15 mm along the axial direction for the different formation pathways. Values presented for conditions a ($\phi \cong 0.91$), b ($\phi \cong 0.77$), and e ($\phi \cong 0.53$).....121

LIST OF TABLES

Table 1.1: Qualitative comparison of different combustor types and their potential. 5

Table 2.1: Comparison of requirements and operational aspects between aero engines and land-based gas turbines 17

Table 5.1: Stator vane geometry as described by Timko [127]. 47

Table 5.2: Operating conditions investigated and their resulting turbine inlet conditions. 51

Table 5.3: Simulations performed to each of the considered conditions 53

Table 7.1: Results for the different chemical reaction mechanisms across the investigated equivalence ratios with respect to prompt NO_x contribution and deviation from experiments. 94

Table 8.1: Operating conditions investigated by Veríssimo et al. [62]. 103

Chapter 1 Introduction

Climate change along with the pollution and degradation of the environment is possibly the biggest challenge for mankind. The projected consequences of climate change include the rise in mean temperatures, non-uniform changes in precipitation, reduction in ice sheets and glaciers, and rise of sea levels [1]. Subsequently, these changes are predicted to cause disastrous consequences: increased extinction risks for many species, undermining of food security due to inviable crops in some areas, limitation of water availability, flooding of coastal areas, and extreme climate events.

The overwhelming scientific consensus that global warming is caused by human activity [2] calls for actions. The emission of greenhouse gases (GHG) has to be reduced in order to limit the temperature increase and, thereby, its consequences. In December of 2015, the signing of the Paris Agreement [3] marked the compromise of nations to pursue reductions of GHG emissions. The goal of the agreement was to maintain the mean global temperature rise below 2° C in this century when compared to pre-industrial values. Recently, the IPCC released a report supporting the engagement on maintaining the rise below 1.5° C. This would significantly reduce the severity of extreme climate events (precipitation, floods and droughts), the range of regional extreme temperatures, the damage to wetlands and coral reef ecosystems, the risks of local species extinctions, the probability of sea-ice-free Arctic summers, and the sea level rise by 0.1 m [4]. This report and a great body of scientific publications reassure the urgency of reducing GHG emissions.

1.1 THE ROLE OF AVIATION IN CLIMATE CHANGE AND POLLUTION

The attribution of GHG emissions and contribution to climate change per sector is a challenging task, as it is dependent on numerous assumptions to account for indirect emissions and to calculate their equivalent impact. According to the estimates published by the IPCC [1], the direct contribution of the transport sector is approximately 14% of the total GHG CO_2 equivalent emissions (see Figure 1.1).

The relative contribution is, however, dependent on how calculations are performed for every other sector and how sectors are separated. The contribution of transport was pointed to be as high as 24% when considering fuel combustion and CO_2 only [5], or as low as 10 to 11%, when agriculture's impact is calculated taking land use, fuel, and fertiliser production into account [6,7]. In the European context, the transportation sector was responsible for 31.6% of all GHG emissions [8].

The assessment of the contribution of aviation has complications due to the chemistry of the non-CO_2 species emitted, the difficulty in predicting and quantifying

Contents of this chapter appeared in:

Perpignan AAV, Rao AG, Roekaerts DJEM. *A review of Flameless Combustion and its potential towards gas turbines*. Progress in Energy and Combustion Sciences 2018;69:28-62.

the contribution of contrails and induced cirrus clouds, as well as the various altitude where the emissions occur [9]. The calculation, usually performed by estimating the radiative forcing of each chemical species, shows that the emission of nitrogen oxides (NO_x) increases the net radiative forcing via the production of ozone, despite the fact that it has a reducing effect via the decrease of methane [10]. Similarly, the sulphate aerosol emitted by aircraft engines has a negative radiative forcing. The contribution of contrails and induced cirrus clouds are difficult to measure due to the complexity of the formation mechanisms and the dependence on several parameters, as contrail coverage, optical depth, and ice-supersaturation in the atmosphere [9,11]. These examples show how arriving at a precise quantification of aviation's contribution is challenging. Owen et al. [12] estimated that aviation was responsible for 4.9% of all radiative forcing in 2005.

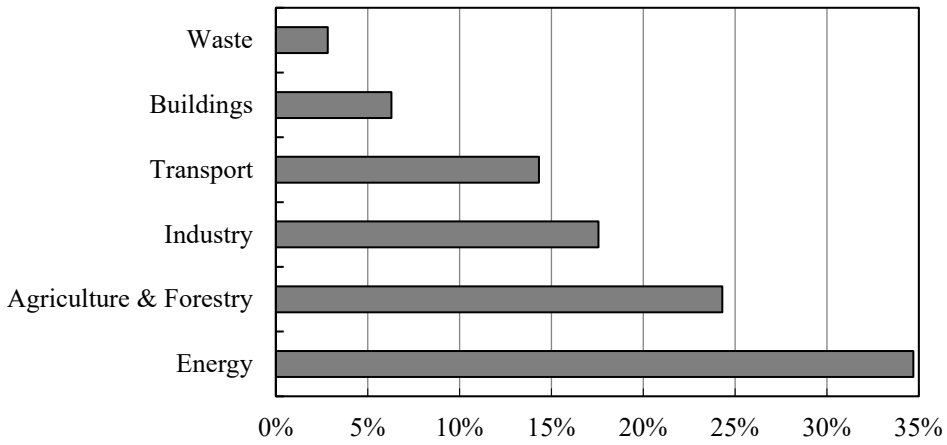

Figure 1.1: Percentage of direct annual GHG global emissions measured in CO_2 equivalent per sector in 2010. Data from Blanco et al. [13].

Despite the uncertainty involved, it is clear that the contributions of the transport sector and aviation are relevant, especially considering that aviation is predicted to grow massively in the coming years [14]. Emissions of CO_2 by international aviation were predicted to grow by 144% between 2005 and 2025 [15] and the increase in aviation CO_2 emissions in China, for example, is projected to be 3.9% per year from 2013 till 2030 [16]. Given the gravity of the scenario and how challenging it is to reduce to the required extent, we should aim at reductions in every possible sector.

1.2 Reducing aviation's and gas turbines environmental impact

Modern aviation relies mostly on gas turbines (GTs) for propulsion. It is important to highlight that GTs play an important role, both in the transport and energy sector. Even though sustainable energy sources and storage systems are increasingly becoming more important, alternatives to combustion in aviation are still

underdeveloped and will not become feasible solutions in commercial aircraft for the next decades due to the extremely low energy density of batteries [17].

The trends and goals in aviation engines are paradoxical in relation to NO_x emissions. Turbine inlet temperatures (TIT) and overall pressure ratios (OPR) have been increasing over time in the pursuit of increasing thermal efficiency and thereby reducing the fuel consumption and CO_2 emissions [18]. However, NO_x emissions have to be reduced, and they have a tendency to increase with both TIT and OPR.

The data displayed in Figure 1.2 shows the trend of increasing OPR over time and the corresponding NO_x emission index. In order to lower or maintain NO_x emissions while increasing OPR and TIT, new combustion technologies have been and still have to be developed, as the different decades portrayed in Figure 1.2 show. According to the goals set by the Advisory Council for Aviation Research and Innovation in Europe (ACARE), the NO_x emission levels in 2050 should be only 10% when compared to a baseline aircraft of year 2000 [20].

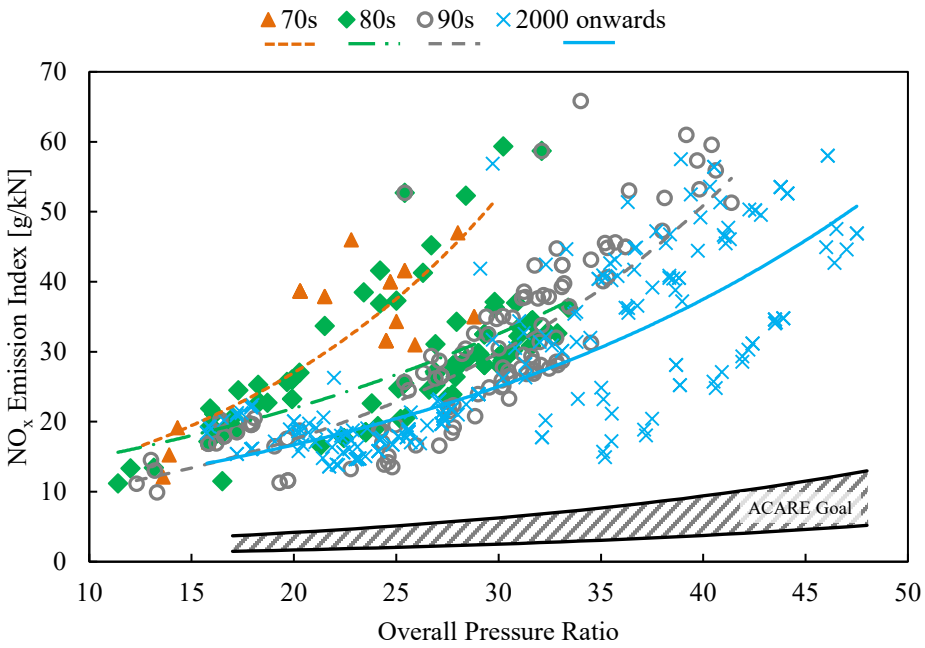

Figure 1.2: Variation of overall pressure ratios and NO_x emissions index for aero engines over time. Data from ICAO Aircraft Engine Emissions Databank [19]. Representation of the ACARE Goal for 2050 [20].

Pollutant emissions regulations for land-based GTs differ significantly in relation to that of aero engines because of their interaction with the systems operating at power plants and the larger variety in terms of power output, fuels and usage (mechanical drive or electricity). A summary of existing regulations in different countries was presented by Klein [21]. Regardless of the differences, the regulatory pressures on

land-based GTs have also been a concern to designers and operators. Emission regulations for NO_x and CO have been increasingly stringent, while greenhouse gases taxation and emission trading schemes have already been introduced in some countries.

Although the current trend in electricity generation is to shift towards sustainable and renewable energy conversion methods, land-based GTs are far from becoming obsolete. GTs are pointed as one of the solutions to be employed along with wind or solar [22] energy systems to deal with the inherent intermittency of these energy sources [23]. Energy storage in the form of fuels and the decoupling of the compression and expansion cycles of gas turbines with compressed air energy storage are regarded as feasible approaches in combined cycle power plants based on wind or solar energy [24].

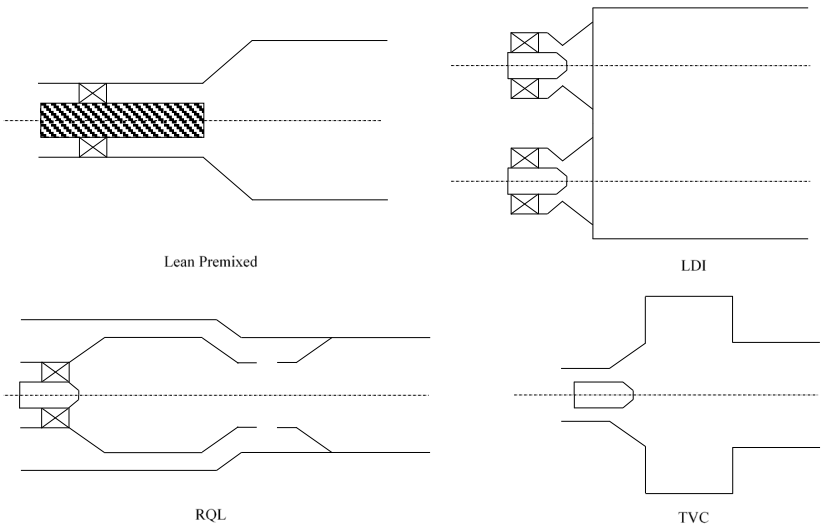

Figure 1.3: Schematics of some of the existing and proposed combustor concepts for gas turbines.

Consequently, research and development have been focused on options that minimize the environmental impact of GT combustion while retaining high efficiencies. Broadly, it may be achieved by using alternative fuels, improving current combustor designs, or adopting new combustion concepts. The latter is arguably the most complex alternative but has more potential for providing significant improvements.

A few approaches have been investigated and attempted as new combustion concepts for aeronautical GTs, such as the Trapped Vortex Combustor (TVC) and Lean Direct Injection (LDI), as shown in Figure 1.3. The TVC concept aims to improve stabilization and mixing by imposing vortical structures to the flow in

cavities of the combustion chamber. The LDI concept is based on quickly vaporizing and mixing liquid fuel sprays in order to create lean mixtures with the least amount of hot spots. However, these concepts are not likely to be able to meet the ambitious ACARE and NASA emission reduction goals for aero engines as the pressure ratio and operating temperatures are being increased in the pursuit of increasing efficiency. Therefore alternative combustion concepts like Flameless Combustion (FC) have to be explored. A qualitative comparison of different types of combustors with FC is shown in Table 1.1, in which the advantages of FC are clear: the well-distributed reactions that characterize the FC regime often yield low temperature gradients, low NO_x emissions, high stability and low acoustic oscillations. It is worth pointing out that the level of readiness for application of FC-based combustors is lower than that of the other types, therefore the characteristics stated in Table 1.1 are based on its potential.

Table 1.1: Qualitative comparison of different combustor types and their potential.

	Combustor Type			
	Lean Premixed	Lean Direct Injection	RQL	Flameless-based
Combustion efficiency	High	High	High	High
Combustion instability	High	Low	Low	Low
Fuel flexibility	Moderate	High	High	Moderate
Integration into engine	Moderate	Moderate	Easy	Difficult
Mechanical complexity	Moderate	High	Moderate	Moderate
NO_x emission	Low	Low	Moderate	Ultra-low
Operating range	Moderate	High	High	Low
Soot emission	Low	Low	Moderate	Low
Volume requirement	Moderate	Low	Low	High

Some of the advantageous characteristics are results of the decoupling between fluid dynamics and heat release under the FC regime [25]. The most attractive feature is the potential for low NO_x emissions, which is a result of three factors that come into play under FC: i) homogenization of the reaction zones, ii) local reduction of the availability of the main reactants for NO_x formation and iii) alteration of the NO_x formation chemistry, with effects on pathways as NNH, N_2O and prompt, as well as increased NO_x reburning. The link between homogeneity and lower NO_x is well-established [26-28], as thermal NO_x formation is reduced if temperatures peaks decrease. The reduction of the reactants availability is because FC is attained with lower O_2 concentration, which in the context of GTs is often realised by flue-gas recirculation, which results in lower NO_x as well. The recirculation of combustion products is also responsible for changing the NO_x chemistry, as further discussed in Chapter 6.

A similar situation is found for land-based GTs, as the reduction goals are also challenging. Additionally, the intermittent and flexible operation required from GTs for their application along with renewable energy sources makes the future scenario even more demanding, as broad operational range is required due to the fact that engines would often have to operate at part-load. One of the alternatives to achieve stable and efficient part-load operation is through exhaust gas recirculation (EGR). From the combustion point of view, EGR may be used to achieve FC conditions [29].

Therefore, the FC regime is an opportunity for both aeronautical and land-based GTs. Although FC is already successfully applied in industrial furnaces, the conditions required to attain the FC regime are not trivial to be obtained in a GT. The requirement to preheat the reactants and to lower local O_2 concentrations present a significant challenge for the designers. Limitations in volume, which is translated into high heat density, as well as strict requirements in terms of pressure losses and operational range combined with lower overall equivalence ratios and residence times, impose challenging barriers to the design. These aspects are further discussed in Chapter 2.

1.3 THESIS STRUCTURE AND OBJECTIVES

As will become clear to the reader after the literature review shown in Chapter 2, one of the most promising engine architectures to achieve FC in GTs is the dual combustor architecture. In the same chapter, the definition of FC, as well as past the studies and conceptual designs for GT combustors aimed to employ FC are discussed in order to establish the state-of-the-art.

Subsequently, the computational models and strategies employed on all the analyses are presented and discussed (Chapter 3). The limitations, advantages, and assumptions of the models relevant for the understanding are brought up.

Chapter 4 proceeds to focus on the description of the dual combustor system in more details. Relevant results from the main combustor are displayed in order to allow the analyses shown in the subsequent chapters: the focus of Chapter 5 is the progression of pollutant emissions along the high-pressure turbine, between the two combustion chambers. The sixth and seventh chapters are the core of the thesis, as they are dedicated to analyse the flow and pollutant emissions of the ITB. Both analyses relied on the combination of CFD and Chemical Reaction Networks (CRN) to model pollutant emissions and draw conclusions.

Building up from that approach, Chapter 8 presents a computational strategy to automatically generate CRNs from a CFD solution based on user-defined criteria. The tool capabilities are showcased using a test-case designed to investigate FC.

Finally, the last chapter summarizes the conclusions attained and provides recommendations for future research. The structure was defined in order to fulfil the objectives of the current research:

i. Establish the advantages of the dual combustor configuration with respect to the attainment of the FC regime in gas turbine combustors. (Chapters 2 & 4)

ii. Determine how pollutant emissions progress in the high pressure turbine (HPT), positioned between the two combustion chambers. (Chapter 5)

iii. Model the pollutant emissions of the ITB to compare with experimental data and provide insights on the NO_x formation mechanisms. (Chapters 6 & 7)

iv. Investigate the performance of a computational tool to automatically generate chemical reaction networks based on CFD solutions. (Chapter 8)

The thesis outline is shown in the diagram of Figure 1.4.

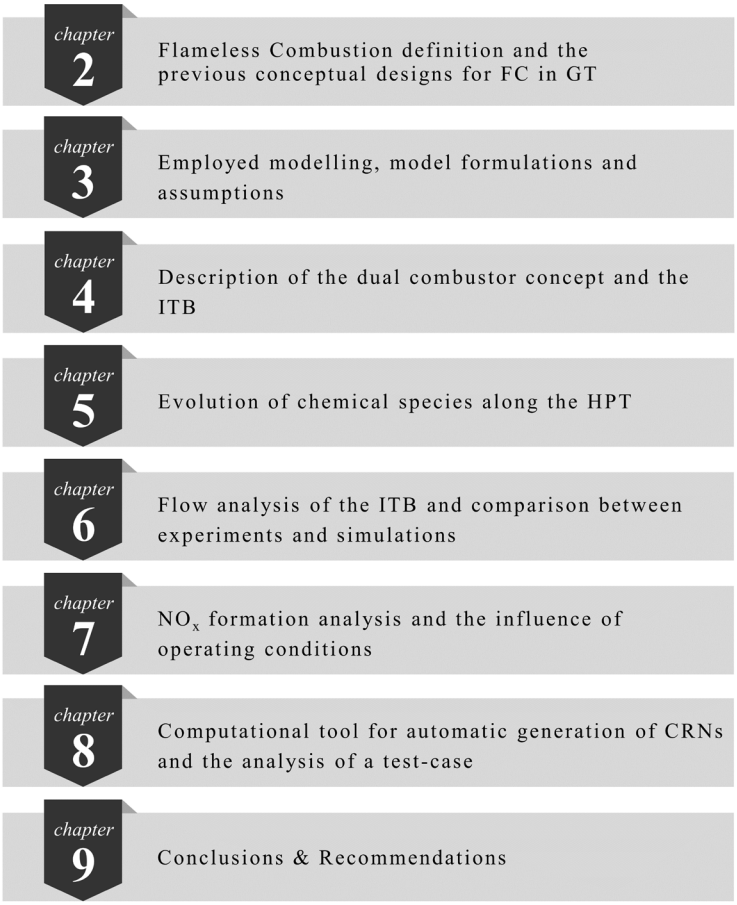

Figure 1.4: Outline of the thesis.

Chapter 2 Flameless Combustion

2.1 Definition of Flameless Combustion

Since its first description, the FC regime received different designations. This fact is in part related to the absence of a formal and consensual definition of the boundaries of the regime or of the features that characterize it. Acronyms such as MILD (Moderate or Intense Low Oxygen Dilution), HiTAC (High Temperature Air Combustion), HiCOT (High Temperature Combustion Technology), and CDC (Colourless Distributed Combustion) refer to the FC regime or slightly different but overlapping concepts.

Cavaliere and de Joannon [30] tackled the issue of the different designations in their review paper. They pointed that HiCOT is a broader concept which comprises of combustion with reactants at relatively high temperatures. HiTAC was then defined by them as a subarea of HiCOT, in which only the air was heated up to high temperatures. The authors then defined Mild Combustion (not as the MILD acronym) as a subset of HiTAC, which could be identified by two parameters: temperature of reactants and temperature rise due to the release of combustion energy.

However, Cavaliere and de Joannon [30] acknowledged the possible differences between FC, CDC and Mild Combustion as a matter of terminology that could not be fully clarified. As the FC and CDC denominations are the result of aspects related to the emission of visible radiation during the combustion process, the authors pointed that their definition of Mild Combustion could overlap but not necessarily coincide with the FC regime, considering FC to be simply a combustion regime without emission of visible radiation.

The issue is more complex if one considers that FC is often attainable using recirculation of exhaust gases, without actual air preheating (HiTAC); or that having lower luminosity is not necessarily related to distributed reactions and lower emissions [31]. As will become clear throughout the present review, the FC regime requires a precise definition to guide the research on the subject.

Historically, the regime was first described by Wünning and Wünning [32] and was referred to as Flameless Oxidation (FLOX®). The study was in the context of industrial burners and furnaces. The authors described the main features and advantages of the regime, and the definition of the boundaries was based on the furnace temperature and recirculation ratio. According to the authors, the regime could be attained if these parameters were above certain approximate values, which were obtained from their practical experience in industrial furnaces.

Contents of this chapter appeared in:

Perpignan AAV, Rao AG, Roekaerts DJEM. *A review of Flameless Combustion and its potential towards gas turbines*. Progress in Energy and Combustion Sciences 2018;69:28-62.

The recirculation of combustion products was a central parameter, defined by the recirculation ratio. The air was split into two streams, one injected along with the fuel (primary) and the other directly into the furnace (secondary). By varying the ratio between primary and secondary air, the furnace studied by Wünning and Wünning [17] changed its regime from normal to FLOX. It was observed that increasing the relative amount of secondary air allowed the reactants to mix with the combustion products prior to reacting with the fuel. In other words, the recirculation ratio increased with increasing secondary air.

Cavaliere and de Joannon [30] proposed the most used definition for the FC regime. Also referred to as a PSR-like definition [33], such definition imposes the reactant mixture to be above auto-ignition temperature at the inlet while the temperature rise due to energy release has to be lower than the same temperature. The authors defined auto-ignition temperature in the context of PSRs: the lowest reactor T_{in} in which any increment in temperature shifts the system to the higher branch of the S-shaped curve (T_{in} vs. final temperature, in this case). In systems relying on recirculation to preheat the reactants, as usually done for gas turbine combustors aimed to operate in the FC regime, such definition poses difficulties. Considering the reactants inlet temperature prior to the mixing with vitiated gases is not sufficient to describe the attainment of the regime while considering the reactants and recirculated gases to be perfectly premixed prior to any reaction is also inaccurate.

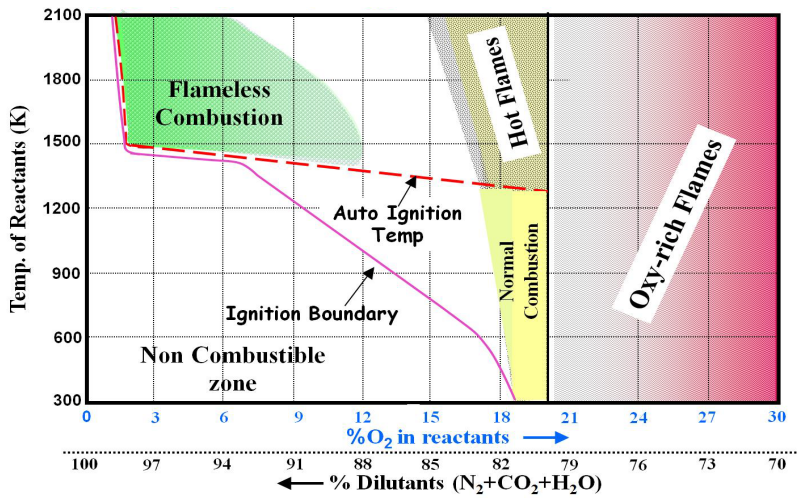

Figure 2.1: Combustion regimes diagram proposed by Rao and Levy [34].

Retaining the focus on the application to gas turbines, one of the most comprehensive definitions was that of Rao and Levy [34]. The proposed diagram, an improved version of which is shown in Fig. 2.1, highlights the roles of T_{in}, the O_2 concentration, and the recirculation ratio. However, the depicted values are only

representative and can vary significantly depending on the specific application. The diagram is useful to understand the difficulties in achieving FC in gas turbine combustors, as the values of the recirculation ratio required to achieve lower O_2 concentration are quite high.

Recently, Evans et al. [33] made a distinction between FC (or MILD) and auto-ignition non-premixed flames by extending the proposition of Oberlack et al. [35], which was developed for premixed flamelets. Their definition imposes the S-shaped curve (Da vs. T^*, the Damköhler number and the non-dimensionalized temperature, respectively) to be monotonic under the FC regime. The usual S-shaped curve is shown in Fig. 2.2, in which ignition and quenching are represented. The lower branch shows the slow increase in reaction rates before ignition (I). The state goes to the upper branch when ignition occurs since heat is released at a rate that does not allow steady transport. Following the opposite path, going from the upper branch towards lower Da, the chemical energy release occurs too slowly and the heat is not transported at a large enough rate, quenching (Q) the reactions and moving to the lower branch.

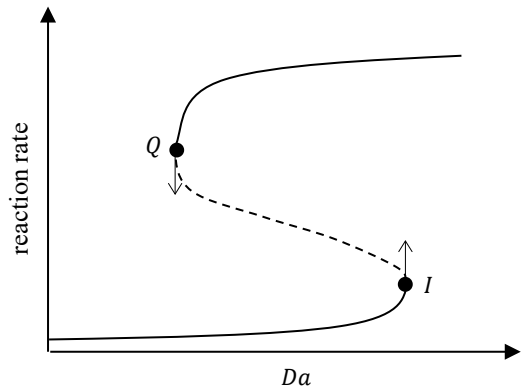

Figure 2.2: The S-shaped curve displaying ignition (I) and quenching (Q). The ordinate axis (reaction rate) can be also expressed in T^*. Da is the Damköhler number.

Therefore, a strong and arguable assumption was made by Oberlack et al. [35]: FC flames do not exhibit auto-ignition and extinction in their structures. This has serious implications to the Jet-in-Hot-Coflow (JHC) experiments since most of them would be outside the FC regime (as highlighted by Evans et al. [33]). Consequently, Evans et al. [33] considered the definition of Cavaliere and de Joannon [30] to be inaccurate, as it comprehends both auto-igniting and gradual combustion flames.

A comparison of the aforementioned definitions is shown in Fig. 2.3. The calculations are performed for methane combustion using the Cantera package [36] along with the GRI 3.0 mechanism [37], utilizing chemical equilibrium (for the PSR-like definition), premixed flamelets and non-premixed flamelets (for the S-shaped curve definitions). The considered value for the auto-ignition temperature and the one-

step reaction effective activation energy were 1000 K and 40 kcal/mol, respectively, as previously assumed [30,33].

The plots for the S-shaped curve definition for premixed flames are made with an assumption for the non-dimensional heat of combustion introduced by Cavaliere and de Joannon [30] ($Q^* \approx \Delta T/T_{in}$), while the original formulation defined $Q^* = (QY_{Fin})/(c_p M_F T_{in})$. As the criterion for a monotonic S-shaped curve is $E^* \leq 4[(1+Q^*)/Q^*]$, the approximation neglects the influence of varying fuel mass fraction and c_p for different ϕ and O_2 concentrations at the inlet. Therefore, the resulting FC region using these approximations is larger than without it. Moreover, it is worth highlighting that the formulation of Oberlack et al. [35] is valid only for lean mixtures.

The definition for non-premixed flamelets presents no difference between different ϕ as the regime is evaluated in relation to the temperature reached at stoichiometry. For low enough ϕ, the PSR definition [30] is only dependent on T_{in}, as the temperature increase is low enough for every O_2 concentration considered, as shown when ϕ = 0.4. The only requirement is then to have T_{in} above auto-ignition temperature. For ϕ close to unity, the FC region is smaller, as the temperature increase is higher, which is also the case for the definition of Oberlack et al. [35].

All three formulations are ultimately dependent on the initial temperature and temperature rise (once auto-ignition temperature and activation energy are given). Additionally, their assumptions are at first glance opposing: on one hand being above auto-ignition temperature [30], and on the other hand not exhibiting ignition or extinction [33, 35]. However, that is not the case, as the definitions share common regions. Fundamentally, the assumption of Cavaliere and de Joannon [15] is that in FC the barrier imposed by the activation energy should be surpassed by the initial temperature of reactants, while not reaching a final state of very high temperature, defined arbitrarily. On the other hand, the monotonic S-shaped curve assumption is to some extent concerned with how the energy release takes place, and not strictly with the initial and final states. The smooth heat release imposed by the monotonic S-shaped curve is especially translated into high T_{in} and low Zel'dovich numbers, as well as low fuel concentrations for premixed cases.

On a more fundamental standpoint, the Damköhler number (Da) has been constantly pointed as a good indicator for the FC regime, as it is has been shown that the interaction between turbulence and chemistry is strong under the regime. Therefore, the values of Da are likely to be close to unity under the FC regime [38-40]. The analyses performed by Cavaliere and de Joannon [30], referred to by the authors as being "more suggestive than propositive", focused largely on chemistry, while turbulence and its interaction with chemistry were left out of consideration. Many of their investigations were based on a $Da \ll 1$ assumption. While such assumption is useful to simplify the study, most authors defend that the FC regime is fundamentally linked to turbulence-chemistry interaction.

PSR-like Definition [30]:

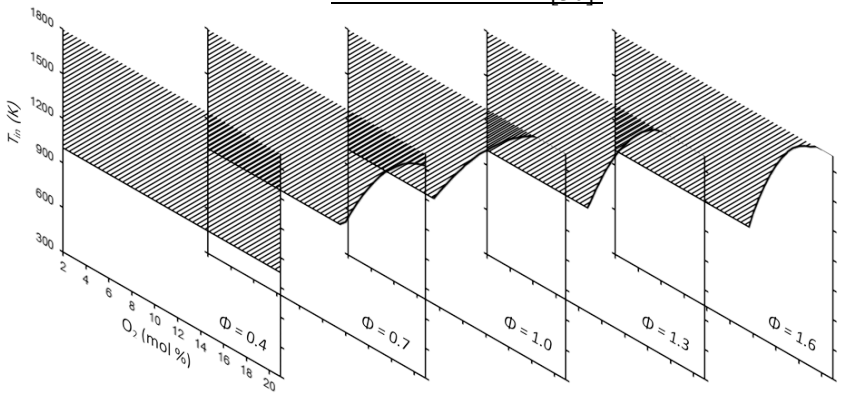

Monotonic S-shaped Curve Definition

Premixed Flamelets [35]:

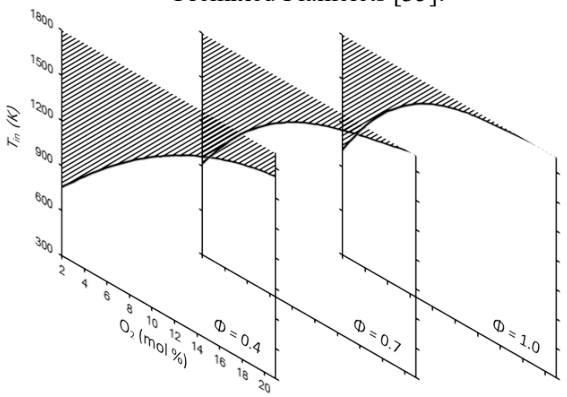

Non-Premixed Flamelets [33]:

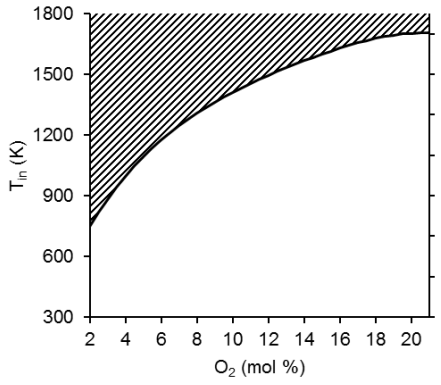

Figure 2.3: Calculated regions where the FC regime occurs in relation to reactants temperature (T_{in}), molar concentration of O_2 in the oxidiser, and equivalence ratio (Φ) according to the definitions of Caveliere and de Joannon [30], Oberlack et al. [35], and Evans et al. [33].

The generic definition of Da is the ratio between a flow (or turbulence) time-scale and a chemical time-scale. The difficulty dwells on how these time-scales are correctly defined to better represent the phenomena in FC. Examining the diagrams for conventional premixed (as proposed by Borghi [41] and Peters [42]) and non-premixed [43] flames (Figure 2.4), the distributed reactions regime corresponds to values of Da near unity and high Ka (Karlovitz number), considering the flow time-scale of Da to be the integral time-scale (Da_T). The chemical time-scale is considered to be the ratio between the laminar flame thickness (δ_L^0) and the laminar flame speed (S_L^0).

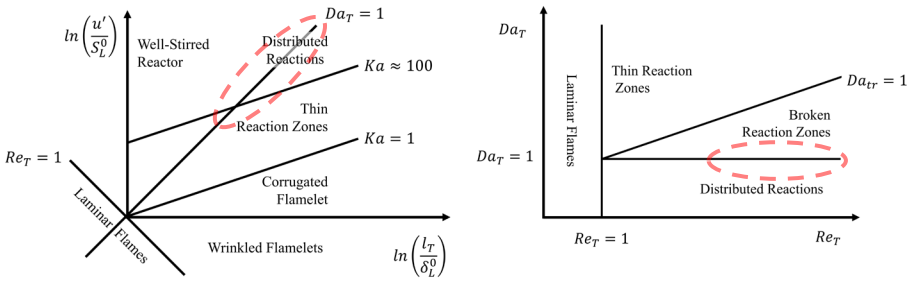

Figure 2.4: Combustion regime diagrams for premixed flames (left) and for non-premixed flames, based on the diagrams proposed by Borghi [41], Peters [42] and Law [43]. If the FC regime is considered related to distributed reaction zones, the regions highlighted by the dashed lines are relevant for the regime.

Industrial applications usually have high Reynolds numbers (Re) when compared to laboratory-scale burners. When considering Da close to unity, integral-scale Re is dependent only on the square of Ka, defined as the ratio between the chemical and the Kolmogorov time-scales. To which extent the FC regime is dependent or affected by the value of Ka is still unknown due to the difficulties involved in achieving a broad range of conditions experimentally or through DNS. However, the high turbulence intensities normally associated with high Re have been reported to aid the attainment of the FC regime [44].

From the perspective of GTs, combustion is usually placed on the premixed diagram in the thin reaction zones region, with high Re, Ka in the vicinity of 100, and Da greater than 1 [45-47]. In order to attain the region where FC is expected to occur, higher values of Ka and Re are required, while Da has to drop. One can conclude that the chemical time-scales have to be increased in relation to the flow time-scales. The high pressures required in gas turbine combustors make that particularly difficult, as reactions tend to occur faster with pressure. Therefore, investigations in high-pressure conditions are necessary. However, there is a dearth of experimental investigations in high pressure environments.

As FC is classified as partially-premixed for most applications, the classical approaches employed for defining the flow and chemical time-scales for premixed flames are not necessarily valid, while the definition for non-premixed flames is not consensual. Isaac et al. [48] proposed a method to determine the chemical time-scale using the Jacobian of the chemical source term based on Principal Variable Analysis (PVA). As there is no possible validation for the method, its analysis comprised the application to simulation results of representative cases described to be in and out of the FC regime. They employed simulation results based on the experiments of Dally et al. [49] to represent FC conditions, while Direct Numerical Simulation (DNS) data of non-premixed jet flames were used for conventional combustion. A range of Da was then calculated by considering the full range of the turbulence (or mixing) scale between the Kolmogorov and integral scales. As expected, FC showed results close to unity, while conventional combustion exhibited higher values of Da for integral mixing scales.

Similarly, Li et al. [50] compared their proposed method for calculating chemical time-scales with others present in the literature (including the aforementioned PVA of Isaac et al. [48]). The input to the evaluations was a CFD simulation of a CH_4 diffusion flame in a hot coflow, which was expected to operate under the FC regime. The authors' method presented Da values closer to unity, while the other methods had lower Da. However, Da was calculated considering the Kolmogorov scale as the flow scale, which is one of the many options to define it. Furthermore, the evaluation relied on many assumptions that eventually arrive at the starting point: i) the chosen case was assumed to be representative of FC; ii) the CFD modelling was assumed to accurately capture the flame characteristics; iii) the methods were compared based on the expected Da values for FC. Therefore, this work demonstrates well the difficulty related to defining FC solely based on Da.

The classification of combustion regimes has been disputed for decades, even when considering the aforementioned regime diagrams (Figure 2.4), whose predictive value is limited because of the assumptions involved. More importantly, even canonical laboratory flames are spread over different regions of the diagrams instead of occupying a single point, since the conditions vary locally. Given the complexity involved in FC, perhaps global parameters alone cannot define its occurrence.

If a new FC definition would be based on Da and Ka numbers, the FC regime could be perceived as a local property. One could then set a global threshold or statistically determined value to define whether the system is under the FC regime. The inconsistencies found in all the aforementioned classifications are possibly a result of the simplifications incurred in estimating local characteristics using global parameters, a common and useful practice in many fields.

The importance of having a widely accepted definition goes beyond classification. The conclusions of flame structure and modelling studies are not necessarily incremental if there is no certainty that the same regime was studied. Authors constantly disregard part of the previous works because of the inconsistencies in the classification or definition.

From a purely practical point of view, a definition including the advantages of the regime would be useful. Whether the reaction zones exhibit auto-ignition, are well-distributed, or have low visibility is of little importance if they do not yield lower emissions and acoustic oscillations. Evidently, a definition based solely on such advantages would certainly not be precise, as the conditions are not univocally achieved in combustion systems. However, this discussion is to point that while the debate on the boundaries of the FC regime is ongoing and requires more scientific support, the technological advance can take place exploiting the advantages provided by the regime.

2.2 Conceptual Designs for Gas Turbine FC Combustors

A number of concepts and designs of Flameless combustors for gas turbines have been proposed, simulated or tested. The lessons learned through these attempts are key to the possible success of future designs. This section presents the most relevant aspects and findings of the previous design attempts.

In contrast with industrial furnaces, there is no easy solution for preheating and diluting the reactants in a gas turbine combustor. The design is far more challenging because:

- Gas turbines usually operate with an overall equivalence ratio of 0.3 to 0.4 close to peak power settings, which hinders the reduction of O_2 concentration in the recirculated combustion products. Industrial furnaces, however, operate close to stoichiometry.
- The heat density (thermal energy density) of gas turbine combustors is an order of magnitude greater than that of industrial furnaces and this hinders the application of FC to gas turbines. This is especially true for aero engines as aircraft performance is sensitive to any increase in the volume and weight of the propulsion system.
- Unlike in most furnaces, the gas turbine combustor is adiabatic, which means that the recirculated combustion products are at a high temperature. This can become a problem when increasing the recirculation ratio as the temperature after mixing of incoming fresh mixture and recirculated combustion products can reach significantly higher temperature than the auto-ignition temperature, which can increase the NO_x emissions.
- Pressure losses due to the recirculation in the combustor can degrade the gas turbine efficiency.

There are important differences in the requirements between aero engines and land-based gas turbines. The latter has fewer restrictions in terms of combustor volume and weight, and no requirement for re-light capabilities. Additional restrictions could be imposed due to cycle differences (recuperation or intercooling, for example)[51]. Other differences are the possibility of having external recirculation (EGR) in land-based gas turbines, which may have a major impact on design

constraints and strategies, and their usual longer residence times [52]. Until recently, land-based gas turbines required narrower operational range. However, gas turbines shall be employed along with renewable energy sources to cope with the inherent intermittency of solar and wind energy. Therefore, the gas turbine operation will have to be more flexible. The main differences between the requirements of land-based gas turbines and aero engines are summarized in Table 2.1.

Table 2.1: Comparison of requirements and operational aspects between aero engines and land-based gas turbines.

	Aero Engines	Land-based Gas Turbines
High priority emission reduction	CO, CO_2, H_2O, NO_x, SO_x, Soot [51]	CO, CO_2, NO_x [51] SO_x, Soot (for liquid fuels)
Typical residence time (ms)	≈ 3 to 5 [52]	≈ 10 to 20 [53,54]
Weight constraints [51]	Very strict [55,56]	Flexible
Volume constraints [51,52]	Strict [55]	Flexible
External recirculation	Not possible	Possible [57]
Fuel flexibility [52]	Liquid hydrocarbons (kerosene, biofuels) [58]	Virtually any gaseous or liquid fuel. Flexibility is required.
Emission regulations [52]	Regulated only for the Landing and Take-Off (LTO) cycle [59]	Regulated for all operating conditions [60]

The FC-based combustor design attempts for gas turbines often rely on the internal recirculation of combustion products. Mixing air with combustion products is an obvious solution as it increases the temperature of the reactants and reduces O_2 concentration. The challenge is in designing a combustor that is able to promote mixing at the required rates without excessive pressure losses and within the limited available volume.

The requirements for operational range in aero engines is one of the main challenges for combustor design, and that is also the case for FC application. The attainment of low emissions while maintaining stability at part-load conditions is crucial. However, this joint requirement has not been extensively evaluated for most design concepts herein reviewed. This is partly explained by the fact FC-based combustors are still in an early stage of development. On the other hand, it will become clear that the success of design concepts would be more likely if such central issues would be addressed already from the conceptualization phase.

The adopted strategies to recirculate gases internally within the combustion chamber are: i) recirculation induced by jet momentum and ii) recirculation induced by geometry. In the first category, the FLOX® type combustors have been proposed and are primarily derived from industrial burners. These burners rely on high momentum jets to promote recirculation and the mixing between oxidiser, fuel and combustion products. Combustors with FLOX® burners oriented to gas turbine applications were tested and simulated with different approaches as reviewed below.

In the FLOX® burners, the fuel is injected through radially distributed nozzles in a pre-chamber section, where it is partially premixed with the oxidiser stream. Both fuel and oxidiser promptly enter the combustion chamber via larger nozzles, positioned in the same axes as the fuel nozzles (Figure 2.6). This concept was first developed for gaseous fuels. The axial distance between the fuel nozzles and the main nozzles (through which both air and fuel enter the combustion chamber) determines the premixedness. The radial position of the nozzles is related to mixing behaviour inside the chamber and, consequently to the chamber volume, which determines the intended energy density of the combustor. However, these design parameters were never openly discussed in the literature and their effect on performance is not precisely known.

Lückerath et al. [61] presented one of the first investigations regarding the adaptation of the FLOX® concept to gas turbines. A FLOX® burner with 12 nozzles was adapted to a combustion chamber with optical access and was operated at 20 bar (similar to the combustor shown in Figure 2.6). Using natural gas as fuel they concluded that the low emission range (for both CO and NO_x) was extended with increasing jet velocity (shown in Figure 2.5), which influenced the mixing behaviour. This fact points to issues regarding pressure losses, which increase with jet momentum.

Additionally, the operational range was relatively narrow. The reported variation in equivalence ratio is shown in Figure 2.5 as well. The behaviour of emissions with varying excess air ratio was usual: increasingly leaner mixtures yielded lower NO_x and higher CO emissions. These results are in contrast with those of Veríssimo et al. [62], discussed in Chapters 7 and 8. Although the geometries of Lückerath et al. [61] and Veríssimo et al. [62] share similarities, the latter was non-premixed, while the former had a significant level of premixedness. Essentially, Lückerath et al. [61] pointed out that the largest difficulties of the FLOX® concept for gas turbine conditions are emissions and operational range. Instabilities and flame blow-offs took place while altering the equivalence ratio and power in settings that would be required for a gas turbine operation. In most enclosed systems the rate of recirculation almost solely depends on the jet momentum which relates to the jet diameter and the heat capacity of the system. Hence, these systems end up having a limited operational range. Duwig et al. [63] also pointed to the problem of narrow operational range, while estimating the required amount of recirculated products to be approximately the same as the incoming reactants in order to sustain FC.

Lammel et al. [64] tackled the problem of having low power densities in FLOX® by increasing the diameter of the fuel nozzle to allow more fuel. However, this led to stability problems and higher emissions as the partial premixing was impaired. The burners were then redesigned to a configuration with air surrounding the fuel nozzle. The reactants further mixed in mixing tubes before entering the chamber. This design was named HiPerMix®. The authors experimentally analysed the performance of the design from 5 to 7 bar, using OH chemiluminescence, temperature and velocity measurements, as well as flue gas concentrations. The fuels tested were natural gas, natural gas-H_2 mixture, and natural gas-C_3H_8 mixture.

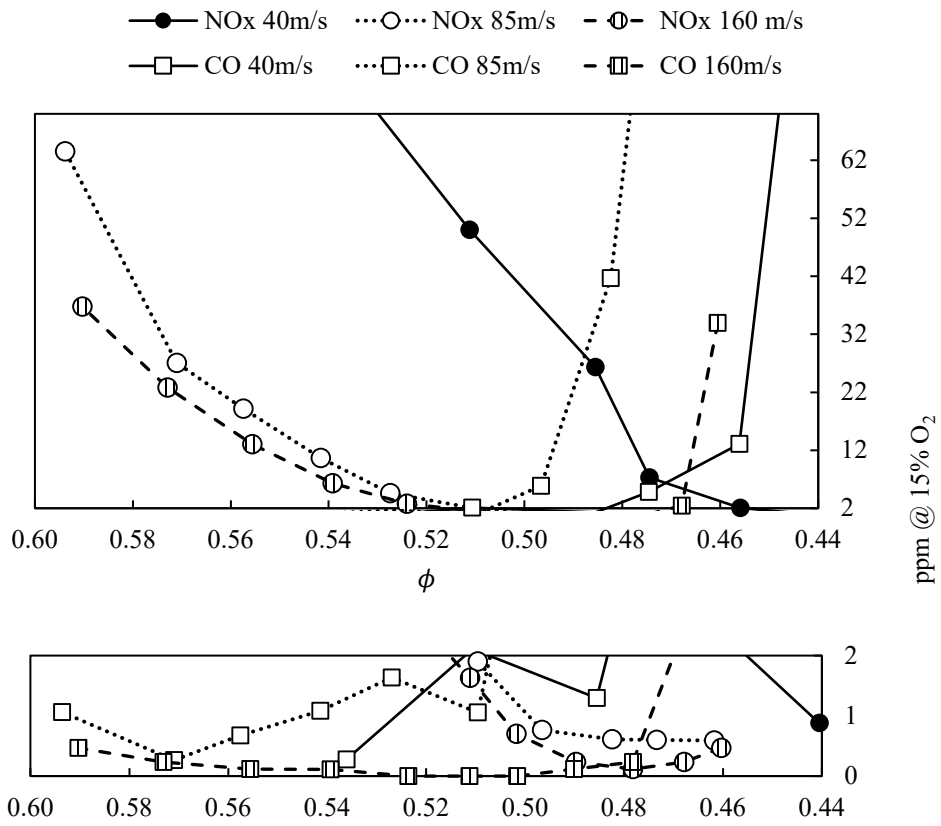

Figure 2.5: Species emission results of CO and NO_x of a FLOX® setup as functions of the equivalence ratio for three different jet velocities. Adapted from Lückerath [61]. The vertical axis was split to aid visualization and clearly show the low emissions window.

Lammel et al. [64] pointed out that the temperature fields displayed inhomogeneity due to the mixing characteristics of the HiPerMix®. Further improving the mixing would increase pressure losses to undesirable levels. Nevertheless, they showed that NO_x emissions were low (<10 ppm) for the cases in which peak local temperatures were below the global adiabatic flame temperature. In practice, these conditions were translated to equivalence ratios lower than approximately 0.6, as their analysis maintained oxidiser mass flows and varied fuel input. For low equivalence ratios local temperatures were less likely to reach temperatures close to the global adiabatic flame temperature. This was probably due to the mixing characteristics of the design. This work showcased the compromise between mixing, pressure loss and emissions using the FLOX® concept. However, more detailed studies are still required in order to develop this concept, as the results are not generalized easily.

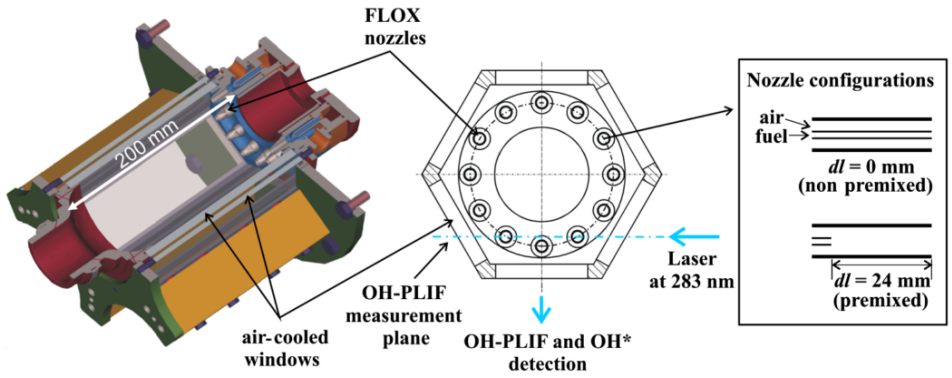

Figure 2.6: FLOX® combustor employed by Sadanandan et al. [65] and the two nozzle configurations.

In the experiments described by Lammel et al. [64] different fuels were compared based on their NO_x emission characteristics. Sadanandan et al. [65] further investigated the effect of fuel composition using a preceding FLOX® combustor operating at 20 bar to determine the effect of H_2 addition to natural gas in various proportions while maintaining the thermal power. Additionally, two types of nozzles were tested: partially premixed, with a fixed axial distance between fuel inlet and combustion chamber inlet, and non-premixed, with fuel and air entering at the same plane directly in the combustion chamber (Figure 2.6). Once again, the addition of H_2 increased the levels of NO_x emissions and moved the reactions upstream because of higher reactivity. Thus, such addition should be followed by adaptations in the jet velocities. In turn, the effect of having partial or no premixing on emissions was minor as compared to the recirculation ratio (for a given equivalence ratio). Emissions were lower for higher recirculation ratios, achieved by higher jet velocities.

As the narrow operational range is a common problem faced by FLOX® based combustors, the EZEE® configuration was developed [66] in an attempt to improve the operational range of the high energy density HiPerMix® design. The design retained the 12 inlets to the combustion chamber as in previous designs, but each of the premixing tubes was fed by two fuel nozzles placed in the same plane and radial coordinate. These fuel nozzles were tested both in centric and eccentric configurations, as shown in Figure 2.7. The idea was to extend the power modulation by regulating the fuel distribution between the nozzles. The fuel partitioning was able to enhance the operational range using natural gas and was regarded as satisfactory by the authors.

Yet another attempt using a modified FLOX® design was explored by Roediger et al. [67] and Zanger et al. [68]. The idea was to have a staged combustion with a swirler-stabilized flame in the centre of the combustor, upstream of the axial position at which the usual concentric FLOX® jets were positioned. Such architecture provides more freedom to extend the operational range and stability as the core is similar to a conventional combustor. The authors reported that a good operational range and relatively low NO_x emissions were obtained. They suggested that CO could be

reduced further by optimizing the split between the swirler burner and the FLOX®. These results were achieved in an atmospheric pressure test rig and require further testing, especially with respect to the complexity involved in fuel splitting. This concept shares similarities with the design studied by Guillou et al. [69] in which the oxidiser was injected through a swirler positioned at the centre of the burner, while the fuel jets were displaced radially and injected tangentially in order to increase the swirling motion.

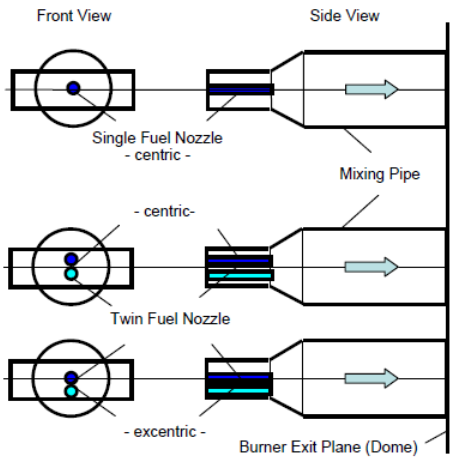

Figure 2.7: The configurations of the partially premixed nozzles studied by Schütz et al. [66] in the EZEE® concept.

These concepts [66-69] are examples of how the FLOX® approach could incorporate solutions to broaden the operational ranges similarly to pilots employed in modern lean-premixed combustors. These candidate solutions must also be evaluated with respect to emissions, as low emissions should be maintained throughout the whole LTO cycle for aero engines.

The FLOX® combustors are primarily suited for gaseous fuels. Using liquid fuels would require a different architecture as the fuel jet momentum and evaporation play an important role in the partial premixing, which is essential for this type of combustors. Attempting to overcome this limitation, Zizin et al. [70] tested possible configurations and designs that would allow the use of liquid fuels. Different atomizers and nozzles were tested for a single-nozzle and a 12-nozzle configuration with diesel, light heating oil and kerosene fuels. The authors reported no clear advantage of one configuration over the others.

Gounder et al. [71] further developed the study performed by Zizin et al. [70] and performed measurements in a 8-nozzle square-shaped combustor (shown in Figure 2.8) intended for a micro gas turbine. The authors mentioned that the spray atomizers could be easily incorporated in large FLOX® gas turbines due to the large ratio

between air nozzle diameter and atomizer diameter. However, the usual difficulties faced in previous works with gaseous fuels were still present.

Apart from the above mentioned difficulties, the applicability of gas turbine combustors based on the FLOX® concept is still uncertain. The integration of an FC combustor within a gas turbine has not been discussed in detail by researchers, especially for aero engines, which use annular type combustion chambers.

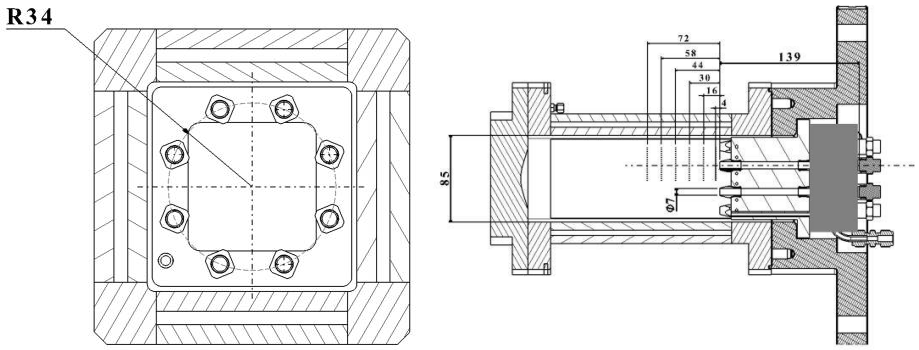

Figure 2.8: The 8-nozzle square-shaped FLOX® combustor employed by Gounder et al. [72] to study fuel spray characteristics. Top view (left) and lateral view (right).

Other experimental variations relying on jet-mixing are present in the literature. The architectures of such concepts were summarized by Arghode and Gupta [73], with variations being mostly in the relative positions of oxidiser jets, fuel jets, and exhaust. The overall difficulties and strategies to tackle them in such concepts are similar to those presented for the FLOX® configuration. Along with their summary, the authors explored the challenge of achieving high energy density inside the combustors, an important requirement of gas turbine engines.

Examining the works mentioned in this section, the gap in relation to the basic experiments, in configurations such as the JHC is evident. For example, formaldehyde (CH_2O) was not measured in realistic setups, while its role was shown to be of great importance. A better correspondence between canonical and applied experiments would also be of great value to discuss the FC regime itself and to check the validity of fundamental experimental conditions to applications.

The designs with recirculation induced by jet momentum were studied in more detail than those based in primary flow recirculation and the difficulties with operational range, combustion efficiency and engine integration are still significant obstacles. Attempting to bridge the gap between designs and basic experiments in combustors based on jet momentum, a single-nozzle premixed burner in a non-symmetrical combustion chamber was designed to represent one of the nozzles found in the FLOX® concept. An early work provided data on OH, OH* and velocity fields

[74], being useful for model validation, while a study on jet-flapping was presented using the same measurement techniques [75].

Interestingly, the setup was employed to study the combustion regimes by varying the jet velocity [76]. With increasing velocity, transitions from laminar premixed flames to turbulent premixed jets that could not be stabilized occurred. Further increase in the jet velocity caused flame stabilization possibly due to the increase in recirculation, with evidence of auto-ignition kernels. The authors suggested that the no-flame region corresponds to jet velocities higher than the flame propagation velocity and too low to cause enough recirculation. Furthermore, the authors estimated positions of the investigated conditions on the Borghi diagram (shown in Figure 2.4). They pointed out that the flames with the lowest jet velocities populated the laminar flame region. A gradual increase in velocity made the flames unstable until velocities were high enough to achieve stable combustion through recirculation, and the flames populated the corrugated flamelet and thin reaction zone regions of the diagram (see Figure 2.4). Although the methodology to calculate *Ka* and *Da* is arguable (as discussed in Section 2.1), it is certainly valuable to relate the fundamentals of the FC regime with an experiment similar to an application. Therefore, this type of experiment shall provide better understanding and modelling databases for the relevant conditions of FC applications.

As previously mentioned, another possible strategy to attain FC in gas turbines is to impose a large recirculation to the primary flow. This strategy was adopted by the FLOXCOM combustor [77-81]. The authors were able to define a preliminary geometry as well as some key design parameters like air split, recirculation ratio and the temperatures of the different streams. By means of a CRN analysis, Levy et al. [79] pointed out that increasing recirculation ratio (condition necessary to attain FC using this concept) could have a negative impact on CO emissions. This trend was later confirmed by Melo et al. [80].The central idea of the design was the generation of a large recirculation zone inside the combustor and to have the fuel injected in a region where the incoming air is already mixed with combustion products. Such design would allow the combustor to be annular and would therefore be easier to integrate into an engine. The concept was later developed into a prototype [80].

The experiments performed by Melo et al. [80] employed 60 degree sectors of the annular concept as shown in Figure 2.9. They investigated different configurations of air inlets (using slots or holes in different angles) while retaining fuel injection and key geometrical features. The cold flow recirculation ratios, as well as emissions for a range of equivalence ratios for different configurations, were compared. Recirculation ratios and emissions showed significant sensitivity to the air inlet design. However, there was no assessment in terms of pressure losses, an important parameter for the application to gas turbines.

In another work, Melo et al. [81] focused on velocity and turbulent kinetic energy distributions on different conditions in relation to power input for one of the air inlet configurations previously studied (Melo et al. [80]). Additionally, point measurements of temperature and main species were performed inside the combustor

using probes. The authors identified relatively uniform temperature profiles, suggesting attainment of the FC regime. In both works, the experiments confirmed low NO_x emissions, while the attained combustion efficiencies and CO emissions were not at acceptable levels. The authors suspected that the residence times within the combustion zone were too low and could be improved by changing dimensions or fuel injection location. Therefore, it is yet to be proven if the concept is able to attain high combustion efficiencies, broad operational range and low pressure losses. Furthermore, the FLOXCOM concept would require further tests in high pressure environment and possibly using liquid fuels.

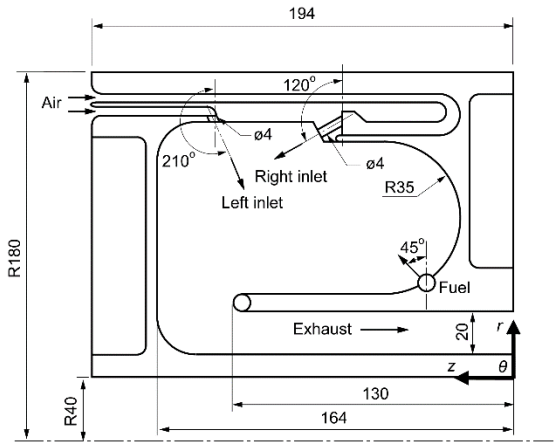

Figure 2.9: Cross-section of the 60º sector employed by Melo et al. [81].

On a more conceptual level, Levy et al. [82,83] studied the idea of having smaller recirculation zones where fuel would be injected. According to the analysis performed with the aid of CRNs, having a smaller portion of the gases being recirculated to generate local low O_2 regions could reach a compromise between achieving FC and the pressure losses caused by recirculation. The concept (Figure 2.10) also explored imposing heat transfer to the secondary air flow, which would allow combustion to take place at near-stoichiometric conditions without excessive temperature increase. In principle, such solution could improve stability and broaden the operational range, one of the largest concerns faced by the FLOX® concept. However, a proof of concept is required to back the preliminary analyses performed.

A more recent concept relying on a large recirculation zone was presented by Levy et al. [84], and was referred to as FOGT (Flameless Oxidation Gas Turbine) combustor. The authors employed the same analyses developed by Levy et al. [77], but developed a different geometry as compared to the FLOXCOM (Figure 2.11). The central idea was to have an annulus with a recirculation zone and the outlet in a direction opposite to the air inlet, thereby forcing mixing with burnt gases. The authors proposed the fuel injection to be either along with the air inlet or inside the recirculation zone.

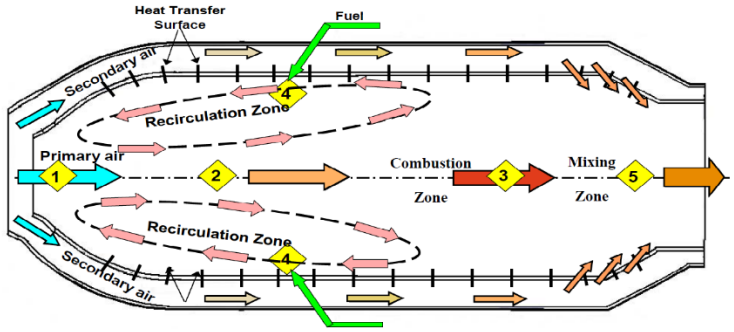

Figure 2.10: The concept proposed by Levy et al. [83]. The numbers refer to the regions simulated in their analyses.

The computational analysis performed using CFD showed promising results in terms of emissions and pressure losses. However, the concept requires a rigorous experimental analysis involving conventional fuels and assessment of the operational range. Additionally, the integration aspects within the engine should be looked into.

Most of the proposed designs did not include aspects related to the integration in the gas turbine or modifications of the engine architecture strategies that would contribute to a successful design. The concept of staged combustion with turbine stages in between was explored by Joos et al. [85], as early as 1996, but with no focus on FC. Already pointed as a solution for the reduction of NO_x emissions, the authors reported on aspects of the design development of the ABB GT24 and GT26 design family, especially related to performance and emissions. Interestingly, the concept was presented in the review of Cavaliere and de Joannon [30] as one of the options to achieve FC in gas turbines. Nevertheless, it was largely ignored in open literature for a long time.

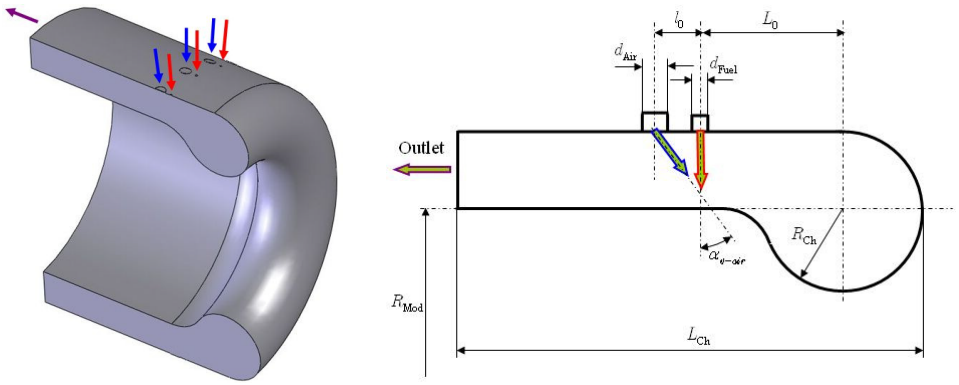

Figure 2.11: The FOGT concept [84].

Recently, the hybrid engine concept conceived and studied within the AHEAD project [86] employed a similar approach but applied to aero engines. The project explored the advantages and challenges of using cryogenic fuels in aviation, and proposed a multi-fuel blended wing body aircraft as a possible solution. The engine was conceptualized to have two sequential combustors separated by a turbine section as shown in Figure 2.12, and is further discussed in Chapter 4. The first combustor would burn cryogenic fuels (natural gas or H_2), while the second combustor, referred to as Inter-Turbine Burner (ITB), would operate with Jet-A or biofuels under the FC regime. A further study of this concept is treated in this thesis.

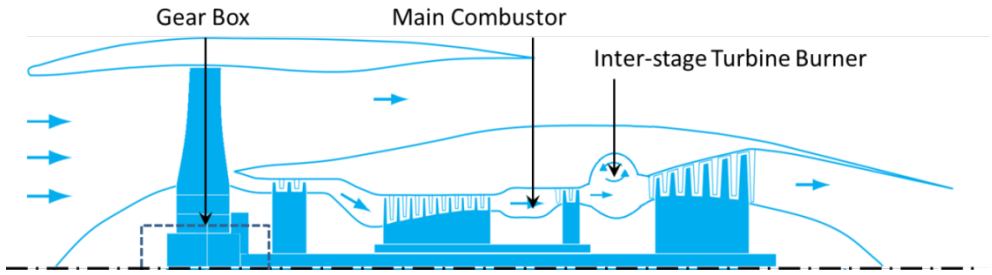

Figure 2.12: The engine concept present along with the AHEAD project [86].

The advantage of this strategy from a combustion point of view is that the gases entering the second combustor would have high temperature and reduced O_2 concentration. Such conditions would facilitate the attainment of the FC regime with lower recirculation thereby reducing the required volume and pressure losses. Additionally, the possibility of regulating the power in each combustion chamber could provide broader operational range if explored wisely [87].

The preliminary design of the ITB was presented by Levy et al. [88], and was based on chemical kinetics and CFD analysis. The authors were able to design the combustor and estimate emission values. The annular FC combustor would split the incoming vitiated oxidizer into the dilution and the combustion streams. The latter would enter a large recirculation zone where fuel is injected. The design of the ITB is evaluated by a comparison between experimental data on NO_x and CO emissions with CFD and CRN simulations as shown in Chapter 6. Opportunities to improve the design are identified and the NO_x formation pathways evaluated.

Overall, the experimental assessment of concepts based on large recirculation zones is difficult due to their predominantly annular configuration, which limits diagnostics and makes the use of prototypes challenging. Therefore, the current trend is that these concepts are being explored with available numerical tools. Designs with recirculation induced by geometry require more exploration, especially in relation to experiments. The design of experiments able to simplify the analyses while being representative of the phenomena involved should be pursued.

A summary of the most important experiments performed to assess conceptual combustor designs discussed in this chapter is shown in Table 2.2. One can notice that there is a lack of experiments performed at pressures or power densities comparable to those found in GT combustors. Nonetheless, these experiments were capable to showcase the difficulties faced when trying to apply FC to GT engines. It is clear that innovations in engine architecture are required for the successful attainment of FC, and a dual combustor configuration might be a successful candidate for future GT.

Table 2.2: Summary of experiments related to proposed FC combustors intended to operate in gas turbines displayed chronologically.

Reference	Power (kW)	Fuels	Recirculation Strategy	Pressure (bar) [a]	Power Density (MW/m^3bar) [b]	Measured Variables [c]	Measurement Techniques
Vaz et al. [89]	82 / 106	NG	Jet momentum	1	< 16	T	Thermocouples
Li et al. [90]	8.3 to 49.3	C_3H_8	Jet momentum	1	3.5 to 20.9	OH*, V	Filtering, PIV
Vaz [91]	69 to 464	NG	Jet momentum	1.00 to 4.74	up to 70	T	Thermocouples
Duwig et al. [63]	463.5	C_3H_8	Jet momentum	n/a	p n/a (vol. = $2.356 \cdot 10^{-3}$ m^3)	OH*, p, V	PIV, Filtering
Lückerath et al. [61]	100 to 475	NG, NG/H_2	Jet momentum	20	3 to 14	OH*, Y_{OH}	Filtering, PLIF
Guillou et al. [69]	n/a	C_3H_8, C_4H_{10}, C_5H_{12}, C_6H_{14}, C_6H_5-CH_3, C_9H_{20}, Jet A	Jet momentum / Swirl	1	Power n/a (vol. = $1.456 \cdot 10^{-2}$ m^3)	OH*, T	Filtering, Thermocouples
Melo et al. [80]	4 to 32	CH_4	Geometry	1	2.6 to 21.2	V	LDV
Lammel et al. [64]	600 to 1300	NG, NG/H_2	Jet momentum	5 to 7	53 to 117	OH*, p, T, V	CARS, Filtering, PIV
Melo et al. [81]	10 to 21.5	CH_4	Geometry	1	6.6 to 14.2	V, T	LDV, Thermocouples
Sadanandan et al. [65]	141 to 500	NG, NG/H_2	Jet momentum	20	4.15 to 14.69	OH*, Y_{OH}	Filtering, PLIF
Schütz et al. [66]	< 1400	NG	Jet momentum	2 to 8	60.53 to 101.90	OH*	Filtering
Roediger et al. [67]	907, 978	NG	Jet momentum / Swirler	< 10	172.38	OH*	Filtering
Zanger et al. [68]	n/a	NG	Jet momentum / Swirler	1, 4	n/a	OH*	Filtering
Zizin et al. [70]	< 40	Diesel DIN EN 590	Jet momentum	1	18.8	OH*, T_{walls}	Filtering, Mie Scattering, Temperature Sensitive Paints
Gounder et al. [71]	90 to 236	Light Heating Oil	Jet momentum	3.5	25.6 to 67.1	OH*, V (spray)	Filtering, Mie Scattering, Spray PIV, PDI
Zhou et al. [92]	161 to 381	CH_4	Jet momentum	1	11 to 26	-	-
Seliger et al. [93]	2.07 / 3.00	NG	Jet momentum	1	n/a	OH*, Y_{OH}, V	Filtering, PIV, PLIF

[a] Experiments carried at atmospheric pressure are assumed to be at 1 bar.
[b] If not reported, values are calculated based on estimated combustor volumes.
[c] All experiments had measurements of main species and pollutant emissions at the exhaust, except for [93].

2.3 SUMMARY

The generalization of results or their classification is currently impaired by the different and uncomprehensive definitions of FC. The lack of a broadly accepted definition limits the effectiveness of research, as results cannot be easily correlated.

The conclusions and recommendations of this chapter are summarized below.

- Existing definitions of FC are based on global parameters. However, because the regime is a result of local conditions, it is difficult to qualify it solely based on global parameters.
- As far as the development of applications is concerned, pollutant emissions could be incorporated in the definition of the FC regime boundaries, as it is the reason to explore the FC regime. However, a definition based on pollutant emissions would not be physically consistent.
- The current conceptual designs of FC combustors for gas turbines rely on recirculation created either by jet entrainment, a large recirculation zone, or a combination of both. Recirculation by jet entrainment might be limited in operating flexibility as the recirculation is directly proportional to the jets momenta.
- Data from experiments performed on combustors operating in the FC regime are scarce. High pressure experiments and the use of advanced diagnostic techniques should be pursued to increase our understanding.
- Most combustor designs proved to be unsatisfactory mainly because of low combustion efficiency (high CO emissions), higher pressure loss, narrow operational range, higher complexity, or unfeasible integration into the engine.
- The integration of the combustor within engines is usually neglected and should be considered in the early stages of the design in order to increase the probability of its feasibility.
- The exploration of innovative engine architectures may pave the ground to the successful attainment of FC in gas turbines, as shown by the use of an inter-turbine burner in a dual combustor configuration.

2.3 Summary

Chapter 3 Computational Modelling of Combustion and Emissions

3.1 INTRODUCTION

Due to the uncertainties regarding the underlying physics, virtually every known approach has been tried for modelling the FC regime. Bilger et al. [94] have very well summarized such approaches or paradigms, and the theoretical background is not discussed in details here. The most employed models for the simulation of FC are presented in the schematic of Figure 3.1. Different models are given a location considering two criteria: the level of detail in the description of turbulence and the level of detail in the chemistry. The size of the boxes given to a model reflects the actual practice in published works related to modelling of the FC regime. The colour shading gives an indication of the complexity of the description of the turbulence-chemistry interaction.

Solving the flow field via Direct Numerical Simulation (DNS) provides a complete description of the turbulence. The computational cost is very high and therefore most often is carried out in combination with simple chemistry. The configurations that can be handled have a simple geometry, relevant for fundamental studies and far away from practical applications. Chemical Reactor Networks (CRN) on the other hand put the computational effort in the detailed kinetics and handle flow effects via mass flow rates between reactors and the residence time in each reactor. Their parameters have to be calibrated for specific applications. The combination of turbulent flow and chemical reaction can be handled in many different ways, working either in a Reynolds Averaged Navier-Stokes (RANS) framework or using Large Eddy Simulation (LES). In both approaches, the closure of the mean or filtered chemical source term is the main issue [94]. The simplest option is to use RANS with an eddy dissipation model (EDM) considering a comparison of chemical time scale deduced from very simple chemistry and flow time scale from a turbulence model to find the effective global reaction rate.

In flamelet models and their generalisations like Flamelet Generated Manifold (FGM) [95] or Flamelet Progress Variable Approach (FPVA) [96], a laminar flame structure is considered and all important thermochemical properties and source terms are tabulated as a function of a few independent variables using detailed chemistry.

Contents of this chapter appeared in:

Perpignan AAV, Rao AG, Roekaerts DJEM. *A review of Flameless Combustion and its potential towards gas turbines*. Progress in Energy and Combustion Sciences 2018;69:28-62.

Perpignan AAV, Talboom MG, Levy Y, Rao AG. *Emission modeling of an Interturbine Burner based on Flameless Combustion*. Energy & Fuels 2018;32:822-838.

These approaches fall in the more general category of 'tabulated chemistry methods'. Detailed chemistry can be included in these flamelet calculations. The types of flamelets can cover premixed, non-premixed or partially premixed conditions. In case differential diffusion effects need to be properly represented, it is important to use detailed laminar transport properties (non-unity Lewis numbers) in the calculation of the laminar flames. The mean or resolved turbulent flame structure is computed using the state or the source terms of the laminar flames and performing ensemble averaging. The turbulence chemistry interaction is taken into account via the probability density function (PDF) of independent variables, which is most often taken as an assumed mathematical function depending on a few parameters, typically mean and variance of mixture fraction and progress variable. For low Reynolds number flames, it may be important to keep the mean laminar diffusion term including differential diffusion in the mean scalar transport equations. However, it has lower impact than including the differential diffusion in the creation of the lookup table [98]. Having a relatively low computational cost as an advantage, these approaches have been extended and tested under several conditions. A priori, it would seem that flamelet-based models for FC are not a recommended option because the high mixing intensity and dilution are supposed to lead to well-mixed conditions or at least widely distributed reaction zones. However, some DNS studies concluded that thin reaction zones are also present in FC conditions [99,100].

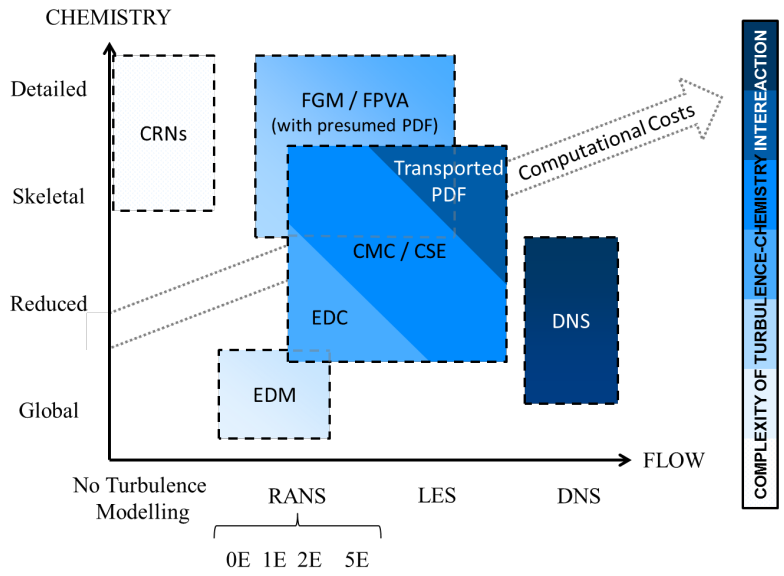

Figure 3.1: Schematic of the most used approaches for modelling FC in relation to turbulence, chemistry, turbulence-chemistry interaction, and computational costs.

In contrast, many other models are built upon a micromixing model. In principle, the importance of proper handling of the micromixing of reacting scalars is high in

FC because the chemical and flow time-scales are in the same order of magnitude. In the Eddy Dissipation Concept (EDC) model the micromixing model distinguishes between reaction zones, often modelled as perfectly stirred or plug flow reactors and their non-reacting environment. The time-scale of the large and small turbulent eddies is taken into account to find the mass exchange rate between the reaction zones and their surroundings. In the EDC framework, skeletal or even more detailed chemistry can be afforded, but the role of turbulent fluctuations on determining effective reaction rates is not well represented. Transport equations for mean mass fractions are solved and it is straightforward to include a detailed laminar diffusion term when necessary. Calibration of model constants is often needed and this aspect has received attention for FC.

More involved representations of turbulent fluctuations are used in Conditional Moment Closure (CMC) [101] and Conditional Source Estimation (CSE) [102] and in transported PDF models [103]. Especially the transported PDF models allow for a wide variety of micromixing models and their performance has received a lot of attention in the past decades. CSE has similarities with CMC in its formulation. Both CSE and CMC use conditional averages to compute the chemical source term, while the conditional fluctuations are assumed to be negligible (conditioned to mixture fraction). In the CMC, transport equations for the conditional means of species and temperature are solved, while in the CSE these conditional means are obtained by inverting the integral equation that relates the unconditional to the conditional mean in a relation involving the (presumed) PDF.

In the present work, the analyses were performed utilizing both CFD and CRN simulations. In the sections below, the models employed in the thesis are described, along with the reasoning on why they were chosen.

3.2 COMBINING CFD AND CRN

The combination of CFD and CRN is a way to deal with the difficulties in predicting pollutant emissions using solely CFD. Most CFD approaches, as discussed in the previous section, require a simplification of the chemistry. The simplification is either inherent, due to the model's assumptions, or due to computational costs. The lack of correct representation of the detailed chemistry has been pointed as the main source of inconsistency in minor species prediction [104]. Due to this fact, approaches using CRNs have gained relevance, as chemistry can be modelled in detail while keeping the computational costs relatively low.

The application of a CRN to describe the reacting flow in a combustor requires a definition of the network parameters (number and type of reactors, mass flow rates and residence times). To provide these parameters, insight into the flow field has to be used. The type of information used can be derived from overall characteristics of flow patterns such as expected presence of a recirculation zone or based on a separate CFD simulation of the flow field, either inert or with simple chemistry. Fairly good results have been achieved by designing CRNs manually. The work of Park et al. [105] utilized a similar strategy as compared the one adopted in the present work. The

resulting temperature, velocity and concentration fields from CFD calculations were used to determine the domain subdivisions within a lean-premixed gas turbine combustor. Similarly, Lebedev et al. [106] built a six-reactor CRN based on the CFD predicted mixture fraction field. Again, their focus was on modelling pollutant emissions of a gas turbine combustor. The model successfully replicated experimental results and was further used to compare the effect of different chemical reactor mechanisms [107].

The use of CRNs also enables the analysis of the species formation pathways, as shown in Chapter 6. The usual manner to account for the individual contributions relies on the deactivation of the reaction pathways. Essentially, three options have been discussed in the literature: i) sequentially add the pathways and compare the output, ii) sequentially remove the pathways [108], and iii) disable reactions of each pathway and compare to the output with all reactions enabled [109]. The latter was adopted in the present study because it requires disabling a lesser number of reactions and, therefore, potentially reduces error due to the interaction between the pathways

The applicability of CRNs to assess emissions in the FC regime is, in principle, better than in conventional combustion due to the inherent characteristics of the regime. Lower temperature and species gradients are closer approximations to the conditions of an ideal reactor. This reasoning is the core of the PSR-like definition for FC discussed in Section 2.1 Provided FC is indeed for suited to the ideal reactor representation, the number of reactors required to simulate a given volume tends to be lower in FC.

3.3 CFD Models

The CFD modelling performed in this thesis served to provide information required for the design of CRNs (Chapters 5, 6 and 7), to directly analyse pollutant formation and progression (Chapter 5), and to analyse the flow field within the ITB (Chapters 6 and 7).

All the simulations were performed with the commercial code ANSYS Fluent®. Turbulence modelling was performed in the RANS framework and the turbulence models varied depending on the specific simulation (ITB or HPT stator), as discussed in the coming chapters. No LES was performed due to the central focus on the chemistry.

When adopted, heat transfer via radiation was modelled with the Discrete Ordinates Method, along with the weighted-sum-of-grey-gases [110] to calculate the radiative properties of the gases. This radiation model provides a good compromise between performance and computational cost [111]. The model discretizes the domain in angular directions and iteratively solves the radiative transfer equation in these predefined directions.

In the following sub-sections, the turbulence-chemistry interaction models employed throughout the thesis are described. The description is provided in enough

details to allow for the understanding of the results and discussion carried out in the subsequent chapters.

3.3.1 EDDY DISSIPATION MODEL

Possibly one of the simplest turbulence-chemistry interaction models, the EDM [112] has as central assumption that combustion is controlled by large-eddy turbulent mixing. Therefore, Da is assumed to be infinitely high, which is not in accordance with what is known about FC, as discussed in Section 2.1. Moreover, the model is not able to take turbulent fluctuations into account. The predictive capabilities of the EDM are, therefore, not the reason why it was utilized. The EDM was chosen because of its low computational costs and to perform a comparison with FGM shown in Chapter 8, in which CRNs were automatically created based on the CFD solutions.

A two-step reaction mechanism was adopted to represent the combustion of CH_4, as shown by Eq. 3.1 and 3.2. The EDM determines the reaction rates based on large turbulence time scales (k/ε), as shown in Eq. 3.3.

$$CH_4 + 1.5\ O_2 \leftrightarrow CO + 2\ H_2O \qquad \text{Eq. 3.1}$$

$$CO + 0.5\ O_2 \leftrightarrow CO_2 \qquad \text{Eq. 3.2}$$

$$R_{i,r} = \left(4C_{i,r}M_i\rho\frac{\varepsilon}{k}\right)\min\left[\min_{\text{reac.}}\left(\frac{Y_{\text{reac.}}}{C_{\text{reac.},r}M_{\text{reac}}}\right), \frac{1}{2}\frac{\sum_{\text{prod.}}Y_{\text{prod.}}}{\sum_{\text{prod.}}^{N}C_{\text{prod.},r}M_{\text{prod.}}}\right] \qquad \text{Eq. 3.3}$$

3.3.2 FLAMELET GENERATED MANIFOLDS

The FGM [95] was employed as its computational cost is considerably lower than that of other models (e.g. EDC and CSE). In this approach, the mean turbulent flame structure is computed by means of the source terms of the laminar flames (or their state) and of ensemble averaging. The employed FGM approach is based on the creation of a diffusion flamelets manifold that is accessed during the CFD calculations, based on the local values of the chosen control variables. Both adiabatic and non-adiabatic formulations were employed, having mixture fraction, a progress variable (c) and enthalpy (for the non-adiabatic cases) as controlling variables. The thermal energy balance performed taking the experimental data into account (temperatures at the inlet and at the outlet, and temperatures) suggested that the heat losses were not negligible, justifying the use of the non-adiabatic approach.

The diffusion flamelets are solved in the mixture fraction space for the species (Eq. 3.4) and for temperature (Eq. 3.5). These equations are then transformed into the progress variable space. The effect of heat losses is only taken into account in burnt products, where the progress variable is equal to 1 and equilibrium is considered.

Therefore, mass fractions for progress variable lower than 1 are not influenced by enthalpy variations, while temperatures are adjusted based on mean enthalpy values.

$$\rho \frac{\partial Y_i}{\partial t} = \frac{\rho \chi}{2} \frac{\partial^2 Y_i}{\partial f^2} + S_i \qquad \text{Eq. 3.4}$$

$$\rho \frac{\partial T}{\partial t} = \frac{\rho \chi}{2} \frac{\partial^2 T}{\partial f^2} - \frac{1}{c_p} \sum_i S_i H_i + \frac{\rho \chi}{2 c_p} \left[\frac{\partial c_p}{\partial f} + \sum_i c_{p,i} \frac{\partial Y_i}{\partial f} \right] \frac{\partial T}{\partial f} \qquad \text{Eq. 3.5}$$

Most of the simulations employed a definition of progress variable dependent on CO_2 and CO mass fractions, as shown in Eq. 3.6. Investigations utilizing the H_2O and H_2 mass fractions to define the progress variable were also conducted and reported in subsequent chapters. The diffusion flamelet manifolds were generated using the GRI 3.0 chemical reaction mechanism [37]. Additionally, NO_x formation was modelled using transport equations for the mass fractions of NO, N_2O, NH_3 and HCN, with their source terms calculated via the Thermal, Prompt and N_2O intermediate pathways, with presumed β shape PDF to take temperature fluctuations into account.

$$c = \frac{(Y_{CO2} - Y_{CO2}^u) + (Y_{CO} - Y_{CO}^u)}{(Y_{CO2}^{eq} - Y_{CO2}^u) + (Y_{CO}^{eq} - Y_{CO}^u)} \qquad \text{Eq. 3.6}$$

The turbulence-chemistry interaction was taken into account with a presumed β shape probability density function (PDF), imposed to be a mathematical function depending on the mean mixture fraction and its variance (Eqs. 3.7 to 3.9).

$$p(f) = \frac{f^{\alpha-1}(1-f)^{\beta-1}}{\int f^{\alpha-1}(1-f)^{\beta-1} df} \qquad \text{Eq. 3.7}$$

$$\alpha = \bar{f} \left[\frac{\bar{f}(1-\bar{f})}{\overline{f'^2}} - 1 \right] \qquad \text{Eq. 3.8}$$

$$\beta = \left[\frac{\bar{f}(1-\bar{f})}{\overline{f'^2}} - 1 \right] - \alpha \qquad \text{Eq. 3.9}$$

3.3.3 EDDY DISSIPATION CONCEPT

The EDC model relies on the assumption that chemical reactions take place at the fine turbulent scales. The formulation employed in this thesis [113] defines the fine structure time-scale τ^* as shown in Eq. 3.10. It is equal to the Kolmogorov time-scale

multiplied by a constant, with a value of 0.4083 in the adopted formulation. This time-scale is combined with the portion of the flow occupied by the fine structures γ_λ, shown in Eq. 3.11, to define the reaction rates (Eq. 3.12).

$$\tau' = C_\tau \left(\frac{\upsilon}{\varepsilon}\right)^{1/2} \quad \text{Eq. 3.10}$$

$$\gamma_\lambda = C_\gamma \left(\frac{\upsilon\varepsilon}{k^2}\right)^{1/4} \quad \text{Eq. 3.11}$$

$$\overline{R_i} = \frac{\bar{\rho}\gamma_\lambda^2\left(\tilde{Y}_i - Y_i'\right)}{\tau'\left(1-\gamma_\lambda^3\right)} \quad \text{Eq. 3.12}$$

Reaction rates are assumed to be proportional to the mass transfer between the fine structures and their surroundings, and it is also dependent on the concentration difference of a given species between the surroundings and the fine structures ($\tilde{Y}_i - Y_i^*$). Therefore, the formulation defines the fine structure volumes, which are then treated as ideal chemical reactors.

The advantage of the model is the possibility of utilizing any chemical reaction mechanism. Additionally, the model does not assume a fixed flame structure (as in flamelet-based models), which was especially required for the analysis of the HPT described in Chapter 5.

3.4 Chemical Reactor Networks

The formulation of the physics is relatively simple in CRNs, as turbulence is not treated. The ideal chemical rectors that compose a CRN are solved by solving the mass, species and energy conservation equations. The mass balance is represented by Eq. 3.13, in which the mass fluxes entering and leaving each reactor are accounted for. In all simulations performed in this thesis, steady-state was assumed, therefore it is here shown as equal to zero.

$$\frac{dm}{dt} = \sum_{\text{ent}} \dot{m}_{\text{ent}} - \sum_{\text{out}} \dot{m}_{\text{out}} = 0 \quad \text{Eq. 3.13}$$

The species conservation in steady-state can be represented by Eq. 3.14, in which the fluxes of each species and the creation or destruction of the species is taken into account with the source term. The net increase or decrease in concentration in each reactor is determined by the reaction rates present in the chosen chemical reaction mechanism. It is worth noting that differential diffusion between species is neglected.

$$m\frac{dY_i}{dt} = \sum_{\text{ent}} \dot{m}_{\text{ent}}\left(Y_{i,\text{ent}} - Y_i\right) + VS_i \qquad \text{Eq. 3.14}$$

The adopted formulation of the energy conservation equation is written with respect to the internal energy U, as defined in terms of the species as shown in Eq. 3.15. Along with the ideal-gas assumption, the internal energy equation can be written (Eq. 3.16). Finally, the equation is rearranged to be solved for the temperature, resulting in Eq. 3.17.

$$U = m\sum_i Y_i u_i(T) \qquad \text{Eq. 3.15}$$

$$\frac{\partial U}{\partial t} = u\frac{\partial m}{\partial t} + mc_v\frac{\partial T}{\partial t} + m\sum_i u_i\frac{\partial Y_i}{\partial t} \qquad \text{Eq. 3.16}$$

$$\begin{aligned} mc_v\frac{\partial T}{\partial t} = -p\frac{\partial V}{\partial t} - \dot{Q} + \sum_{\text{ent}} \dot{m}_{\text{ent}}\left(h_{\text{ent}} - \sum_i u_i Y_{i,\text{ent}}\right) \\ - \frac{pV}{m}\sum_{\text{out}} \dot{m}_{\text{out}} - V\sum_i S_i u_i \end{aligned} \qquad \text{Eq. 3.17}$$

All CRNs were developed utilizing Cantera [36], an open-source library and solver for chemical kinetics and thermodynamics. Additionally, most of the CRNs were solved using Cantera, apart from the automatically generated CRNs discussed in Chapter 8.

The usual number of reactors employed in CRNs is considerably smaller than that of cells in CFD simulations, which facilitates the use of detailed chemical reaction mechanisms. Additionally, the relatively lower complexity of the formulation and the neglect of complex phenomena such as turbulence, radiation and tridimensional flow, usually allows the achievement of numerical convergence in the range relevant for pollutant emissions (10^{-5} to 10^{-7} in species concentrations).

Chapter 4 The Dual Combustor System

This chapter presents the engine architecture utilized for the study performed in this thesis, as well as the motivation to employ it are presented. It is important to highlight that the design of the engine is an integral part of the whole aircraft conceptualized within the AHEAD (Advanced Hybrid Engines for Aircraft Development) [18] project. The concept is centred on the use of a blended wing body with the engines sitting on the aft, as shown in Figure 4.1. This configuration allows for the accommodation of cryogenic tanks to store part of the fuel required for the missions. The storage of cryogenic tanks in a conventional commercial aircraft configuration is more challenging. Additionally, the engine positioning can be advantageous due to the efficiency gain associated with having Boundary Layer Ingestion.

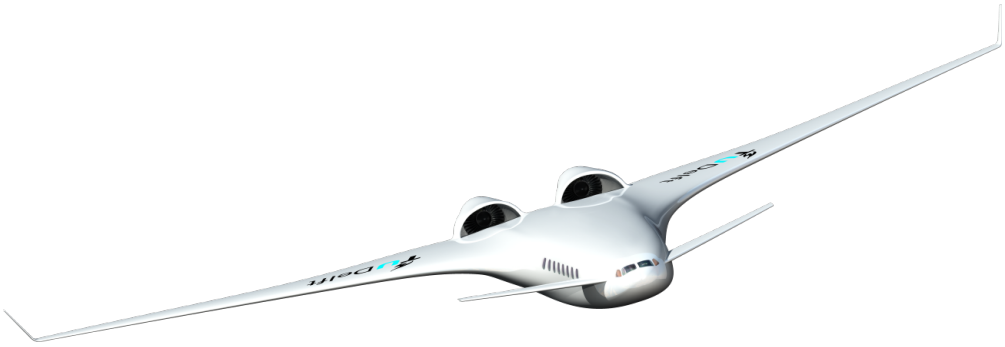

Figure 4.1: The aircraft concept developed by the AHEAD project [18].

As discussed in Section 2.2, conceptual design attempts for FC combustors relied on the recirculation of combustion products, either jet-induced or by having large recirculation zones formed due to their geometries. However, the resulting operational ranges were usually narrow. Moreover, emissions posed problems, as CO tended to increase when NO_x was at desirable levels and vice-versa. Along with the more comprehensive solution of the AHEAD project, the use of two sequential combustion chambers was proposed, having the high-pressure turbine between them (see Figure 4.2).

The hybrid engine was designed to operate using the fuels stored cryogenically in the first combustor and the conventional or bio-fuels in the ITB. Additionally, the concept takes advantage of the presence of cryogenic fuels to cool the bleed air prior

---

Contents of this chapter appeared in:

Perpignan AAV, Rao AG. *Effects of chemical reaction mechanism on NO_x formation pathways on an Inter-Turbine Burner*. The Aeronautical Journal 2019; 1-21. DOI: https://doi.org/10.1017/aer.2019.12

Perpignan AAV, Tomasello SG, Rao AG. *Evolution of minor chemical species in a gas turbine stator*. Submitted to Applied Energy.

to its utilization to cool turbine vanes and blades, reducing the required air mass flows and, therefore, reducing losses. This process is also beneficial due to the preheating of the fuels prior to their entry in the main combustor. Another feature of the engine is the use of a contra-rotating fan, as shown in Figure 4.3. As the aircraft was conceptualized as a blended wing body and the engines are positioned at the aft of the fuselage to allow for boundary layer ingestion, the contra-rotating configuration is advantageous because it enables more compact fans and higher propulsive efficiency at a given by-pass ratio [86]. From a combustion point of view, the configuration with two combustors facilitates the attainment of the FC regime in the second combustor, the ITB.

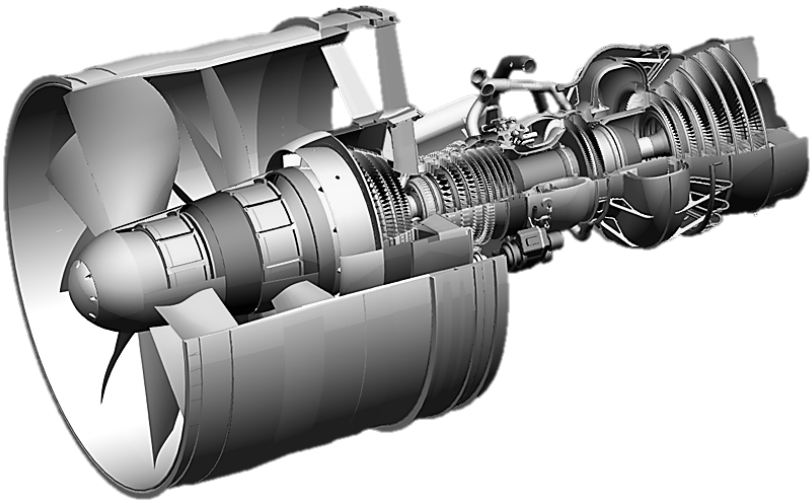

Figure 4.2: The hybrid dual combustor engine. Courtesy of Pratt and Whitney Rzeszów S.A., Copyright 2014.

Even though the concept is promising [87], it has to be further developed as there are many unknowns. The design of an ITB, or any other combustor designed to employ FC, relies on accurate prediction and representation of both fluid dynamics and chemistry. Chemical kinetics is particularly important for the prediction of pollutant e missions since low emissions are the goal of employing FC in the first place.

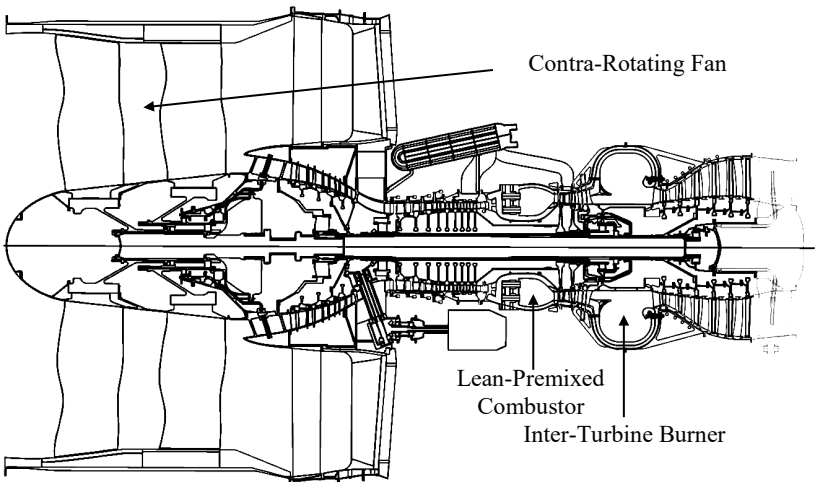

Figure 4.3: Engine concept with an inter-turbine burner. Courtesy of Pratt and Whitney Rzeszów S.A., Copyright 2014.

4.5 THE LEAN-PREMIXED COMBUSTOR

The main combustor of the dual combustor system was designed to be a lean-premixed burner. From a combustion point of view, the advantages of the combustor is the ability to avoid locally high ϕ, which in turn lowers the peak temperatures.

The concept was studied and presented in several publications by Reichel et al. [114-116], in which the stability of H_2 combustion was studied, the flashback behaviour was analysed, and NO_x emissions were measured. The combustor was designed in an annular configuration and with several injectors accompanied by premixing tubes. The combustion characteristics of the individual burners are mainly dependent on the swirl number, premixing tube length and ϕ.

From the GT combustion point of view, the challenges preventing the concept from being applied can be summarized as:

- Avoiding flashback for all operating conditions;
- Maintaining flame stability;
- Provide high premixing quality without excessive pressure losses.

The experiments presented by Reichel et al. [114-116] were performed utilizing a single burner, depicted in Figure 4.4. Part of the oxidiser entered the premixing tube axially while the remainder was added via the swirler vanes. Fuel was added through 16 axial inlet ports radially distributed around the axial oxidiser inlet. The mixture then entered the optically accessible combustion chamber were reactions took place.

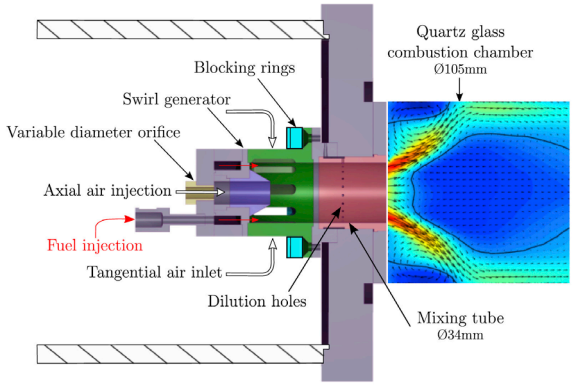

Figure 4.4: Geometry of the burner employed for the experiments carried out by Reichel et al. [115].

In Figure 4.5, one can notice that the reaction and recirculation zones shape is dependent on ϕ. Reactions become more intense as stoichiometry is approached with a reduction of the areas with negative axial velocities (depicted in blue in Figure 4.4).

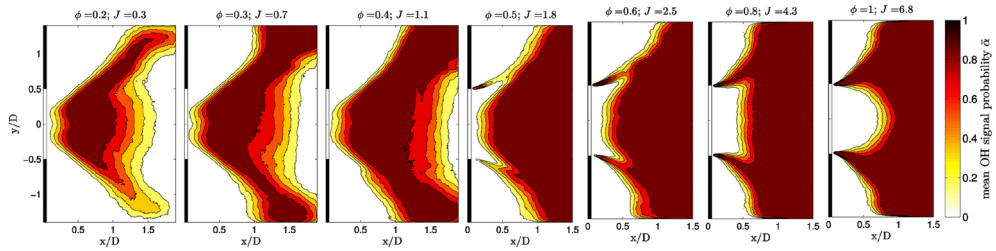

Figure 4.5: Mean OH signal for different values of ϕ and fuel momentum (J) [115].

The experimental results of emissions were employed to validate a CRN designed to represent the lean-premixed combustor. Composed of 5 reactors, the CRN was based on the velocity fields and OH-PLIF images published by Reichel et al. [115], and it is a modified version of the CRN developed by Talboom [117]. Based on the observation of these results, the relative volume of reactors representing the reaction, post-flame and recirculation zones was imposed to be dependent on ϕ. The resulting CRN, displayed in Figure 4.6, was then run for two different experimental sets which had 453 K and 623 K as T_{in}.

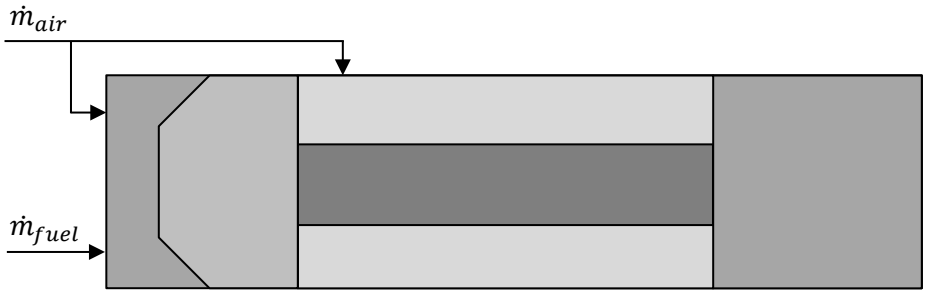

Figure 4.6: Schematic of the CRN employed to estimate the composition of the gases leaving the lean-premixed combustor.

The results of these calculations are shown in Figure 4.7: the CRN is able to reasonably reproduce the experimental results for both reactant temperatures. This same CRN was then utilized to estimate the composition of the flow entering the HPT, as shown in Chapter 5.

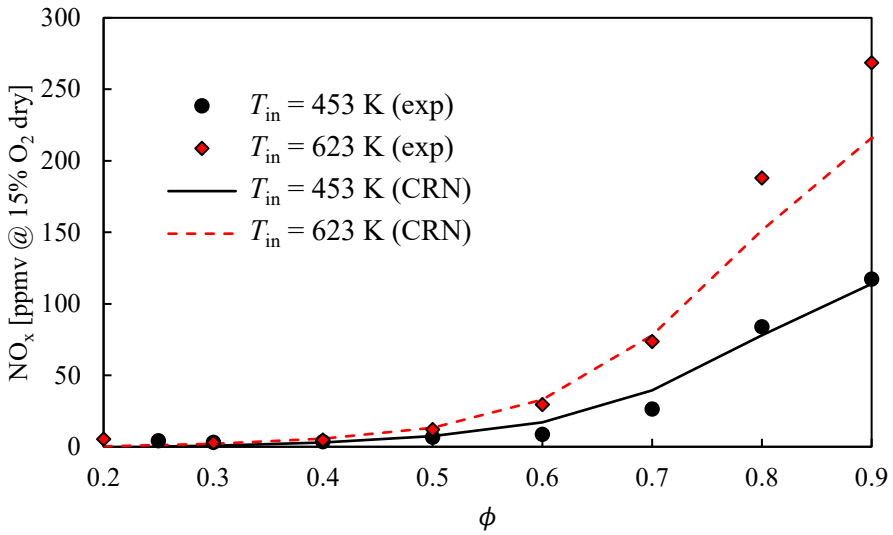

Figure 4.7: Comparison between experimental [118] and calculated values of NO_x for the lean-premixed H_2 combustor for two different reactants temperatures.

4.6 THE HIGH-PRESSURE TURBINE

Pollutant emissions evolution along turbine sections have been researched in the past, as shown in Chapter 5. Despite this fact, the vast majority of the literature neglects the changes that might occur in the other parts of the engine and considers that the species at the combustor outlet are the emissions of the engine. The configuration of the dual combustor system potentially makes the evolution of relevant species along the HPT more important for the prediction of net emissions. The analysis of the ITB showed in Chapter 6 clearly shows how complex the emission formation can be for highly vitiated environments and, therefore, variations in the inlet composition of the ITB oxidizer may cause relevant variations in the overall engine emissions.

Additionally, as emission values attained in combustors become smaller due to improved combustion technology, small variations become more important and so does the precision of computations. Variations of a few ppm can potentially cause values and trends that come out of models to be inadequate for design purposes.

Furthermore, the tendency to increase TIT and operating pressures in order to achieve higher cycle efficiencies further increases the need to include the turbine section in emission calculations.

4.7 THE INTER-TURBINE BURNER

The design of the ITB takes advantage of the lower O_2 concentrations and high temperatures at the HPT outlet to attain FC. These conditions ultimately reduce the required amount of recirculation within the combustor required and, therefore, lower pressure losses and required volume. Additionally, it has been shown that a dual combustor gas turbine engine can be more efficient due to its off-design characteristics [87].

The conceptual design for the ITB, described by Levy et al. [88], relies on a large recirculation zone, similar to the FLOXCOM [77-79] configuration. The choice for an annular combustor was made to overcome the difficulties faced by jet-induced concepts, as shown in Section 2.2. The authors computationally tested a configuration with two large recirculation zones (referred to as “double bubble”) that could potentially increase recirculation and lower emissions. However, the configuration was abandoned due to the required size and conflict with the other engine components, resulting in a single annular recirculation area to be adopted, as shown in Figure 4.3.

The concept was developed to operate with liquid fuels, either conventional aviation fuel or bio-fuels. Therefore, the design specified 60 injectors within the annulus. One of the most important features of the design is oxidizer split between combustion oxidizer and dilution oxidizer. The former enters the reaction zone (the equivalent of the primary zone of regular combustors) close to the fuel injectors, while the latter is intended to enter at another region of the recirculation zone. The combustion oxidizer path was designed to surround the liner before entering the reaction zone, thereby cooling the liner and further gaining heat.

Chapter 5 Emissions along the High Pressure Turbine

5.1 INTRODUCTION

Previously developed models to predict emissions vary in their approaches with respect to complexity, fidelity, and variables taken into account. The majority of models are based on the assumption that the pollutant emissions at the combustion chamber outlet remain constant and, therefore, can be considered the output of the gas turbine [52,105,106,120]. In such models, only the chemistry inside the combustor is considered. This has been the standard practice for emissions prediction.

However, some modelling works were dedicated to including the rest of the engine in order to study the composition of exhaust gases. The vast majority of past works was related to sulphur species and aerosol precursors. The work of Lukachko et al. [121] is an example of such studies. In a rather comprehensive study, the authors presented results for both one and two-dimensional approaches. The 1D model considered both turbines (HPT and LPT), as well as the nozzle section. The authors compared different sets of initial composition (calculated utilizing a chemical equilibrium assumption or non-equilibrium). For the considered conditions, NO and NO_2 were predicted to decrease. The investigated turbine inlet temperatures (TIT) ranged from 1459 to 1820 K at approximately 15 bar.

When utilizing the 2D model of a stator blade row, NO was shown to increase while NO_2 decreased. An important conclusion of this work is the relatively poor comparison between the 1D and 2D approaches. The study was, however, performed with a rather simple chemical reaction mechanism with respect to CO and NO_x chemistry, as the authors were mainly interested in the influence these species have on sulphur species.

Also focusing on aerosol precursors, the work of Starik et al. [122] presented a Chemical Reactor Network (CRN) model to represent the whole gas turbine engine downstream of the compressor section, including all turbine sections and the exhaust nozzle. The focus was on calculating the concentrations of ionized species along throughout the engines. The most important conclusions of the work for the present paper is that NO_x related species still had significant variations after exiting the combustion chamber. When displaying the results for NO concentration, they pointed to an increase in concentration from the combustor exit to the nozzle exhaust for a RB211 under cruise condition (TIT equal to 1540 K and turbine inlet pressure of 11 bar). However, for a JT9D-7A engine (TIT = 1200 K and pressure of 7.7 bar), the NO

Contents of this chapter appeared in:

Perpignan AAV, Tomasello SG, Rao AG. *Evolution of minor chemical species in a gas turbine stator*. Submitted to Applied Energy.

concentration decreased. The concentrations of CO were shown to decrease after the combustion chamber for both cases.

The work of Moniruzzman and Yu [123] was also focused on modelling an aircraft engine, the CFM56-2-C1, which was tested within the NASA APEX (Aircraft Particle Emissions eXperiment) program [124]. The authors simulated the engine at idle condition, as outlet values of emissions were available. Utilizing a 0D batch-reactor model, the authors utilized gas parcels to represent the unmixed nature of the flow at the combustor inlet. As a conclusion, NO_x species were predicted to change by as much as a factor of 2 when comparing the combustor and the nozzle outlets. At the investigated condition, NO was shown to decrease after the combustion chamber with an increase in NO_2. The concentration of CO decreased in the post-combustor region.

Again with a focus on aerosol precursors and particulates, Bisson et al. [125] utilized a CRN model to investigate diverse flight conditions: idle, take-off, climb and approach. Having analysed the species related to particulate formation and sulphur species in more detail, the authors broadly summarized that NO_x and CO concentrations were mostly constant or had a slight decrease downstream of the combustion chamber dilution zone, under all the visited conditions. The presented plots on the evolution of the involved species show that NO_2 increased across the HPT in all conditions, while the decrease in CO along the HPT was more pronounced for the take-off and climb conditions (TIT of approximately 1500 K).

Recently, a work exploring 3D modelling of an HPT stage has been presented [126]. The authors focused on the effect of chemical reactions on temperature, pressure and velocity. Additionally, they also reported results on the evolution of NO_x and SO_x related species. By utilizing a finite rate chemistry approach with no turbulence-chemistry interaction model, the authors concluded that temperatures drop substantially less across the turbine stage when considering chemical reactions (a difference of approximately 200 K), while pressures are maintained practically the same. Moreover, NO was shown to decrease while NO_2 increased at the chosen condition (TIT = 1341 K and turbine inlet total pressure of 31.13 bar).

From analysing previous work on the subject, it becomes clear that there is a lack of understanding regarding the evolution of CO and NO_x downstream of the combustion chamber. Additionally, it is still unclear what type of modelling is required to predict such progression and what regulates the trend of the species.

This chapter deals with the modelling of the chemistry of pollutant emissions in the HPT stator. The operating conditions were chosen based on the design of the dual combustor engine concept. The effect of different modelling approaches (CFD and CRN) are compared, as well as the use of different chemical reaction mechanisms, the inclusion of turbulence-chemistry interaction, engine operating conditions, and heat loss to the cooling of the blades. The objective of the current research is to further understand how CO and NO_x evolve along the HPT stator and what parameters affect the development of these minor species.

5.2 TEST CASE GEOMETRY

The investigation of the chemistry within the turbine stator requires the use of a representative geometry and experimental data on some aspects of the flow field to allow for the validation of the fluid models. The chosen test case is one of the turbine sections developed in the NASA's Energy Efficient Engine program with General Electric. The HPT geometry and performance data for the E3 program are available in a report [127].

The two-stage turbine was designed for a pressure ratio of 4.933 at the defined maximum climb condition. The first stage stator utilized for the present study is composed of 46 vanes. The vanes were designed to achieve Mach 0.815, 0.878 and 0.910 at the outlet for tip, mean radius and hub, respectively. The vanes had an axial width of 33.78 mm at the mean radius (345.76 mm). Table 5.1 describes the geometry.

Table 5.1: Stator vane geometry as described by Timko [127].

Dimension	Hub	Mean	Tip
Radius [mm]	325.755	345.760	365.760
Axial width [mm]	3.376	3.378	3.383
Trailing edge thickness [mm]	0.965	0.965	0.965
Uncovered turning [degrees]	9.2	8.4	8.7
Trailing edge wedge angle [degrees]	10.2	9.2	9.0

The experimental campaigns collected data on pressures and temperatures at some stations of the HPT. Moreover, this test case has been simulated in previous works [128,129]. The previous experiences allowed for an easier definition of the CFD setup required to successfully reproduce the stator flow field.

5.3 NUMERICAL MODELLING SETUP AND VALIDATION

5.3.4 COMPUTATIONAL FLUID DYNAMICS

Before looking at the chemical kinetics inside the HPT, it is important to model the flow field and make sure that it is in agreement with reality. For this reason, non-reactive flow simulations were performed and validated. Simulations solved the RANS equations along with the k-ω SST turbulence model. Total pressure and temperature were imposed at the inlet, while static pressure was imposed at the outlet. Second order discretization was employed to every transported variable. The ANSYS Fluent® solver was utilized for all CFD simulations.

The computational mesh refinement was determined based on the Grid Convergence Index (GCI) method described by Celik et al. [130] having the value of

the overall nozzle efficiency at the outlet as the observed variable (Eq. 5.1). The experimental value of the stator efficiency was used for the evaluation. The chosen fully hexahedral mesh (Figure 5.1) was composed by 2.04 million elements, while the GCI method was employed utilizing a coarser mesh (860 thousand elements) and a finer mesh (3.6 million elements). The meshes encompassed one single stator blade as a periodical boundary condition was imposed to the lateral surfaces of the domain.

$$\eta_V = \frac{1 - \left(p_{S,1}/p_{To,1}\right)^{\frac{\gamma-1}{\gamma}}}{1 - \left(p_{S,1}/p_{To,0}\right)^{\frac{\gamma-1}{\gamma}}} \qquad \text{Eq. 5.1}$$

The comparison between simulations results and experimental data on both isentropic Mach numbers (Figure 5.2) and vane efficiency show good agreement. The deviations in isentropic Mach number are lower than 1% for all points if the two outliers, one at 50% span and the other at 90% span, are excluded. Figure 5.3 shows the results of η_V on a plane located 10.16 mm away from the trailing edge of the vane. The deviation for η_V is below 3% for all data points. Given this level of agreement, the fluid flow model was considered validated and, therefore, the reactive flow simulations were carried out utilizing the same mesh, numerical settings and turbulence model.

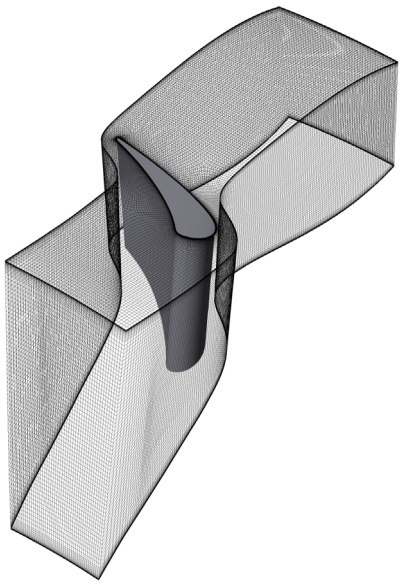

Figure 5.1: Fully hexahedral computational mesh of the a stator blade passage employed for the CFD simulations.

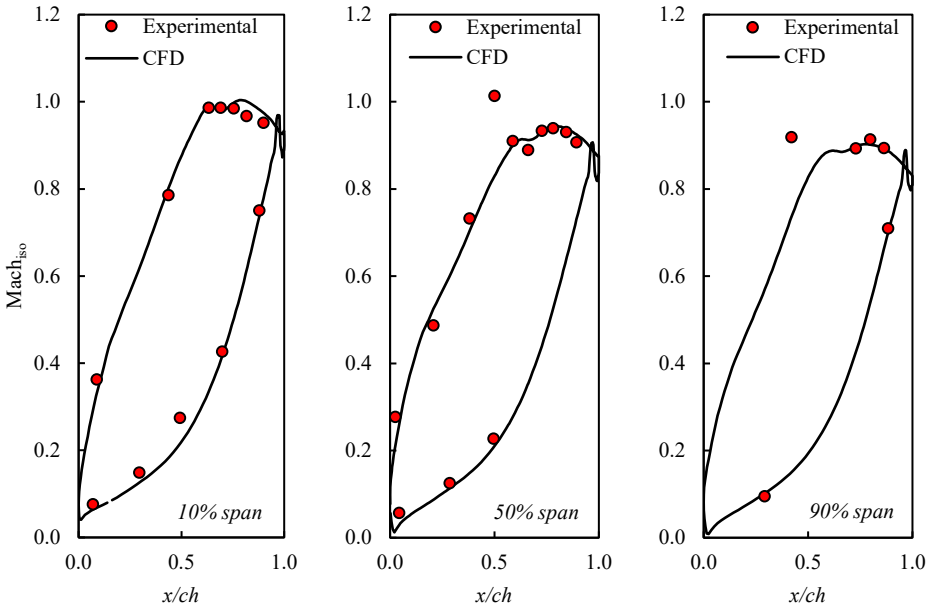

Figure 5.2: Comparison of isentropic Mach number at three different blade spans between experimental [127] and CFD values.

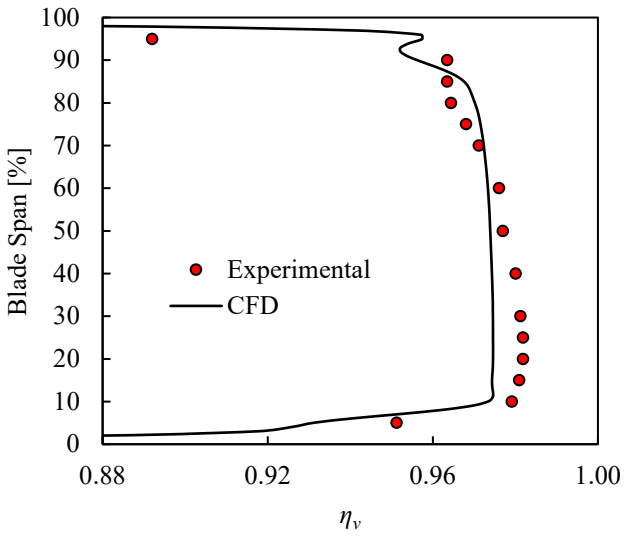

Figure 5.3: Comparison between experimental [127] and CFD values of vane efficiency at a plane located 10.16 mm downstream of the vane trailing edge.

Chemical reactions were included in the CFD simulations with two different approaches: one considering only finite-rate chemistry (FRC) without turbulence-chemistry interaction and the other using a turbulence-chemistry interaction model, namely the Eddy-Dissipation Concept (EDC), utilized as described in Section 3.3.3. This choice allows for a comparison with previous works and to assess the effect of turbulence on the reactions (although the model does not represent well the effect turbulent fluctuations, as discussed in Section 3.1).

The advantage of utilizing the EDC model is the possibility of utilizing any chemical reaction mechanism without any simplification or dimensional reduction, which has been shown to improve minor species prediction capabilities. Additionally, despite being normally used only in combustion simulations, the model is adequate for the simulation of the flow within the turbine due to its lack of assumption regarding the flame structure, unlike flamelet-based models, for example. A flamelet-based model would require capabilities as those recently presented by Efimov et al. [131], in which the FGM approach was extended to include additional time-scales. The authors identified the slowest chemical time-scale, in which the reactions related to CO and NO_x typically occur, and added a dimension to the manifold.

The default convergence parameters from the ANSYS Fluent® chemistry solver were modified to achieve higher accuracy. The values of the species of interest are relatively low (in the ppm order), therefore, usual convergence criteria do not provide consistent results.

Despite the theoretical ability of the EDC to accommodate any chemical reaction mechanism, too large mechanisms have prohibitive computational costs. Bearing that in mind, two different chemical reaction mechanisms were utilized: the NO_x subset of the San Diego mechanism [132] and the H_2/CO NO_x POLIMI mechanism [133]. The San Diego mechanism could only be utilized when H_2 was used as fuel in the first combustor, as it does not contain carbon species, and it has 20 species and 40 reactions. The POLIMI mechanism, developed for syngas combustion, has 32 species and 173 reactions, which encompass the required reactions to calculate CO emissions.

The initial compositions were adapted to these two mechanisms, maintaining the concentrations of common species, apart from N_2, which was used to ensure the mass fractions added to 1. In order to assure that the mechanism employed to calculate the initial conditions did not affect the general outcome of CFD simulations, the same case calculated using the GRI 3.0 [37] and C2 NO_x [134] mechanisms were compared. The trends of the species of interest were the same and only varied slightly in their initial values.

5.3.5 Operating Conditions and Calculation of Initial Composition

In order to estimate the conditions relevant to the dual combustor engine, the cycle calculations and performance estimates presented by Yin [135] were utilized. The work provides calculations for several energy fractions between the main combustor and the ITB. The evaluation of emissions in the HPT was performed for cases in which

90% of the energy release takes place in the main combustor. The relatively high value was chosen due to the higher resulting temperatures in the main combustor, leading to more active and relevant pollutant formation. Additionally, these conditions are relevant to conventional engines as well, and the present analysis is, therefore, valid for any modern gas turbine.

The compositions were calculated with the CRN described in Section 4.5, developed to mimic the main combustor. The developed CRN is able to replicate reasonably well the NO_x emissions measured in the experiments. The experimental campaign was performed in atmospheric conditions.

The imposed outlet static pressure values at the selected conditions were chosen with the aim of maintaining the flow field (evaluated in terms of Mach number) of the turbine as close as possible to its design point. The intention was to obtain flow fields representative of regular turbine operation. Table 5.2 displays the conditions A, B, C and D investigated in the present paper. Conditions C and D are the same except for the presence of heat transfer at the blade walls in the CFD calculations. A constant wall temperature of 1400 K was imposed as an attempt to emulate the presence of blade cooling. These conditions cause a residence time between 1.2 and 1.4 ms in the computational domain.

Table 5.2: Operating conditions investigated and their resulting turbine inlet conditions.

Condition	Main Combustor Fuel	Flight Condition	TIT [K]	Total Pressure [bar]	CO [ppm]	NO [ppm]	NO_2 [ppm]	Blade Walls
A	H_2	Cruise	1689	13.93	-	7.81	0.11	Adiabatic
B	CH_4	Cruise	1689	13.93	20.90	14.46	0.16	Adiabatic
C	CH_4	Take-off	2027	63.37	44.12	126.45	1.87	Adiabatic
D	CH_4	Take-off	2027	63.37	44.12	126.45	1.87	1400 K

5.3.6 CHEMICAL REACTOR NETWORK

After the CFD simulations were performed, a CRN was developed in an attempt to simulate the turbine stator. The CFD modelling suffers from high computational costs that make it difficult to use some chemical reaction mechanisms. The relatively low computational cost involved in the CRN calculation allows for the use of detailed chemical reaction mechanisms. On the other hand, the CRN modelling requires a priori knowledge about the flow field or assumptions related to it. Moreover, CRNs usually neglect turbulence-chemistry interaction and details of the flow field. The purpose of utilizing the CRN approach was to verify whether it is necessary to include such details in the modelling.

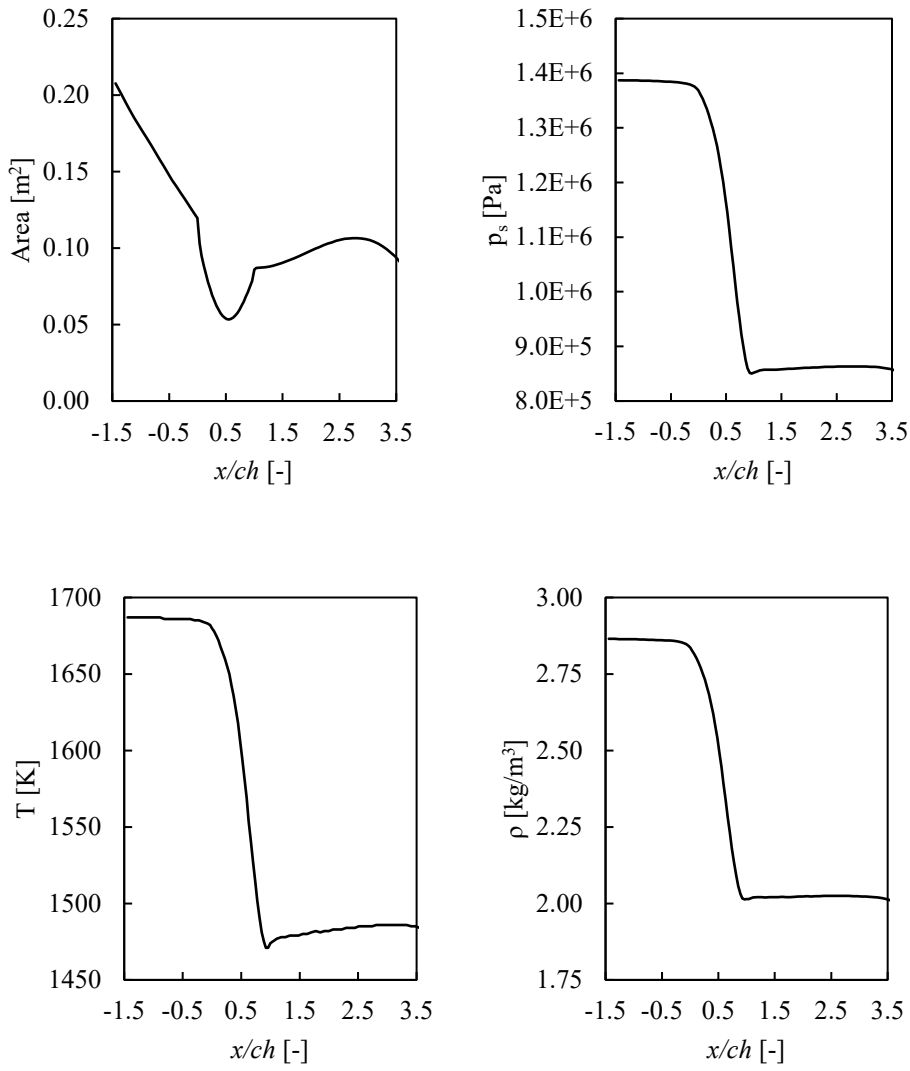

Figure 5.4: Profiles of cross-sectional area, static pressure, temperature and density imposed to the CRN for conditions A and B (cruise).

The open-source software Cantera [36] was utilized to setup and run the CRN calculations. The developed CRN was a series of PSRs. Tests were conducted increasing the number of PSRs until the results were found to be independent of the number of reactors. Thus, all results herein presented were obtained utilizing 1000 reactors. The volume of each reactor was determined by utilizing its axial location and imposing the cross-sectional area as shown in the profile of Figure 5.4. The local properties (static pressure, static temperature, velocity and density) calculated from

CFD are presented in Figure 5.4 and were imposed in a similar fashion. The velocity angle at a given axial location was utilized to correct the volume of the reactor in order to obtain similar residence times. A similar exercise was carried out for the take-off case and the properties from the CFD simulations were subsequently utilized for the CRN analysis.

The CRNs were subsequently solved utilizing detailed mechanisms, GRI 3.0 [37] and the C2 NO_x [134], as well as with the reduced mechanisms employed in the CFD analysis.

A summary of the performed simulations is shown in Table 5.3. This set of simulations are the basis of the analysis presented in the following sections.

Table 5.3: Simulations performed to each of the considered conditions.

Modelling	A	B	C	D
CFD San Diego NO_x FRC	x			
CFD San Diego NO_x EDC	x			
CFD POLIMI H_2/CO FRC	x	x		
CFD POLIMI H_2/CO EDC	x	x	x	x
CRN C2 NO_x	x	x	x	
CRN POLIMI H_2/CO	x	x	x	
CRN San Diego NO_x	x	x	x	
CRN GRI 3.0	x	x	x	

5.4 Results and Discussion

As a first analysis, the non-reactive CFD simulations were compared to those including chemical reactions. As discussed in Section 5.1, Nguyen et al. [126] found considerable differences in the thermodynamic properties when comparing reactive and non-reactive conditions. Figure 5.5 displays a comparison between the non-reactive CFD simulation and an EDC simulation for condition A (cruise, H_2) utilizing the San Diego NO_x subset. The temperature variation between the reacting and non-reacting flow simulations are all below 10 K, much lower than reported by Nguyen et al. [126] (approximately 200 K). The temperature variations seem to be related to the

slight difference in density caused by the difference in composition (which occur mostly at the wake of the blades). Similar results were obtained with the POLIMI mechanism and the FRC approach.

Comparing the cases with and without turbulence-chemistry interaction, both the FRC and EDC were applied to conditions A and B. As will become clear in the discussion carried in subsequent sections, there were substantial differences in the results with the EDC, which is in principle more reliable, as the model takes turbulence-chemistry interaction into account. Therefore, the CFD simulations for conditions C and D were only performed utilizing the EDC in order to include turbulence-chemistry interaction.

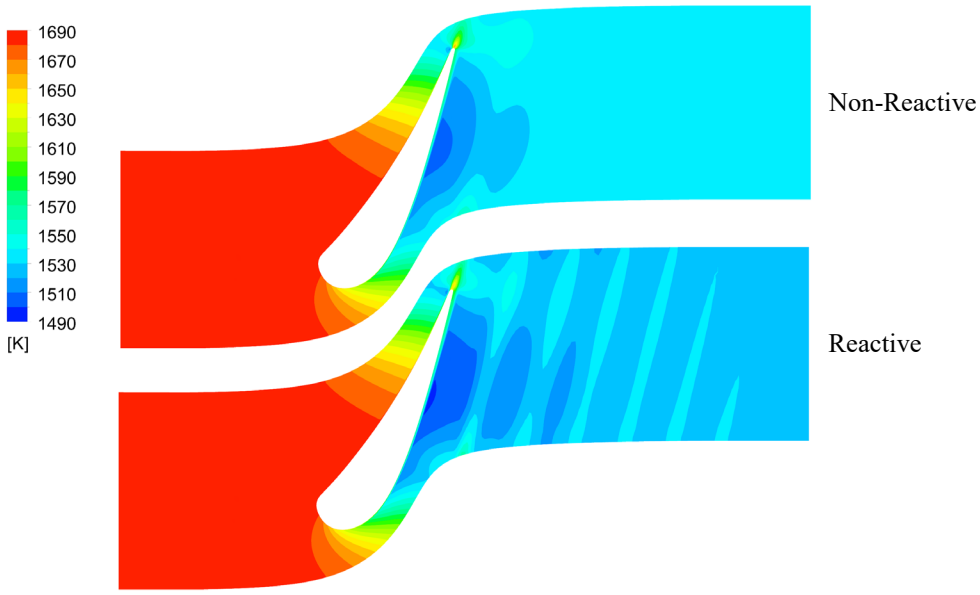

Figure 5.5: Temperature contours for a simulation without chemical reactions (above) and an EDC simulation (below) for condition A.

5.4.1 NO_x Chemistry

For the two cruise conditions (A and B), the CFD simulations predict a substantial increase in NO (Figure 5.6). The POLIMI H_2CO mechanism predicts a higher increase in NO than the San Diego mechanism. The EDC predicts a lower increase in NO than the FRC model for both mechanisms. The overall increase in NO is quite high for condition A. The lowest predicted increase (from the San Diego calculations with the EDC) is of 3.3 times the initial concentration.

This increase seems to be related to the predicted flow field to a great extent. The NO concentration rises along the passage walls and at the wake of the blades, as shown in Figure 5.7, especially along the hub and blade walls. This could be a result of the increase in residence time in these regions, and the NO_x emissions being influenced by the increased residence time. The results presented in Figure 5.7 are for the FRC approach, while the results employing the EDC displayed similar characteristics.

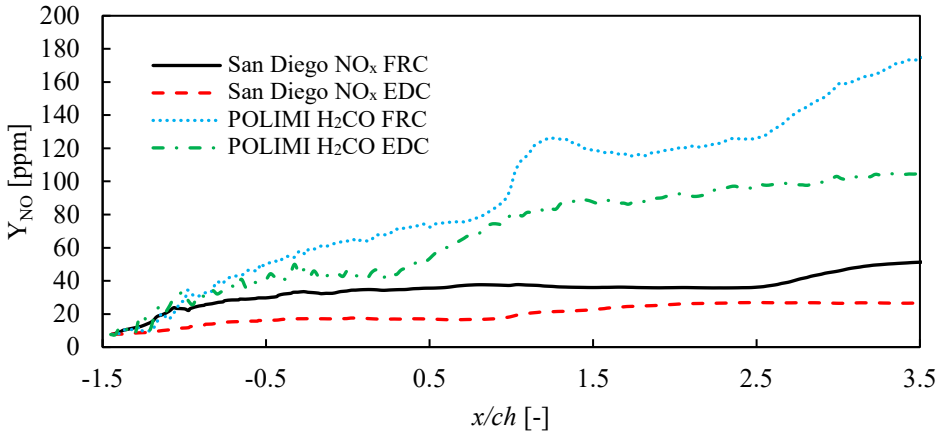

Figure 5.6: Cross-sectional average of NO mass fraction for condition A (cruise, H_2) calculated utilizing the CFD model with different chemical reaction mechanisms and chemistry modelling.

The results obtained with the 1D CRN model (Figure 5.8) are not comparable to those of CFD. The variations in NO mass fraction for the cruise conditions are quite low in the CRN calculations. The NO concentration has a slight increase from the inlet to the leading edge of the blades ($x/ch < 0$), then NO drops along the blade ($0 < x/ch < 1$), and finally there is an inflection in the concentration at the trailing edge of the blades ($x/ch > 1$). The 1D model is, of course, unable to capture the flow characteristics that seem to be driving the NO production. Part of the difference with respect to the CFD solutions might be attributed to this fact.

At conditions C and D, NO increases along the stator according to all modelling approaches as seen in Figure 5.9. The predicted variations are in the order of 15% with respect to the inlet values. The comparison between CFD and CRN results is much closer for these conditions. The largest variations are seen in the blade region ($0 < x/ch < 1$) and they can be explained by the effect of the boundary layer which is neglected in the CRN simulation.

The comparison between conditions C and D shows that the blade cooling slightly lowers the amount of NO increase. The difference in the outlet values is, however, lower than 1%.

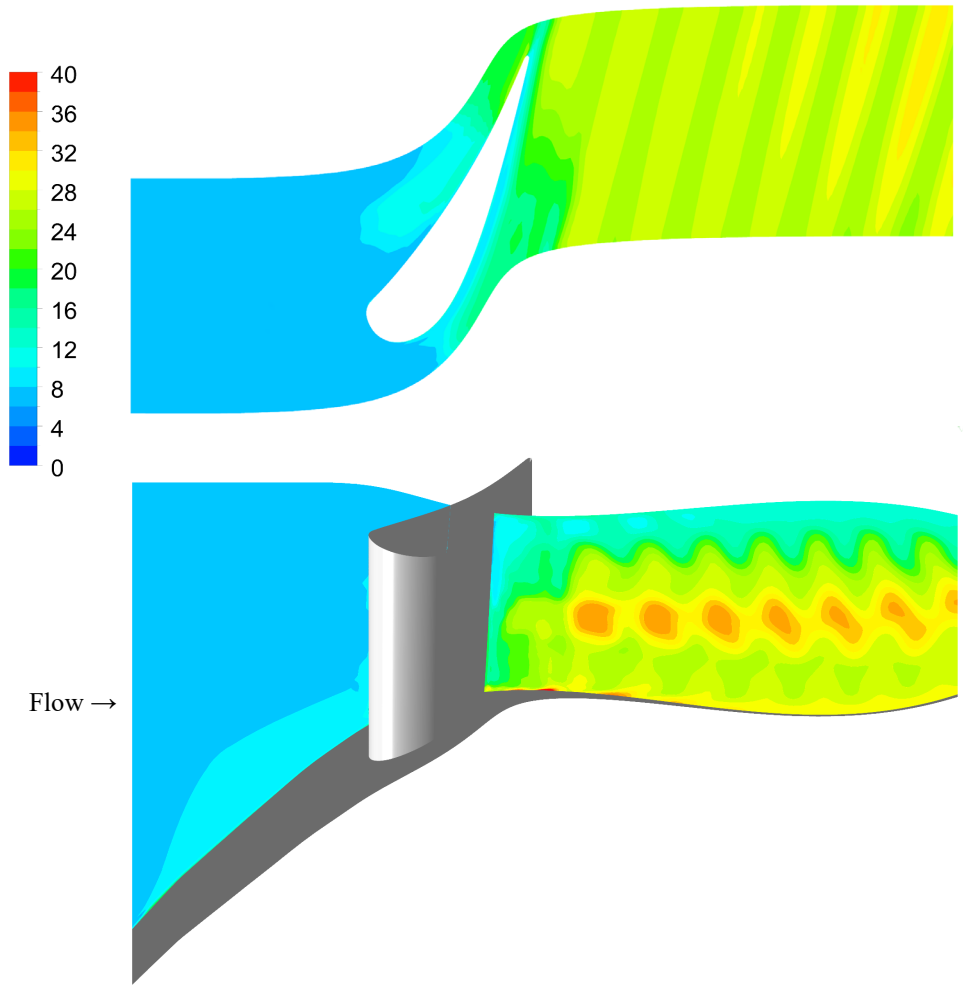

Figure 5.7: NO mass fraction contours in ppm for condition A with the FRC approach and the San Diego mechanism. A top view plane (above) and an axial plane (below).

The overall agreement between CFD and CRN in this case is related to the fact that the behaviour of NO is not as correlated to the flow field as in conditions A and B. Apart from a little influence of the hub boundary layer, the behaviour of NO (shown in Figure 5.12) is dependent on the axial position. The high influence of the blades wake seen for conditions A and B is longer present. This can be explained by the higher operating temperature in conditions C and D. With a lower temperature, NO formation is more dependent on the local temperature peaks attained at certain flow structures, while with high temperatures NO formation is mostly dependent on the residence time.

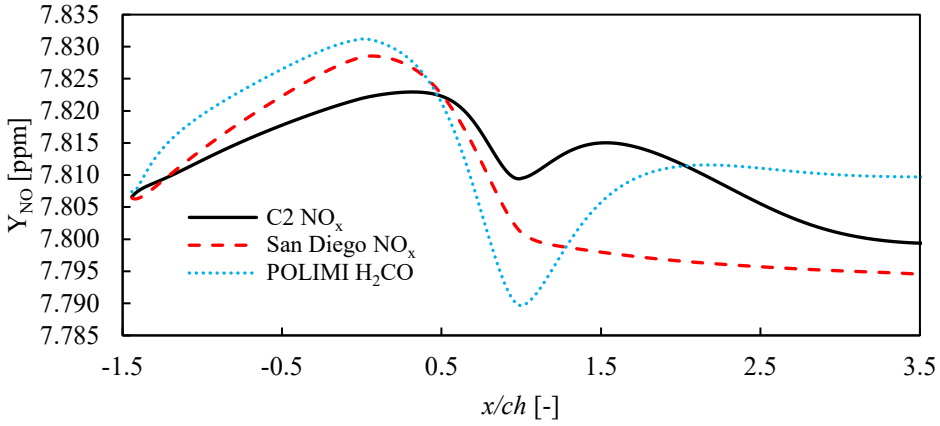

Figure 5.8: NO mass fractions for condition A (cruise, H_2) calculated utilizing the CRN model with three different chemical reaction mechanisms.

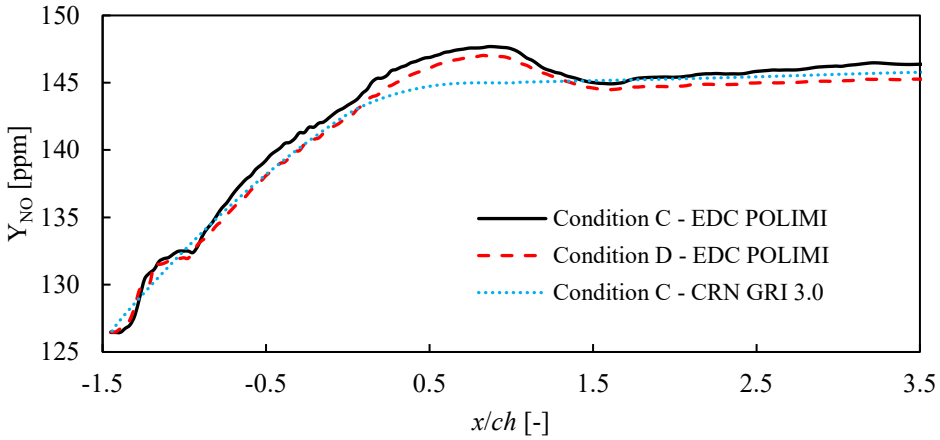

Figure 5.9: Mass-averaged NO mass fractions as functions of the axial location.

Despite having higher temperatures, the relative increase in NO for conditions C and D was lower than for conditions A and B. One of the possible reasons to explain this behaviour is the initial composition, which had a larger value of NO for conditions C and D. Therefore, reaction rates may have been limited by the initial composition.

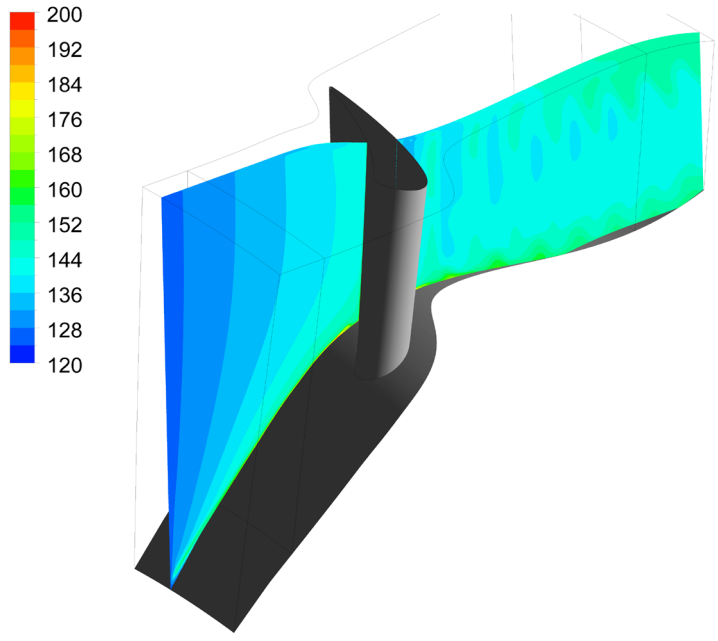

Figure 5.10: NO mass fraction contours in ppm for condition C with the EDC approach and the POLIMI H_2CO mechanism.

5.4.2 CO CHEMISTRY

The behaviour of CO emissions is dictated by the balance between its tendency to oxidize to CO_2 and the tendency of CO_2 to dissociate. It is known that dissociation occurs at higher temperatures if compared to oxidation [136].

The results concerning condition B show that CO undergoes an increase in concentration that starts at the leading edge of the blades in the CFD simulations (Figure 5.11). This behaviour is related to the increase that is predicted to occur along the blade walls, as a result of the boundary layer (Figure 5.12).

The CRN results have completely different behaviours. The concentration drops considerably from the inlet. The behaviour does not seem to be affected by the differences in temperature or pressure along the stator. The hypothesis for the different behaviour between CFD and CRN is that, locally (along the blade walls and in the wake), the CFD simulations are able to attain conditions in which CO_2 dissociation is made possible, while these local conditions are not incorporated in the CRN modelling. This hypothesis is reinforced by the analysis of the local CO concentration (Figure 5.12). Most of the increase takes place along the blade walls and its wake.

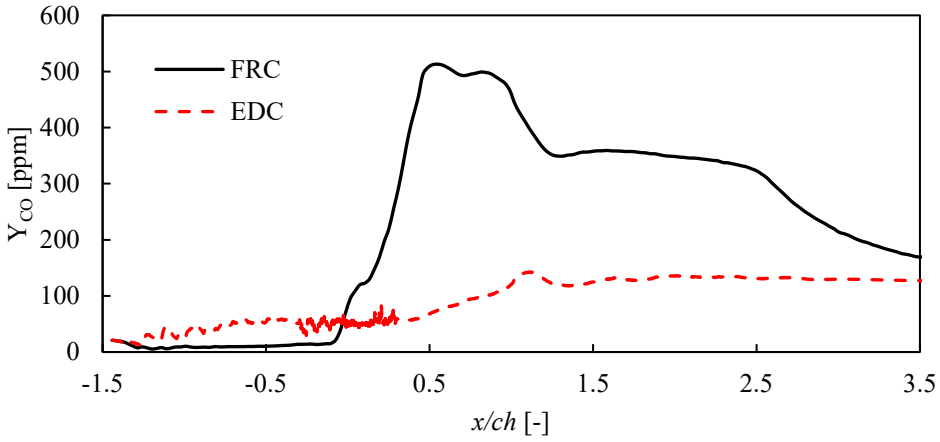

Figure 5.11: CO mass fractions for condition B calculated utilizing the CFD model with FRC and the EDC.

The simulations of conditions C and D, as in the case of NO, show that CFD and CRN results are similar (Figure 5.13). The main difference between the two approaches occurs at the blade and its wake. This is attributed to the lower rates of CO reduction in the boundary layer of the blade, which is corroborated by the lower rates in condition D. The imposition of a constant wall temperature locally cools the fluid and reduces the rate of CO oxidation. A film-cooling strategy possibly has different consequences to the behaviour, once it also changes the local compositions. The initial drop in CO near the region in which *x*/*ch* is -1.5 can be attributed to the fact that the calculation of the initial composition was performed with a different chemical reaction mechanism, as described in Section 4.5.

While in conditions A and B the CFD simulations predicted an increase in CO, the prediction points to a reduction in conditions C and D. This difference is thought to be a result of the operating pressure, since CO_2 dissociation is suppressed by higher pressures.

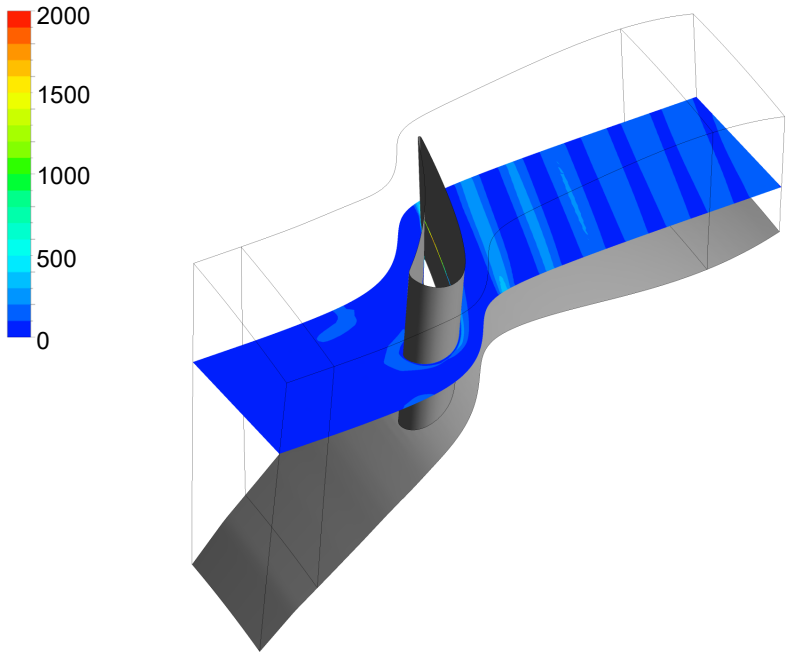

Figure 5.12: CO mass fraction contours in ppm for condition B with the EDC approach and the POLIMI H_2CO mechanism. The maximum CO mass fractions can be seen in the boundary layer of the blade.

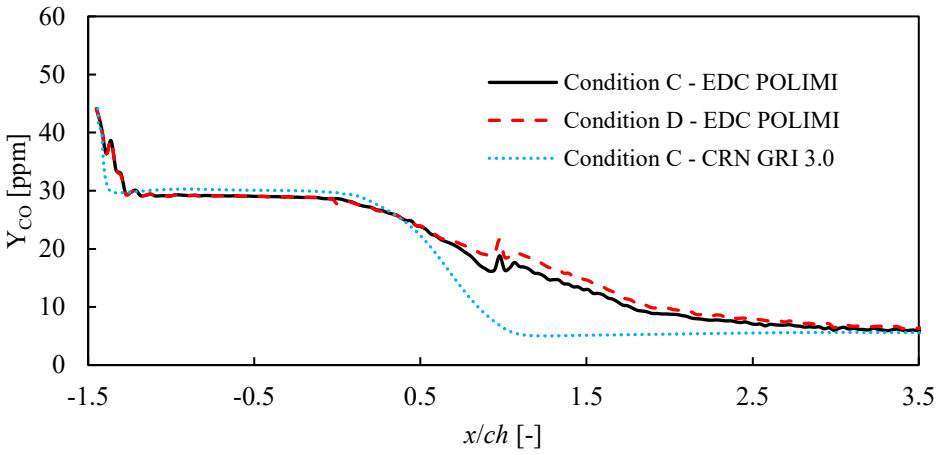

Figure 5.13: CO mass fractions for conditions C and D calculated utilizing the CFD model with the EDC, and the CRN model.

5.4.3 OVERALL OBSERVATIONS

Another meaningful result is the difference between FRC and EDC. For all investigated conditions, the EDC provided lower reaction rates, causing a lower change in species. This goes to show that neglecting turbulence-chemistry interaction may overestimate the variations in composition along the turbine. Further investigations should be conducted to assess the effect of turbulent fluctuations that are not well represented with the EDC model.

Some of the flow structures seem to directly influence emissions. The boundary layers and near-wall flows, as well as the wakes alter the reaction rates. This is due to different residence times and turbulence characteristics. The result is the periodical pattern observed in most of the plots. With respect to the reactions predicted to occur close to the walls, further studies should be conducted on the adequacy of the turbulence-chemistry interaction model. There is evidence that the EDC model requires adjustments to this type of flow [137]. Additionally, the heat transfer to the walls and the turbine blade cooling should be taken into account.

5.5 CONCLUSIONS & RECOMMENDATIONS

This chapter describes simulations performed to model the progression of the generation of pollutants through the first stage stator of a high pressure turbine. The changes in pollutant chemical species were monitored using both CFD (3D) and CRN (1D) approaches. Variations in the 3D modelling were also explored.

The conclusions of the analyses that

- the inclusion of turbulence-chemistry interaction showed to be relevant, as the EDC provided lower reaction rates than a simple FRC approach. Therefore, utilizing FRC may overestimate the amount of variation in the HPT;
- the simplification of modelling the presence of blade cooling by imposing a constant wall temperature slightly affected CO and NO formation. It is recommendable to further investigate the effect of cooling by modelling the injection of air usually performed in stator vanes;
- the discrepancy between the 1-D CRN model and the 3-D CFD model is relevant for some of the conditions. The differences seem to be increased when the species concentration is more connected to the flow structure. At higher operating pressure and temperature, the 1-D and 3-D models had good agreement, which shown that the flow structures are not as relevant for such conditions;
- the progression of CO along the turbine stator depends on the initial temperatures and composition as well as the local maxima attained. The dissociation of CO_2 may occur if temperature maxima are high enough, causing the increase in CO. The dissociation, however, seems to be

suppressed at higher operating pressure. Further investigation in the behaviour of CO for HPT relevant conditions are advised;

- the precision of the chemistry solver coupled with the CFD solver is a concern for this type of simulations. Small convergence tolerances must be imposed in order to achieve consistent solutions, which causes long computational time;
- including non-uniform inlet compositions and properties may cause different results and should be investigated.

Chapter 6 Analysis of the Inter-Turbine Burner

In this chapter, the analyses performed to assess the ITB are presented and discussed. As the previous chapters made clear, the ITB is key to achieve low emissions by utilizing the FC regime in the dual combustor configuration.

6.1 INTRODUCTION

The adopted strategies to recirculate vitiated combustion gases internally within a combustor can be divided into two categories: i) jet-induced and ii) geometry-induced recirculation. Studies on both configurations have highlighted challenges regarding operational range, narrow low emissions window, combustion efficiency, or integration within the engine.

In the first category, the FLOX® type combustors are the most explored configuration. The concept of these burners relies on high momentum partially-premixed jets to promote the mixing of the incoming reactants and recirculated combustion products. The fuel is injected through radially distributed nozzles in a pre-chamber section, where it is partially premixed with the oxidiser. Both fuel and oxidiser promptly enter the combustion chamber through larger nozzles, positioned on the same axes as the fuel nozzles.

The first investigations under high pressure conditions pointed to issues regarding pressure losses as the low emissions window could only be extended by increasing the jets momenta [61]. Furthermore, the energy density was lower than that of a conventional gas turbine combustor. In order to tackle the problems of low energy density and narrow operational range, the conventional FLOX® was redesigned using a non-premixed configuration with the oxidiser being injected as coflow to each fuel jet [64], allowing larger fuel mass flow rates. Another attempt involved having each of the premixing tubes fed by two fuel nozzles placed in the same plane and radial coordinate [66]. The concept aimed at extending the power modulation by regulating the fuel distribution between the nozzles.

Although these configurations were reported to provide better results compared to the baseline design, further investigations were not performed (or published). Instead, the same group studied a swirler-stabilized flame in the centre of the FLOX® combustor [67,68]. The architecture would operate similarly to a conventional combustor in its centre, providing more freedom by splitting the air between the FLOX® and the swirler burner. The results of the investigations were promising, in spite of the relatively high level of CO emission. As the combustor was tested at

Contents of this chapter appeared in:

Perpignan AAV, Talboom MG, Levy Y, Rao AG. *Emission modeling of an Interturbine Burner based on Flameless Combustion*. Energy & Fuels 2018;32:822-838.

atmospheric pressure, more detailed investigations would be required to further prove the validity of the design, especially in terms of pressure losses.

The FLOX® concept was initially conceived as a combustor for gaseous fuels. However, since liquid fuels are important to gas turbine applications, the use of liquid fuels in FLOX® has been recently investigated. Zizin et al. [70] tested possible configurations and designs that would allow the use of liquid fuels. Different atomizers and nozzles were tested for both single-nozzle and 12-nozzle configuration. The authors reported no clear advantage of one type of atomizer or nozzle over the others. The study was extended to an 8-nozzle configuration intended to operate in micro gas turbines [71], the conclusion was that the atomizers could easily be incorporated in the FLOX® concept because of the large ratio between the air nozzle and atomizer diameter. However, the typical problems affecting FLOX® combustors operated with gaseous fuels were anyway experienced: too limited operational range and narrow low-emissions window.

In the studies mentioned above, the integration of the combustor within the gas turbine has not been discussed in detail and the adopted mixing principle is more suited for can-type combustors, which is not suited for modern aero engines. Therefore, the future and applicability of the FLOX®-based gas turbine combustor is still uncertain. Furthermore, a range of other configuration variants relying on jet-mixing is documented in the literature and has been summarized by Arghode and Gupta [73]. The difficulties faced in the design of such configurations are similar to those faced by when designing for the FLOX® configuration.

The other approach which has been investigated in order to solve the problems connected with FC in GT is based on the design of a combustion chamber geometry that causes large recirculation zones [77-81]. This strategy was adopted for the combustor developed with the FLOXCOM [77-79] project, which was conceptually designed with the aid of Chemical Reactor Networks (CRNs). The FLOXCOM was characterized by an annular shape, as most of the modern gas turbine combustors, and this provided an advantage over the FLOX® concept.

Experiments were performed utilizing an adapted prototype having a 60° sector of the full annular combustor [80]. Diverse configurations of air inlets were experimented with, as the position and direction of the injection showed to have significant influence on the performance. Recirculation ratio and pollutant emissions are sensitive to the air inlet design. Although the experiments did not assess the pressure losses, they are probably also dependent on such design choices.

In another work, the velocity and turbulent kinetic energy fields within the FLOXCOM were investigated [81]. Additionally, point measurements of temperature and main species were performed. Relatively uniform temperature profiles were identified, pointing to a successful attainment of the FC regime. The experiments showed low NO_x emissions, while CO emissions and combustion efficiencies were not at satisfactory levels. The authors suspected that the residence times within the combustion zone were too low and that this could be overcome by changing dimensions or fuel injection location. However, gas turbine engines have severe

constraints regarding the combustor volume, which could make it difficult to attain high enough residence times.

In view of the difficulties faced when utilizing both strategies, the study of an alternative was proposed within the scope of the AHEAD project [86,119]. Among other features, the project explored the advantages and challenges involved in having two sequential combustion chambers. The first and main combustion chamber would operate with fuels stored cryogenically, while the second would be an inter-turbine burner (ITB) intended to operate under the FC regime and the analysis of the experimental and simulated performance of the ITB configuration is the topic od the following sections.

6.2 COMBUSTOR EXPERIMENTS

Instead of the full annular combustor, as described in Section 4.7, the experimental campaign was focused on an 18° re-scaled section to be tested at atmospheric conditions [138]. This experimental combustor sector contained three fuel ports (as the full annulus was designed to have 60 injectors). Part of the oxidiser entered the combustor along with the fuel (combustion oxidiser), in coflow. The diameter of the fuel injectors was 1 mm long, while that of the cylinders of oxidiser coflows was 8.3 mm long. The dilution oxidiser stream entered near the other end of the recirculation zone (see Figure 6.1).

Experiments were conducted at atmospheric pressure using CH_4 as fuel. The incoming air could be preheated, diluted with N_2, or diluted with H_2O (in order to emulate the products of combustion from the first combustion chamber using H_2). The laterals of the combustor had quartz windows, which were employed for visual inspection. The experiments aimed to understand the behaviour of the combustor operating parameters in relation to the emissions measured at the outlet of the combustor. The details of the experimental campaign will be described in an upcoming publication by the team in Technion. There is no information available on the uncertainty of the experimental data.

The combustor was tested for various equivalence ratio, N_2 and H_2O dilution levels. Conditions with oxidiser dilution were obtained by maintaining air and fuel mass flows while adding different amounts of N_2 or H_2O to the oxidiser stream. The addition of H_2O was realized in order to emulate the vitiation of the gases as it would happen in the dual combustion system. Equivalence ratio was altered by maintaining the fuel mass flow ($5.91 \cdot 10^{-5}$ kg/s) and changing the amount of air.

Photographs of the combustor with varying degree of N_2 dilution can be seen in Figure 6.2. Apart from moving the reaction zone downstream due to the larger mass flow rates, N_2 addition increased the volume occupied by the reaction zone and increased the radiation from the combustor walls (relative to the flame region radiative emission), a common feature of the FC regime as shown by Tu et al. [139], for example.

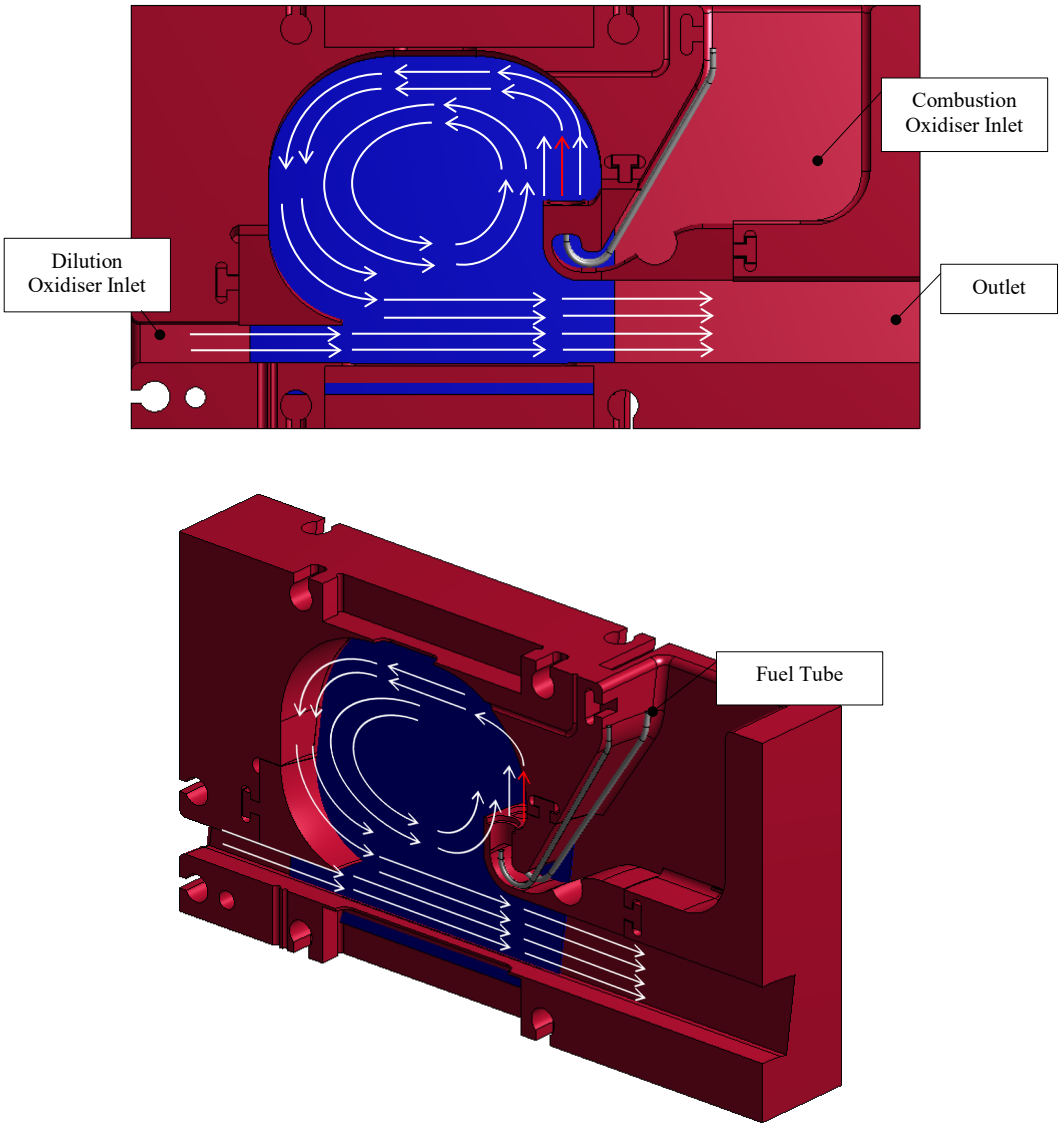

Figure 6.1: Geometry of the 18-degree combustor sector employed in the experiments. Geometry is cut in half along the longitudinal axis, with the quartz window depicted in blue [138].

a.

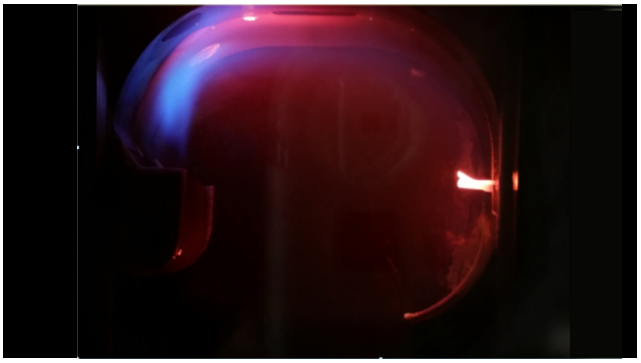

b.

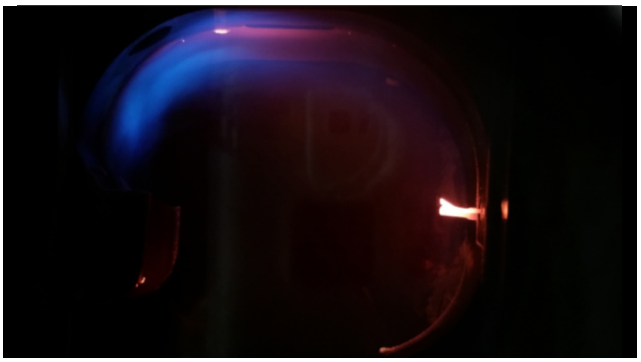

c.

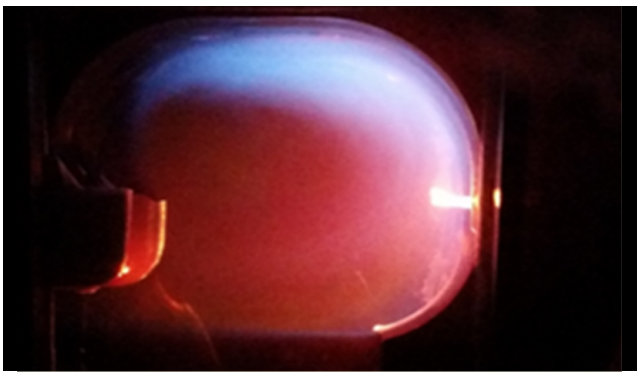

Figure 6.2: Photographs of the combustor for different amounts of N_2 addition [138]. For 0 LPM, 40 LPM and 100 LPM steps (from a to c). Fuel mass flow of $5.91 \cdot 10^{-5}$ kg/s. The incandescent filament on the right-hand-side is a thermocouple. Please note that the photographs are meant for visual representation only.

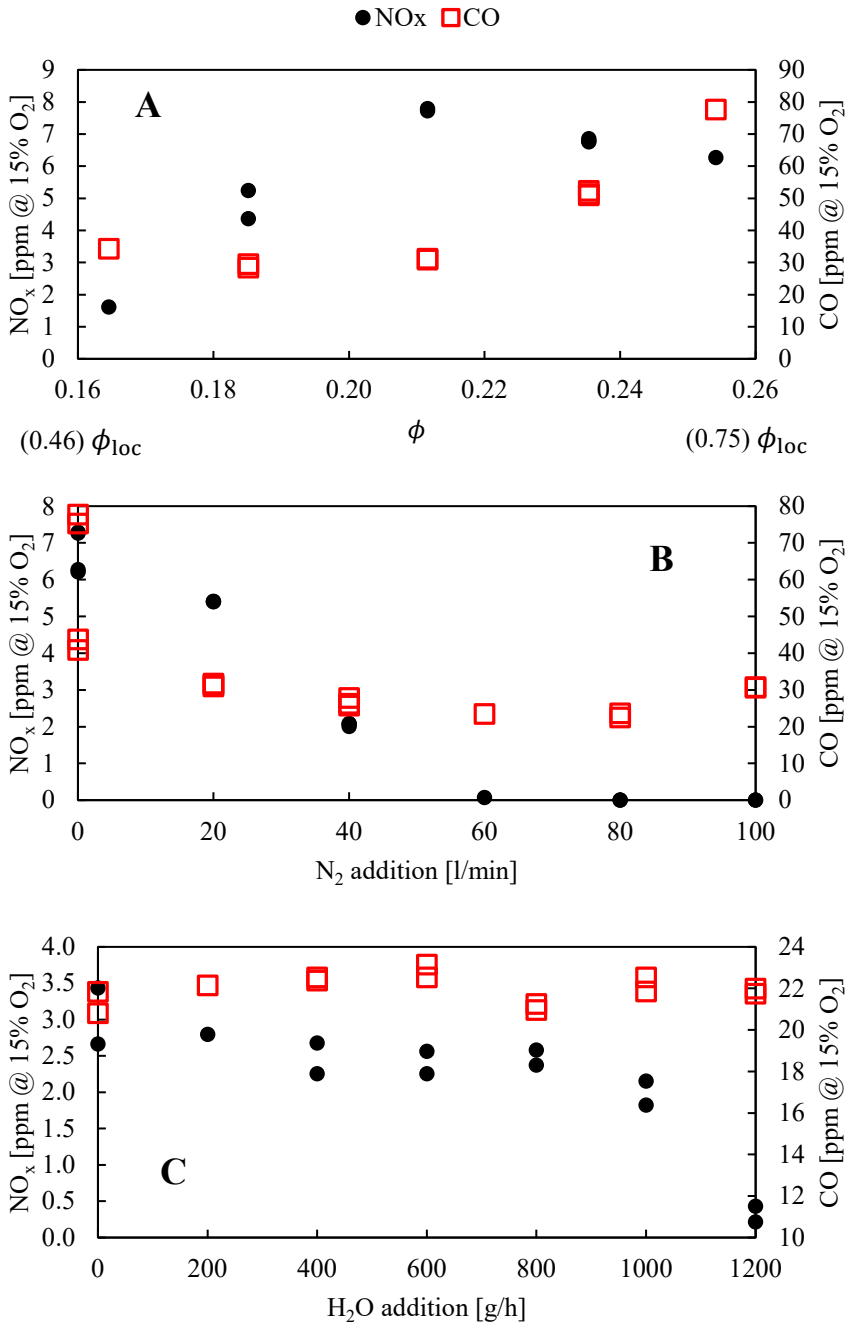

Figure 6.3: Experimental results of NO_x and CO emissions with a variation of global equivalence ratio A (values of local equivalence ratio also indicated), N_2 addition to the oxidiser B, and H_2O addition to the oxidiser C. [derived from 138].

Emissions of CO and NO_x for varying ϕ, N_2, and H_2O addition are summarized in Figure 6.3. There are multiple data points per operating condition, corresponding to different acquisitions. Interestingly, both CO and NO_x exhibit non-monotonic trend with varying ϕ, even though all conditions belong to the lean region (ϕ_{loc} ranged from 0.46 to 0.75). This behaviour is further discussed and explained in Section 7.1. The local equivalence ratio (ϕ_{loc}) is defined using the combustion oxidiser mass flow (excluding the dilution oxidiser). The behaviour with N_2 addition was in line with previous studies [140], as NO_x decreased with increasing N_2, while CO increased after a certain level of dilution. The addition of N_2 can primarily have two effects. The first is the reduction in the O_2 concentration which, as a consequence, reduces the value of the peak temperatures). The second effect is due to the reduction in the residence time. Water addition had little effect on the CO emissions, while it decreased NO_x emissions significantly. The modelling and analysis of the effect of H_2O addition will be treated in another upcoming publication.

6.3 Computational Modelling Objectives

The challenge of modelling reacting flows is often related to how simplifications and assumptions cause deviations in relation to the actual trends and how these deviations vary for different conditions. Throughout the years, many studies have been dedicated to investigating the effect of possible simplifications on premixed and diffusion flames. Obtaining models able to yield good results across a broad range of operating conditions is still a major challenge in combustion research. Furthermore, combustion modelling is more often focused on predicting flame structures rather than pollutant emissions.

The modelling presented herein was motivated by several objectives, namely:

- understanding the effect of dilution and equivalence ratio on the flowfield and pollutant emissions of the ITB;
- assess the performance of CFD regarding the prediction of pollutant emissions using simplified chemistry;
- assess the capabilities and limitations of CRNs in predicting emissions and in assisting the design;
- increase the understanding about the effects of recirculating combustion products on NO_x emissions;
- analyse the effect of using different chemical reaction mechanisms and operating conditions;
- provide useful insights aimed at the improving the ITB concept by combing the information provided by the two modelling approaches.

In order to achieve these objectives, the following sections describe and discuss the results of the different computational approaches.

6.4 CFD SIMULATIONS

The employed FGM approach, described in Section 3.3.2, was based on the creation of a diffusion flamelets manifold that is accessed during the CFD calculations, based on the local values of the chosen control variables. Both adiabatic and non-adiabatic formulations were employed, mixture fraction, a progress variable and enthalpy (for the non-adiabatic case) as the three control variables. The energy balance performed by taking the experimental data into account (temperatures at the inlet and at the outlet) suggested that the heat losses were not negligible, justifying the use of the non-adiabatic approach.

The standard k-ε turbulence model was employed as tests using the k-ω SST model and a Reynolds Stress turbulence model did not significantly change the results in terms of emissions. Heat conduction through the walls was included by imposing an estimated outer wall temperature, as well as their thicknesses and thermal properties. The properties of the quartz windows on the lateral domain were obtained from the work of Loenen and van der Tempel [141].

The computational mesh was refined until the difference in the computed emissions and in the temperature and velocity fields at mid-plane were deemed negligible. All meshes were hexahedral and the variation in the emissions as a function of mesh refinement can be seen in Figure 6.4. The employed computational mesh had approximately 5.6 million elements (Figure 6.5). The zone closest to the fuel injection port had finer refinement than other regions.

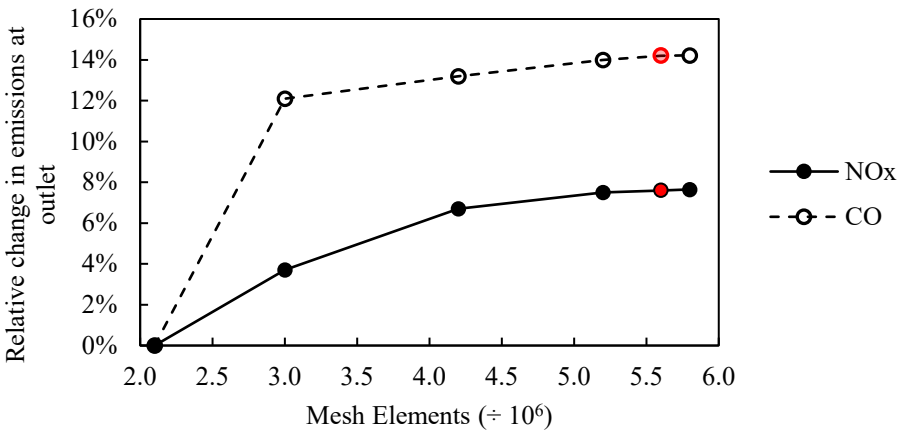

Figure 6.4: Variation in the emissions with mesh density (results for 2.1 million elements as reference). Data points in red indicate the utilized mesh.

Mass flows and composition were imposed at the domain inflow boundaries, with a turbulence intensity of 5%. The outlet boundary, where the resulting emission values were computed, was set to have zero mean relative pressure.

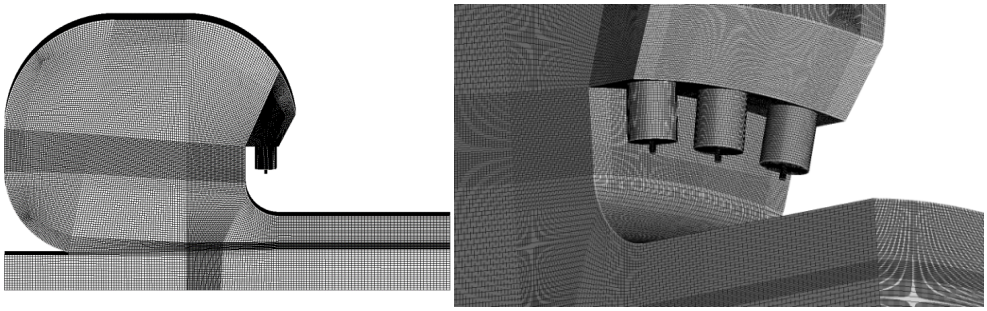

Figure 6.5: Computational mesh. Side view (left) and fuel injection region (right).

6.4.1 FLOW FIELD ANALYSIS

The obvious advantage of CFD is the characterization of the flow field, which can provide useful information regarding the combustor design. The experimental campaign did not entail any flow field measurements and thereby did not provide experimental data for model validation.

The results suggest that the mixing between dilution air and the stream coming from fuel and combustion air is inadequate (Figure 6.6 and Figure 6.10). The gradients persist up to the domain outlet and show nearly no interaction between the two streams. This behaviour was observed for all turbulence models. It is therefore clear that the interaction between the streams should be increased to improve mixing and to obtain the desired temperature pattern factor at the turbine inlet situated downstream of the combustor.

The plots also show an undesirable behaviour: most of the reactions take place near the combustor walls and not in the recirculation zone, contrary to what was intended. This behaviour would cause problems to the durability of the combustor walls (due to the complex flame-wall interaction) and would lead to increased CO emissions due to quenching.

In order to quantify the recirculation of combustion products, a recirculation ratio was calculated. Similar to the procedure adopted by Melo et al. [80], the recirculation ratio *RR* is defined by Eq. 6.1, in which *A* is the area of the surface shown in Figure 6.7. The surface was defined as follows: the centre of the recirculation zone (where velocity is zero) in the central plane of the combustor was taken (shown by the dot in Figure 6.7). This point defined the upper limit of the vertical surface, while the horizontal surface was defined by the position where the flow split along the wall (highlighted in the lateral view of Figure 6.7).

$$RR = \frac{\int_A \rho \mathbf{V} \cdot \mathbf{N} dA}{\dot{m}_{\text{oxid}} + \dot{m}_{\text{fuel}}} \qquad \text{Eq. 6.1}$$

The defined RR is therefore the ratio between the mass flow of recirculated products and the total mass flow rate. To neglect the effect of the dilution oxidiser stream, a local recirculation ratio (RR_{loc}) is also defined, and it only takes into account the oxidiser mass flow rate injected along with the fuel.

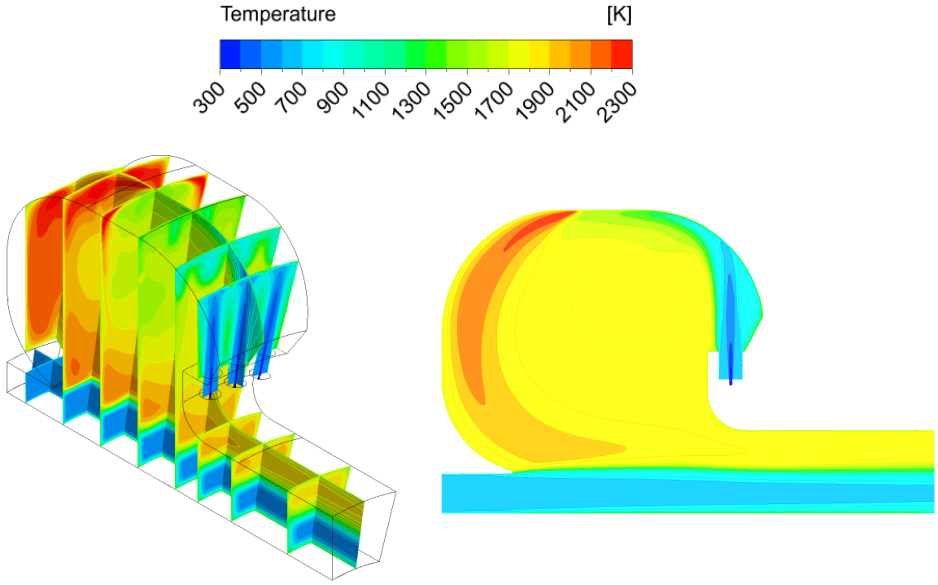

Figure 6.6: Temperature field with ϕ = 0.235. Non-adiabatic CFD simulations.

The values of RR and RR_{loc} for different Φ are shown in the plot of Figure 6.8. The overall values of RR are low if compared to those of the FLOXCOM [80], which were between 0.34 and 1.12. Although it makes more sense to compare these values to those of RR_{loc}, as the FLOXCOM did not feature any oxidiser split, the values in the 0.5-0.7 range are also considered suboptimal to attain FC [34]. The most important conclusion that can be drawn from Figure 6.8 is that the dilution oxidiser stream has almost no influence on the recirculation: the trends of RR and RR_{loc} are similar, with the dilution stream slightly increasing RR only for the highest values of ϕ. The recirculation is larger for lower ϕ due to the increase in the overall mass flow, which increases the jets momenta and, consequently, the induced recirculation.

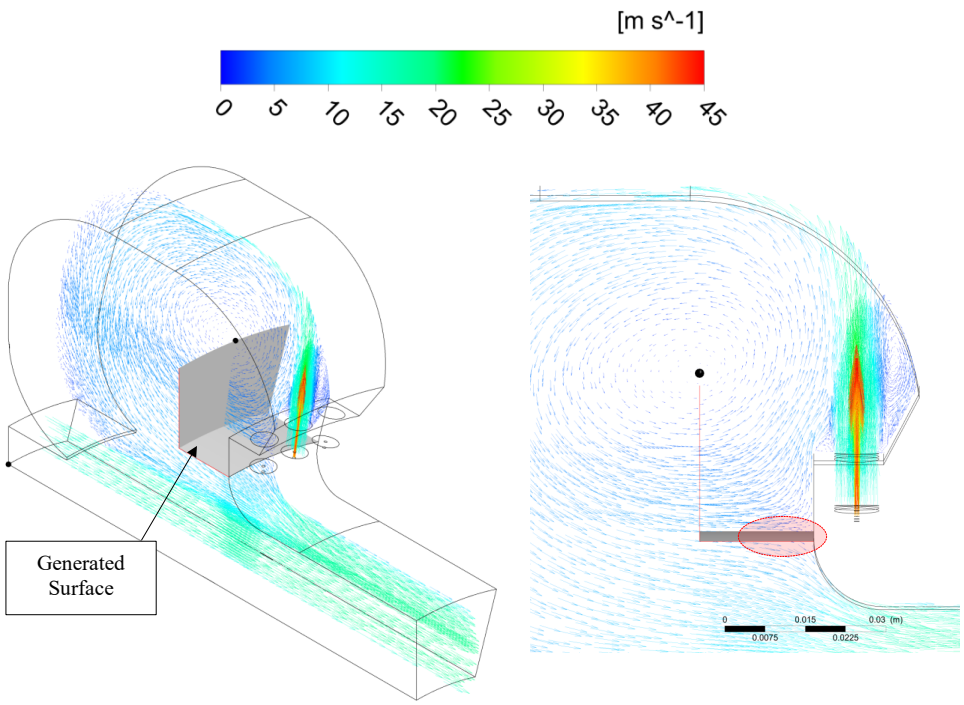

Figure 6.7: Example of a defined surface for the calculation of the recirculation ratio for the case with ϕ = 0.254. Velocity vectors on the central plane of the combustor. The dot depicts the centre of the recirculation zone, where velocity is equal to zero. Isometric (left) and lateral (right) views.

By analysing the resultant Da distribution from the CFD simulations (Figure 6.9), it can be seen that the Da decreases significantly (close to unity) with the addition of N_2. Thereby, supporting the observation that the combustor was operating in the FC regime during the experiments with high N_2 dilution, especially with 80 and 100 LPM N_2. The Da is often adopted as an indicator of the FC regime [38]. Values of Da close to unity denote that neither the chemistry nor the mixing (or turbulence) are limiting and governing the reaction progress, as the two time-scales are comparable. The Da is calculated as shown in Eq. 6.4, where the formulation present in the Zimont model [142] is used to estimate the turbulence time-scale (Eq. 6.2).

$$\tau_t = \frac{l_t}{u'} = \frac{0.37(u'^3/\varepsilon)}{u'} = 0.37\left(\frac{2}{3}\right)\left(\frac{k}{\varepsilon}\right) \quad \text{Eq. 6.2}$$

$$\tau = \frac{\alpha}{s_L^2} \quad \text{Eq. 6.3}$$

$$Da = \frac{\tau_t}{\tau} = \frac{0.37(2/3)(k/\varepsilon)}{\alpha/s_L^2} \qquad \text{Eq. 6.4}$$

The addition of N_2 lowers the values of Da, going from maximum values across the whole domain of above 20 (without N_2) to around 5 (with 80 LPM of N_2) and below 3 (with 100 LPM of N_2). Mean Da values in the combustion zone (excluding the dilution air and exhaust regions) were close to unity in the case with 100 LPM of N_2. The plausibility of the results of the simulations are supported by the photographs taken during the experiments (Figure 6.2). The blue regions in the photographs mark the reaction zones, which gradually move downstream with increasing N_2 addition. At the maximum level of N_2 addition (100 LPM on Figure 6.2), the photograph shows the most distributed reaction zone with increased red luminosity coming from the walls, a characteristic that is often observed when FC is attained. Moreover, the reaction zones are shown to be located along the combustor walls, as predicted by the simulations.

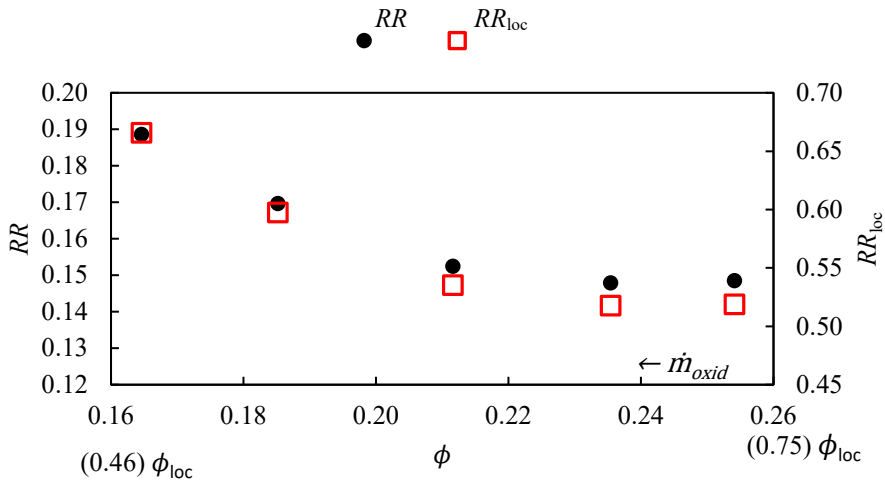

Figure 6.8: Recirculation ratio and local recirculation ratio as functions of the global equivalence ratio.

Given the results of both simulations and experiments, it is likely that the dilution of the oxidiser stream with N_2 causes the combustor to operate under the FC regime. The attained level of dilution at the inlet during the experiments was lower than the predicted operational dilution of the dual combustor system [18]: while the most diluted case shown in Figure 6.9 has 17.5% O_2 (mass), the ITB is predicted to operate between 10 to 15.5% O_2. Therefore, it is even more likely that the combustor would operate under FC regime in the actual operation. In the actual application, H_2O is responsible for the dilution along with CO_2, in case CH_4 is employed in the main

combustor. The different heat capacities between N_2, H_2O and CO_2 may alter the behaviour of the combustion zones for the same amount of dilution.

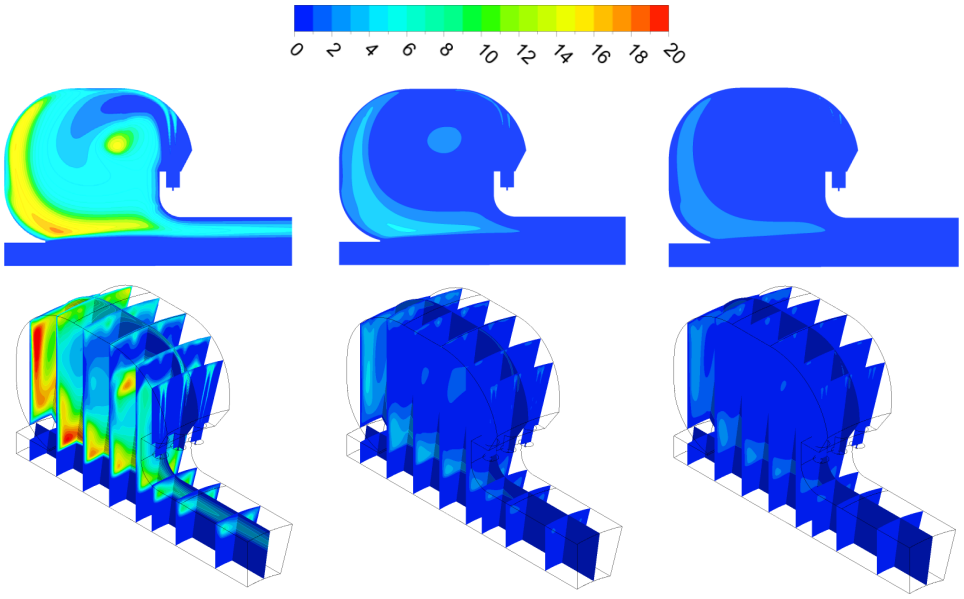

Figure 6.9: Calculated Da for the without nitrogen addition (left), with 80 LPM N_2 addition (middle) and 100 LPM (right). Lateral (up) and isometric (down) views. Non-adiabatic CFD simulations.

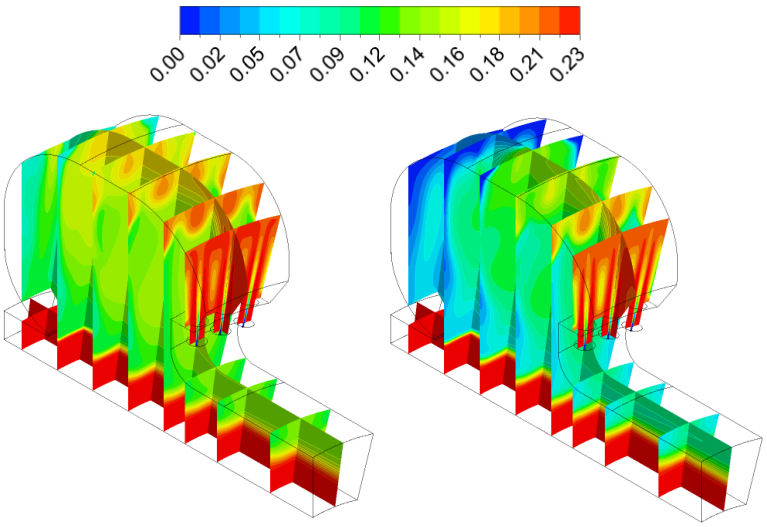

Figure 6.10: The O_2 mass fraction for two different equivalence ratios with no air dilution. ϕ = 0.165 (left) and ϕ = 0.235 (right). Isometric view. Non-adiabatic CFD simulations.

The comparison between different ϕ shows that the combustor performance may be greatly affected by the split between combustion and dilution air since the mixing between the two streams is not intense. While the lowest value of ϕ in Figure 6.10 indicates an excess of O_2 throughout the whole combustor, the increase in ϕ creates undesirable regions with no O_2. Although such result may be the reason for the overprediction of CO emissions discussed in Section 6.6 (being therefore inaccurate), further studies should be performed to ensure that the designed air split is adequate for the whole operational range of the combustor.

6.5 Chemical Reactor Network of the ITB

Having the flow field results from the CFD, a CRN was designed to represent the flow inside the ITB. The combustor volume was subdivided into ideal reactors based on the temperature and composition gradients. The velocity field helped in determining the volume of the reactor representing the central recirculation zone. The amount of recirculation was also estimated by the composition and velocity fields.

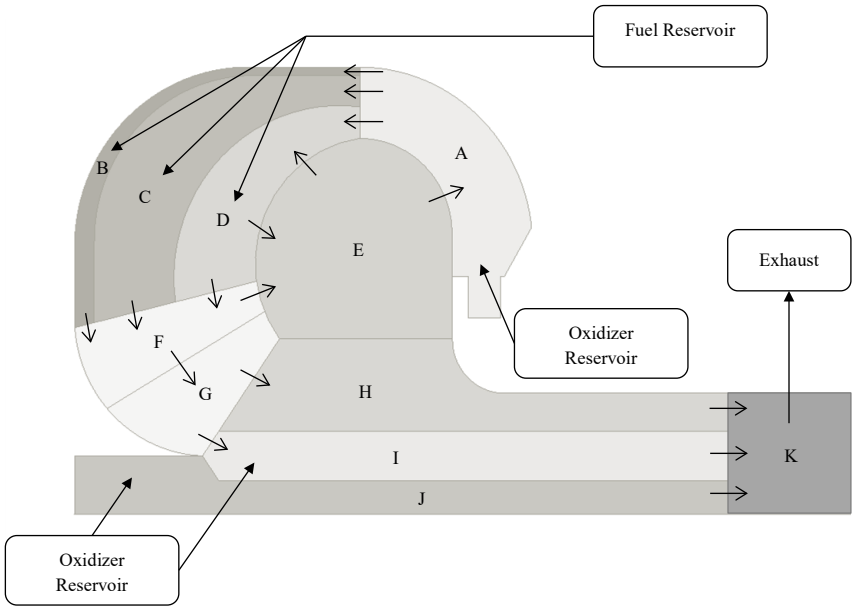

Figure 6.11: Regions of the inter-turbine combustor divided into idealized reactors in the designed CRN.

After some iterations, the regions depicted in Figure 6.11 were established. Each region was represented by a Perfectly Stirred Reactor (PSR). The CRN was modelled and solved using the open-source code Cantera [36], as described in Section 3.4. The connections between the reactors and the structure of the CRN can be seen in Figure

6.12. The given names to the reactors on Figure 6.12 represent the behaviour observed in the CFD simulations in each region.

Total heat losses were calculated based on the inlet and outlet temperatures measured during the experiments. As the lateral windows were made of quartz and were much thinner than the other walls, it was assumed conduction took place only across the lateral windows. Therefore, the allocation of heat loss was dependent on the temperature reached in each reactor and on their lateral areas.

The GRI 3.0 mechanism [37] was employed to determine reactions and their rates in the CRN. As previous works reported the tendency of this mechanism to overpredict NO_x emissions, the GRI 2.11 [143] was also employed in order to draw a comparison, as literature indicates a better performance in terms of NO_x emission [144-146]. The difference between the two mechanisms is attributed to the different rates obtained for the Prompt NO_x formation. A comparison with other mechanism is shown in Section 7.3.

The disabled reactions to account for the contribution of each formation pathway are shown in Appendix A. As shown in Section 6.7, the errors were low as emission values obtained by the sum of the calculated contributions is close to the total without any disabled reaction.

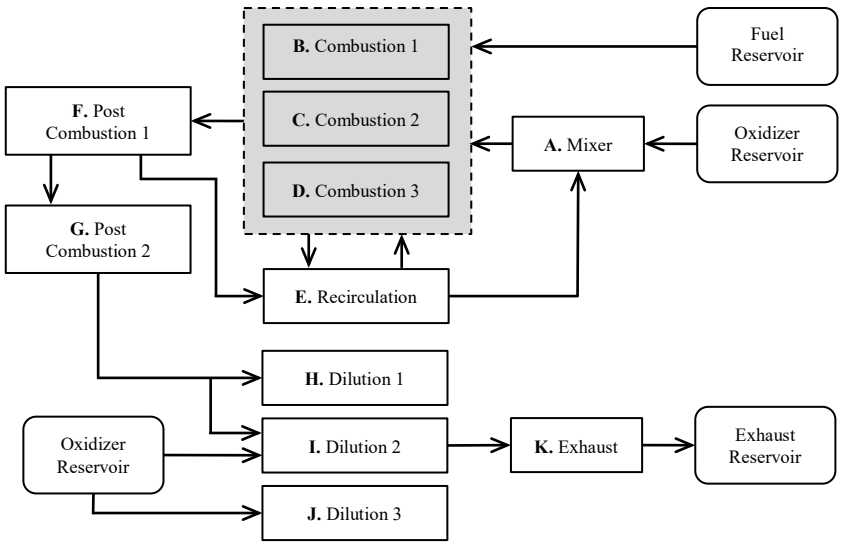

Figure 6.12: Structure of the designed CRN.

The conceptual design of the ITB took the important role of reburning into account, as the NO_x generated in the main combustor would be present in the oxidiser streams of the inter-turbine combustor. However, the oxidiser utilized during the experiments did not contain any NO_x and reburning took place due to recirculation within the

combustor. The occurrence of reburning in FC conditions has been identified and discussed in the literature [147].

6.6 Comparison between CFD and CRN

The results obtained with both the CFD and the CRN simulations in relation to overall emissions can be summarized as shown in Figures 6.13 to 6.16. In these figures, prediction of emissions for the adiabatic and non-adiabatic CFD cases are shown along with the CRN results for both the GRI 3.0 and the GRI 2.11 chemical mechanisms.

The results for CO (Figures 6.13 and 6.15) show that the CFD simulations overpredict the emissions. The non-monotonic behaviour present in the experiments is not captured by the simulations. The overprediction is either a result of limitations in the formulation of the employed FGM model or in the prediction of the mixing between the streams. The definition of the progress variable as a function of CO mass fraction could also be a source of error. However, the use of H_2O mass fraction to define the progress variable provided worse results. On the other hand, the CRN results are very close to the experimental CO data, with little difference between the two chemical mechanisms, although the GRI 2.11 provides marginally better predictions.

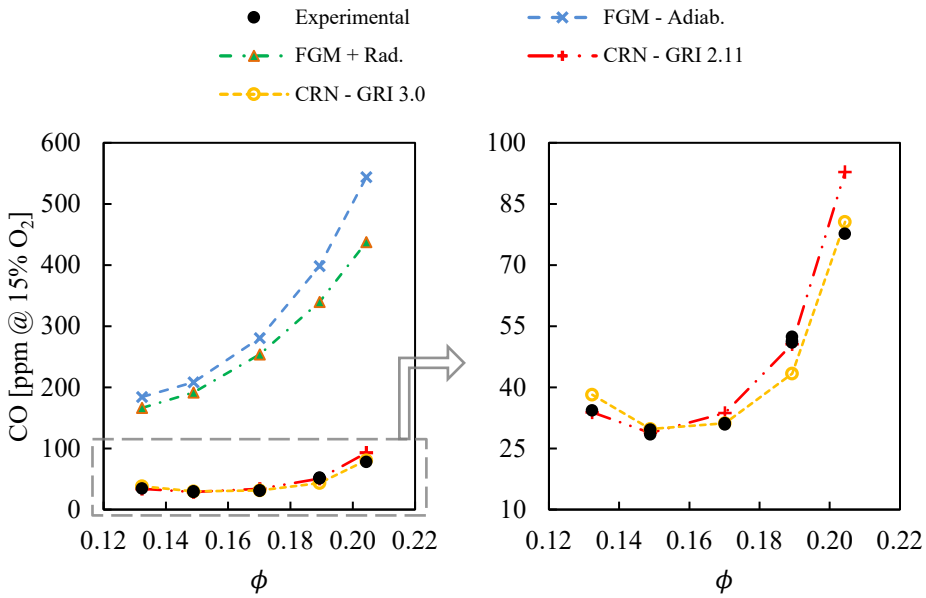

Figure 6.13: CO emissions as a function of the global equivalence ratio. Comparison between experimental data [121] and modelled results.

In the case of NO_x emissions (Figures 6.14 and 6.16), the adiabatic FGM highly overpredicts the values. Such behaviour is expected, as heat losses were present in the experiments and NO_x emissions depend on the peak temperatures. The non-adiabatic CFD approach has better agreement, being the best amongst the four cases in capturing the effect of N_2 addition (Figure 6.16). However, it fails to predict the non-monotonic trend of NO_x emissions with increasing equivalence ratio (Figure 6.14).

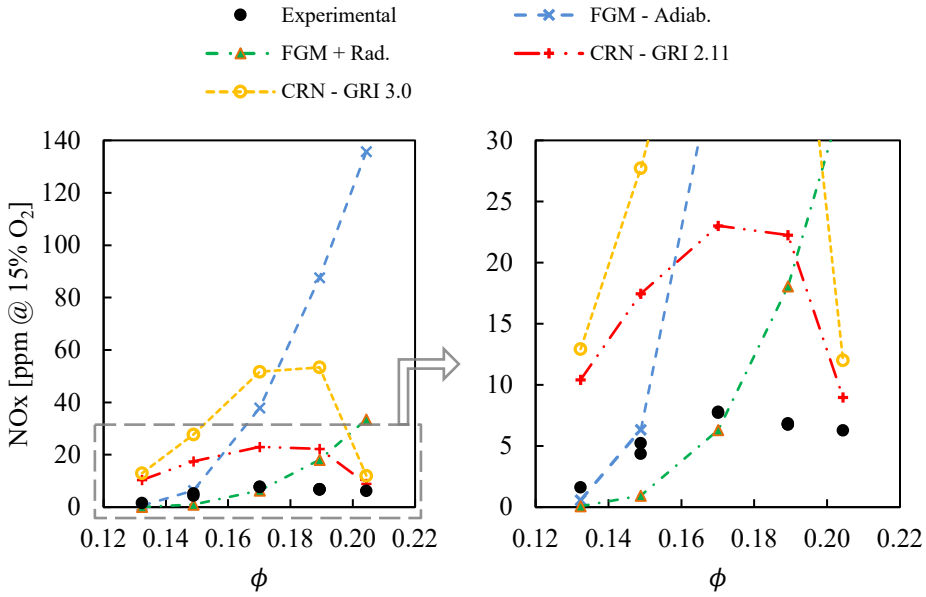

Figure 6.14: NO_x emissions as a function of the global equivalence ratio. Comparison between experimental data [121] and modelled results.

The NO_x behaviour is captured by the CRN for variations of ϕ and N_2 addition. In accordance with previous works, the GRI 3.0 yields values as high as 10 times the experimental data points. Therefore, the best prediction for NO_x with a variation of equivalence ratio is obtained from the CRN with GRI 2.11, although still overpredicted. The unusual non-monotonic behaviour of NO_x with increasing equivalence ratio can be explained by analysing the NO_x formation pathways, presented in Section 6.7.

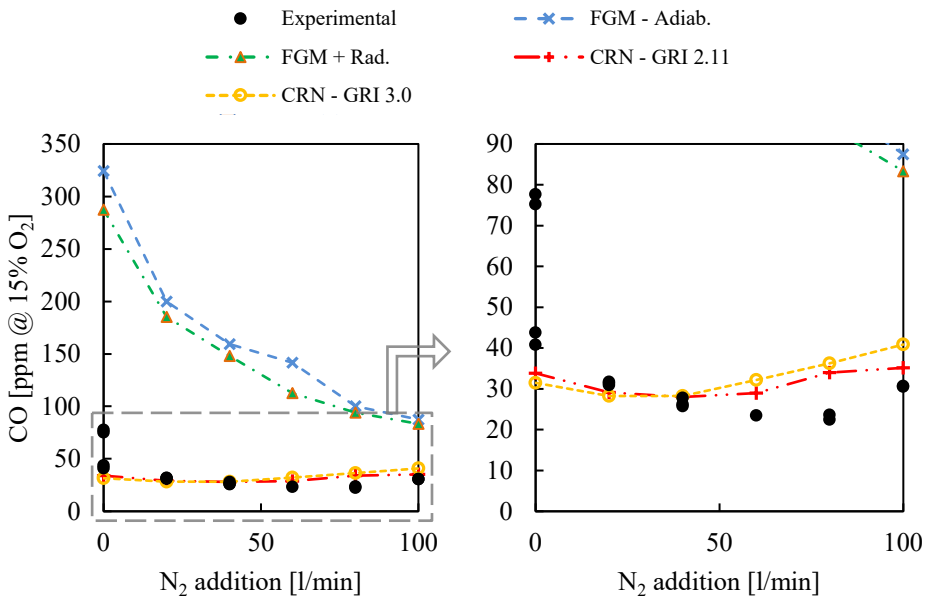

Figure 6.15: CO emissions as a function of N_2 addition to the oxidiser. Fixed fuel and air mass flow. Comparison between experimental data [138] and modelled results.

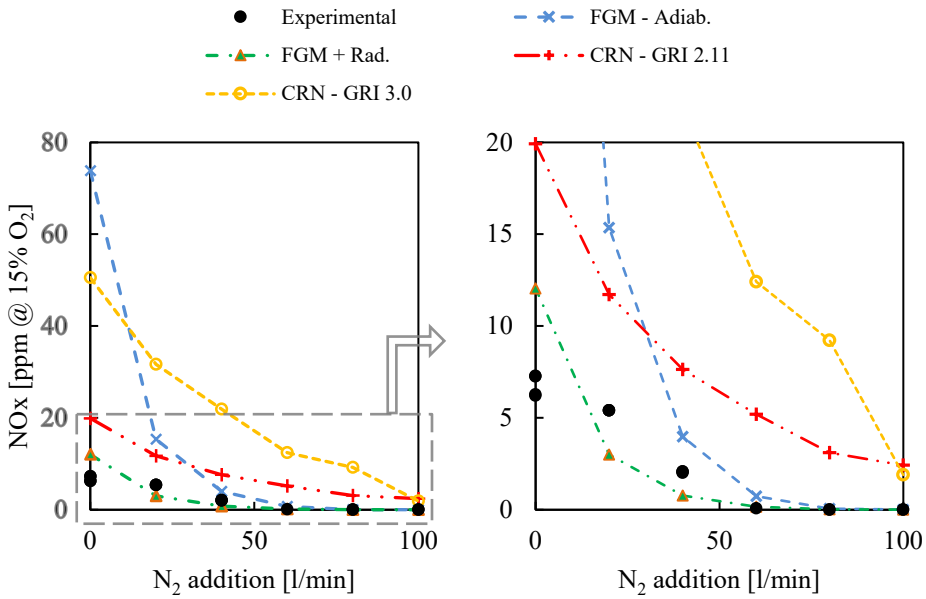

Figure 6.16: NO_x emissions as a function of N_2 addition to the oxidiser. Fixed fuel and air mass flow. Comparison between experimental data [138] and modelled results.

6.7 NO_x Formation Analysis

The detailed chemistry incorporated in the CRN allows detailed analysis of the contributions from the different NO_x formation pathways. Figure 6.17 presents the relative and absolute contributions of the NO_x formation pathways to the overall NO_x emissions as a function of ϕ. Interestingly, the contribution of the thermal pathway is minor and, to some extent, constant across all conditions.

The comparison of the emission values predicted with the full GRI 2.11 mechanism and the sum of the calculated contributions in Figure 6.17 shows that the largest deviation occurs in cases where the dominant pathways shift (around $\phi = 0.21$ and $\phi = 0.24$). The contributions of prompt NO formation and NO-reburning are the key differences in relation to the NO_x emission at other equivalence ratios. Therefore, the interplay between prompt and/or reburning with other pathways appear to be significant. One could argue that the calculation of NO-reburning is probably responsible for the deviations, as more reactions have to be deactivated.

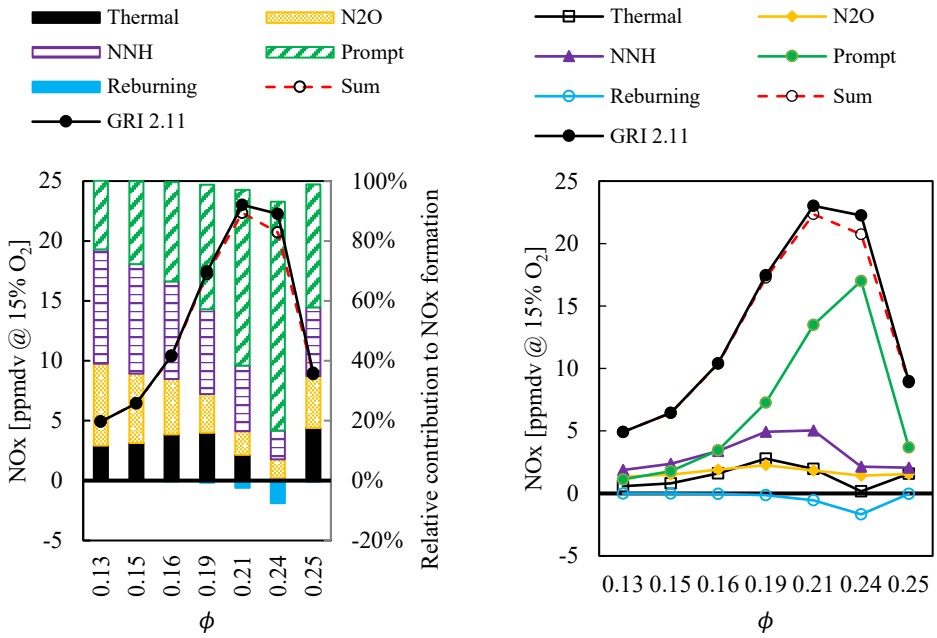

Figure 6.17: Relative (left) and absolute (right) contributions of NO_x formation pathways for different global equivalence ratios. Results from the CRN model with the GRI 2.11 mechanism.

The overall behaviour of the NO_x formation is dominated by prompt NO_x. The initial NO_x increase with ϕ can be attributed to the prompt pathway, with a smaller contribution of the NNH pathway. Subsequently, NNH drops when prompt reaches

its peak (around ϕ = 0.24). A further increase in equivalence ratio reduces both NNH and prompt pathways, as well as increases reburning, reducing the overall NO_x production.

The behaviour of prompt NO_x in the CRN can be explained by analysing the Combustion PSRs (presented in Figures 6.11 and 6.12), where the most important reactions take place. A plot of the C/O mass ratio excluding CO_2 and H_2O (which indicate complete combustion) is shown in Figure 6.18 for the three PSRs. The C/O ratio in Combustion 2 zone always increases with increasing ϕ. On the other hand, The C/O ratio in the Combustion 1 reactor has similar trend to that of prompt NO_x formation, decreasing for the highest ϕ. The C/O ratio may be regarded as a local equivalence ratio, neglecting the products of complete combustion. It aids the analysis since it is difficult to assess each reactor based on inlet values, as the CRN was designed with several recirculations and interplays between the PSRs.

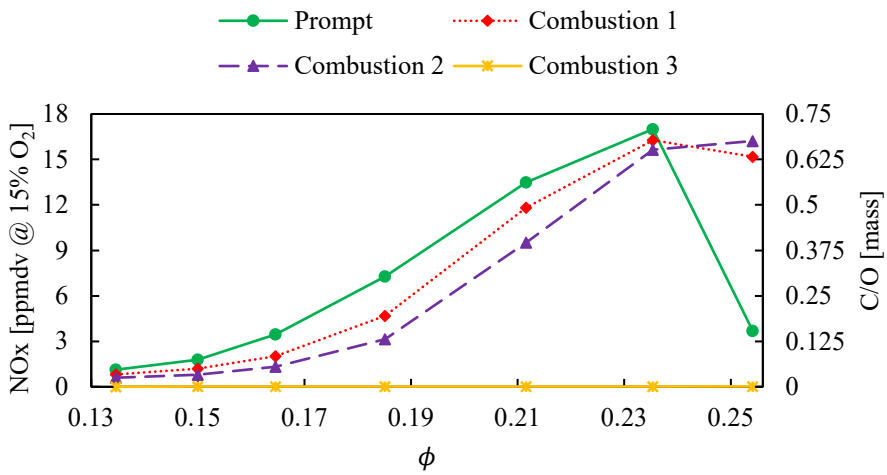

Figure 6.18: Prompt NO_x emissions and the C/O mass ratio (excluding H_2O and CO_2) for the Combustion PSRs as functions of the global equivalence ratio using the GRI 2.11 mechanism.

In order to further analyse prompt NO_x formation, the intermediate species HCN and CH are the most important [148,149]. The plots of their mass fractions in the Combustion 1 and 2 PSRs is presented in Figure 6.19. The results once again point to the importance of the reactions taking place in the Combustion 1 PSR, as both HCN and CH peak at the value of ϕ in which prompt emissions are the highest and drop dramatically with further increase in ϕ. Both species exhibit considerably lower concentrations in the Combustion 2 reactor and, while CH behaves similarly to the Combustion 1 reactor, HCN always increases with increasing ϕ. Therefore, it can be concluded that the overall NO_x behaviour of the combustor is governed by the prompt pathway taking place in main reaction zone, close to the combustor wall.

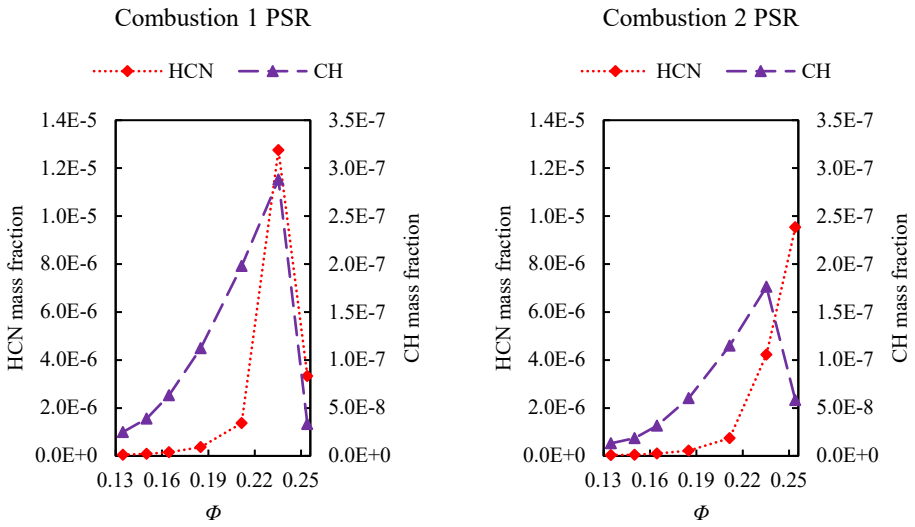

Figure 6.19: The mass fractions of HCN and CH in the Combustion 1 (left) and Combustion 2 (right) PSRs as a function of the global equivalence ratio, using the GRI 2.11 mechanism.

6.8 SUGGESTED ITB DESIGN MODIFICATIONS

The simulation results allow for the assessment of the designed combustor. Two undesirable features were observed through the simulations and, to some extent, with the experiments: i) most reactions take place close to the combustor walls and ii) the dilution oxidiser does not enhance the recirculation within the combustor and does not mix properly with the products before leaving the combustor.

Figure 6.20 shows the dimensions that may be modified in order to improve the performance of the combustor. The direction of the fuel and combustion air streams (denoted by the angle θ), as well as the velocity of the jets, cause the reactions to occur close to the walls. The mixture impinges upon the combustor walls at high velocities. Reducing the velocity by increasing the diameter of the fuel (d) and oxidiser (D) ports could be an option, but with the drawback of hindering the mixing between the streams due to the lower jet momentum. Altering the injection angle should also be considered, especially by making it point towards the intended recirculation zone.

Regarding the effect of the dilution oxidiser, more complex modifications may be required. The designed split between combustion and dilution air was based on the assumption that dilution air would interact and enhance the recirculation, thereby homogenizing the flow leaving the combustor. The increase in the relative amount of dilution air would probably enhance the mixing and could be performed by altering the ratio between r_1 and r_2. However, it would be unlikely that the problem can be solved without further modification of the geometry. An interesting option is to

change the direction of the dilution oxidiser flow by adding an obstacle between the dilution air inlet and the outlet of the combustor, as shown by means of the patterned area in Figure 6.20. The shape and dimensions (L and H) of this obstacle should be studied to enhance interaction with the recirculation zone while not excessively increasing pressure losses.

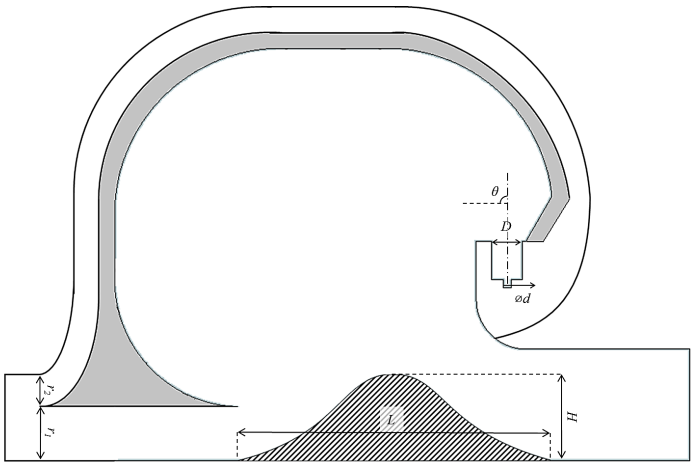

Figure 6.20: Dimensions that can be modified in order to improve the combustor design.

6.9 CONSIDERATIONS & CONCLUSIONS

This chapter reports computational calculations related to the ITB of the dual combustor concept for gas turbine engines, designed to operate under the FC regime. The modelling was performed using the CFD and the CRN computational methods and the results were compared to experimental data of CO and NO_x emissions.

The conclusions related to this work may be summarized as follows. As far as the modelling is concerned,

- the CRN model had a better performance calculating the pollutant emissions from the FC combustor than the CFD model;
- the different levels of oxidiser dilution with N_2 lead the transition towards FC regime, as evidenced by the low Da resulting from the simulations and from the spreading of the reaction zone observed during the experiments;
- both CFD and CRN should be used when designing the ITB, especially when pollutant emissions are important.

With respect to the NO_x formation in the ITB, it can be concluded that

- the Prompt NO_x formation mechanism is the dominant pathway and determines the overall of NO_x emissions behaviour. The thermal pathway

has a relatively low contribution, being less important than the NNH and N_2O-intermediate pathways;

- the role of prompt NO_x was shown to be prominent in the ITB experiments at atmospheric pressure and relatively low reactants temperature;
- the analysis was performed for CH_4 and at atmospheric conditions. Therefore, the implications of these simplifications should be further investigated.

With respect to the ITB performance and design, the main conclusions are:

- both CFD simulations and experiments point to the occurrence of reactions close the combustor walls and not within the large recirculation zone, as envisioned by the conceptual design. Modifications in fuel injection position and direction, as well as air split, should be considered to improve the ITB design;
- the ITB design may be improved by assuring that the reactions take place in the main recirculation zone and that the dilution oxidiser stream is well-mixed before leaving the combustor;
- the split of oxidiser between primary and dilution zones has more complex consequences in combustors with high recirculation than in conventional combustors. Apart from influencing the amount of recirculation, the split also influences the chemistry of pollutant species.

Chapter 7 Effects of Operating Conditions on the ITB Emissions

In this chapter, the modelling approach described in Chapter 6 is adopted to further investigate the chemistry of FC, and to understand the effect on different ITB operating conditions. Additionally, other chemical reaction mechanisms are treated and their deviations are analysed. The combustion of CH_4 is considered. The chapter begins with an overview of the state of knowledge about NO_x formation under the FC regime in order to provide context and perspective.

7.1 CHEMICAL KINETICS UNDER THE FC REGIME

The lower NO_x emissions under the FC regime are caused by the more homogeneous reaction zones that abate thermal NO_x, by the reduction in the availability of the species involved in NO_x formation (especially O_2), and due to the effect on the production of NO_x through the NNH, N_2O-intermediate and prompt formation pathways. However, the ways in which the pathways are influenced under FC and what parameters govern such influence are not yet fully understood.

Nicolle and Dagaut [147] showed interesting results related to NO_x formation by using Partially Stirred Reactor calculations. The authors highlighted that the contribution of the N_2O pathway is as important as that of thermal NO_x. In addition, they demonstrated that the contribution of both the NNH and the prompt pathways are also relevant. The occurrence of NO reburning was also relevant. The high recirculation of combustion gases, usually present in FC systems, increases NO reburning. Since the first studies on FC [32], different chemical mechanisms to take reburning into account have been proposed [150,151].

For conventional gas turbine combustors, the thermal (or Zel'dovich) pathway is constantly pointed as the dominant source of NO_x, with minor contributions of prompt and N_2O-intermediate pathways, the latter for leaner conditions [52,53]. The conditions for increased N_2O impact were already associated with more distributed conditions (in studies not related to FC), as described by Correa [53]. However, the formation (and destruction) of NO_x can occur through more pathways, as treated in the recent review by Glarborg et al. [152]. The authors included the NNH pathway, NO reburning, as well as the oxidation mechanisms of HCN, HNCO and NH_3 (as fuel-NO_x subsets), to the thermal, prompt and N_2O pathways.

It has been shown that NO_x emissions may display a non-monotonic behaviour with increasing equivalence ratio, with the peak being at lean equivalence ratios in

---

Contents of this chapter appeared in:

Perpignan AAV, Rao AG. *Effects of chemical reaction mechanism on NO_x formation pathways on an Inter-Turbine Burner*. The Aeronautical Journal 2019; 1-21. DOI: https://doi.org/10.1017/aer.2019.12

systems in which the FC regime is attained via high recirculation of combustion products. It is known that NO_x emissions usually peak on the lean side with changing equivalence ratio, but just adjacent to stoichiometry [153], as the competition between fuel and nitrogen for O_2 to oxidize reduces NO_x at stoichiometry. The behaviour shown by some FC applications is, however, at leaner values, as shown in Figure 7.1.

The three systems utilized to derive the results shown in Figure 7.1 have significant differences between each other. Veríssimo et al. [62] utilized a cylindrical combustion chamber with a jet-based burner, in which the central air jet was surrounded by 16 CH_4 jets. The prismatic combustion chamber utilized by Sorrentino et al. [154] is characterized by a large central recirculation zone and relatively high residence times. Air and C_3H_8 were added to the chamber via pipes positioned in two opposing corners of the chamber. Figure 7.1 also displays the results for the ITB presented in Section 6.2. Despite being different, all combustors were aimed at attaining FC and showed a similar NO_x emissions trend with respect to ϕ.

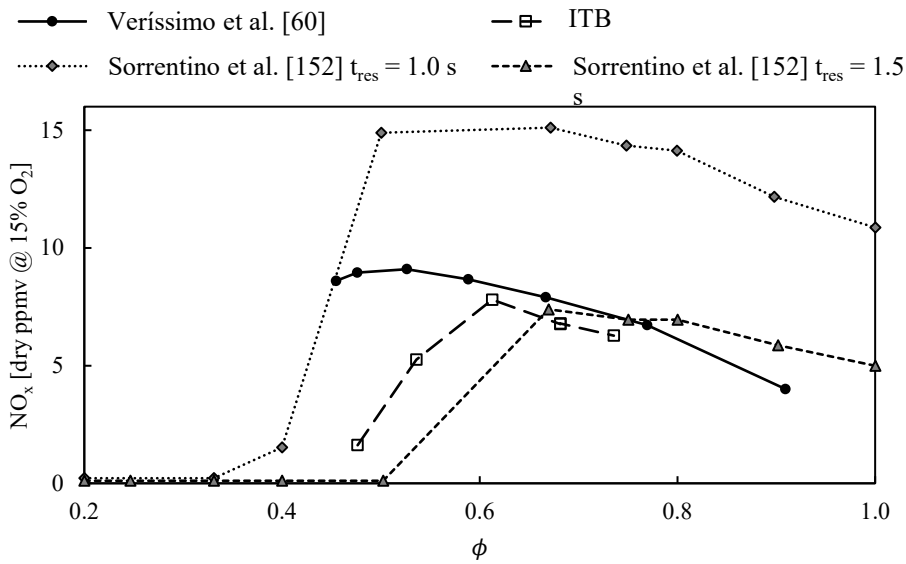

Figure 7.1: Measured NO_x emissions as a function of the equivalence ratio for three different systems with high recirculation: a combustion chamber with jet-induced stabilization [62], the ITB, and a cyclonic prismatic chamber for two different estimated residence times [154]. The values related to the ITB are plotted as a function of the local equivalence ratio, and not of the global equivalence ratio, as defined in Section 6.2.

The authors, however, provided different explanations for the observed trends in each case. Veríssimo et al. [62] pointed to a switch between FC and conventional lean combustion caused by mixing characteristics between the burner jets and the recirculating combustion products. Sorrentino et al. [154] explained that higher temperatures were attained in the prismatic combustion chamber at higher equivalence ratios, which activated NO reburning. Lastly, the results treated in

Section 6.7 demonstrated the prominent role of prompt NO_x formation with respect to the non-monotonic behaviour observed for the ITB emissions.

The following sections describe the effects of recirculating combustion products, to compare the performance of chemical reaction mechanisms for CH_4 combustion, and to provide insights into the effect of T and p on the NO_x emissions of the ITB. The study was performed by utilizing CRNs and the modelling approach described in Section 3.4.

7.2 FOUR-REACTOR CRN

In order to provide further understanding about the effects of recirculating combustion products on NO_x emissions, a simple CRN was developed to systematically evaluated the effect of recirculation, equivalence ratio and residence times on NO_x emissions behaviour. As discussed in Section 7.1, the recirculation of combustion products employed to attain the FC regime is one of the main factors involved in the reduction of NO_x.

However, its effects are not fully understood, and to elaborate on the involved phenomena, a simple CRN composed of 4 PSRs was developed to showcase the effect of recirculation and equivalence ratio on NO_x emissions (Figure 7.2). Moreover, the simple model enables the discussion of some of the results attained with the ITB model. The names of the PSRs in Figure 7.2 are merely representative of the expected function each PSR is expected to have in the simulations. The combustor PSR was assigned 75% of the total volume, while the mixer, outlet and recirculation PSRs were assigned 15, 6 and 4% of the volume, respectively. Different total volumes were assigned in order to assess the effect of residence time. Heat losses were included since they are present in virtually every experimental investigation related to FC (including the experiments whose Figure 7.1 refers to). Losses play an important role in NO_x formation under FC, especially due to their effect on the thermal pathway. All simulations of this CRN were performed using the GRI 3.0 mechanism.

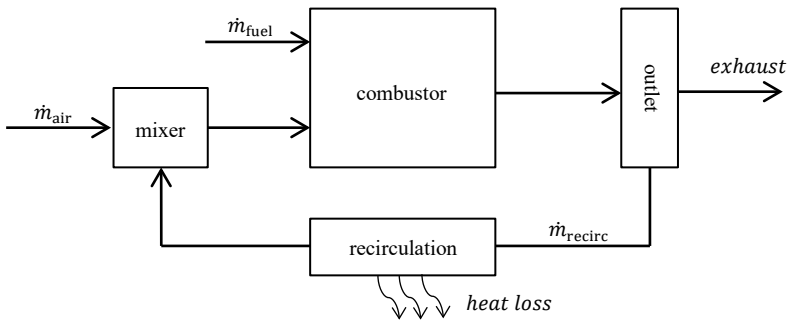

Figure 7.2: Scheme of the CRN designed to investigate the effect of recirculation of products in the behaviour of NO_x emissions.

Different values of ϕ were tested. The total amount of mass flow was kept constant, causing both air and fuel mass flows to be different for each value of ϕ. The amount of recirculation was quantified by the recirculation ratio (RR), as shown in Eq. 7.1.

$$RR = \frac{\dot{m}_{recirc}}{\dot{m}_{air} + \dot{m}_{fuel}} \qquad \text{Eq. 7.1}$$

7.2.1 FOUR-REACTOR CRN RESULTS AND LIMITATIONS

The four-reactor CRN results are shown first in order to discuss some general aspects of combustion systems with high recirculation and the difficulties in modelling emissions in such systems. Examining the effect of recirculation, an increase in RR for the same value of T_{in} and ϕ may increase or decrease NO_x. Additionally, the influence of RR on the absolute values of NO_x is quite low for the settings used to generate the plots in Figure 7.3. The differences caused by RR is less than one ppm.

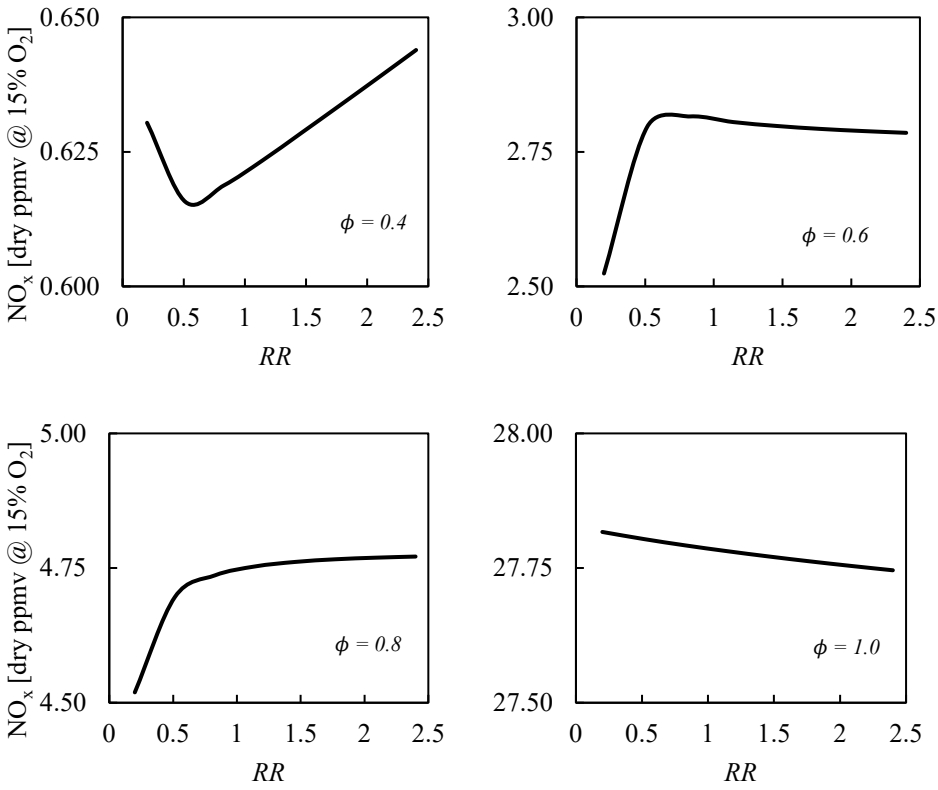

Figure 7.3: NO_x emissions as a function of RR for the four-reactor CRN. Four different ϕ. Mean residence time = 0.12 s. T_{in} = 600 K.

Nevertheless, by analysing the results of Figure 7.3 it is possible to notice that recirculation of products has two competing effects: on the one hand, the composition of the products tend to reduce reaction rates of the incoming reactants, on the other, the products are predicted to reach high temperatures, which tends to increase reaction rates. This explains why, in the leaner cases, higher *RR* tends to increase NO_x, as combustion products contain larger amounts of O_2 and N_2 available for the oxidation.

The sub-ppm changes in NO_x emissions with changing *RR* in this CRN model can be explained by the large relative size of the combustor reactor and the very assumption underlying a PSR, namely perfect and instantaneous mixing. The large volume of the reactor causes most of the reactions to take place in that reactor. Therefore, the temperature rise occurs in the reactor and adding combustion products has little influence on the heating of the incoming reactants.

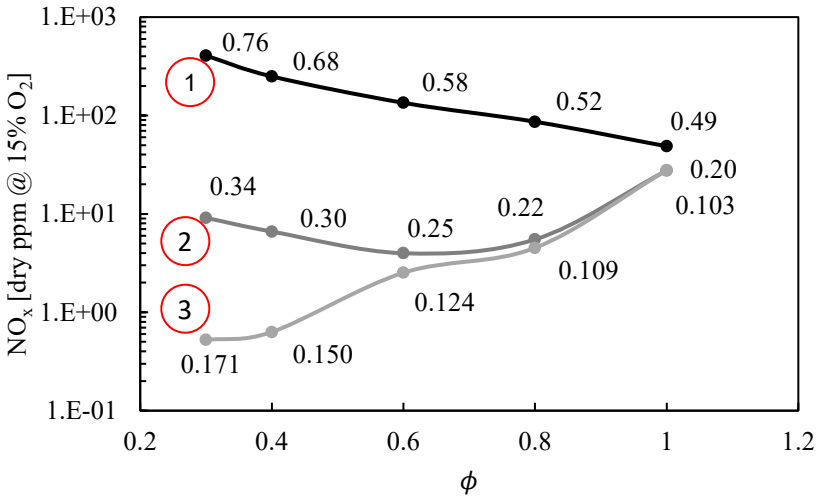

Figure 7.4: NO_x emissions as a function of ϕ for the four-reactor CRN, three different reactor volume settings. Values of residence time shown in seconds for each data-point. T_{in} = 600 K. RR = 0.2.

In a simplified model as the discussed CRN, residence times play an even more important role. The simulations were performed by maintaining the total mass flow constant. However, as the temperature increase is lower for leaner cases, these were characterized by higher residence times due to lower density. The plot in Figure 7.4 shows how the NO_x emissions behave with ϕ for three different volume settings. For residence times varying from 0.49 to 0.76 s across the values of ϕ (case 1 in Figure 7.4), lower ϕ causes higher NO_x. However, when the values vary from 0.103 to 0.171 s (case 3 in Figure 7.4), NO_x increases with ϕ. This can be explained by the presence two effects: i) the increasing NO_x due to longer time available for reactions to proceed and ii) the increasing NO_x due to reactants being exposed to higher temperatures. The

case varying from 0.20 to 0.34 s (case 2) results in a non-monotonic trend, which indicates the shift between these two effects.

The overall NO_x behaviour is complex and is dependent on the temperatures attained in the reactors, residence time, and recirculation ratio. Understanding the complexity and how the parameters involved act aids the analysis of the ITB CRN.

7.3 Effects of Different Chemical Reaction Mechanisms

The results of the analysis documented in Section 6.6 show that the CRN model of the ITB is able to reproduce the experimental results to a good extent and that there are significant differences between the two selected chemical reaction mechanisms (GRI 2.11 and GRI 3.0). The reasons for such differences are not entirely clear, although there is evidence that the prompt NO chemistry was responsible for the deviations.

The development of the ITB concept, and of FC in general, is highly dependent on the computational tools' ability to accurately predict pollutant emissions since the design is aimed at taking advantage of the vitiated oxidiser to reduce emissions. Therefore, assessing and understanding the performance of chemical reaction mechanisms is of great importance. Moreover, the understanding regarding the NO_x emission mechanisms in systems with high recirculation intended to operate under the FC regime is still limited.

In this section, the effects 5 different CH_4 combustion mechanisms are treated: GRI 2.11 [143], GRI 3.0 [37], Konnov [155], GDF-Kin® 3.0 NCN [156] and POLIMI C1C3HT [157]. The GRI mechanisms [37,143] were developed with an aim of representing methane and natural gas flames and their ignition. The GRI 2.11 mechanism inolves 49 species and 277 reactions, the GRI 3.0 53 species and 325 reactions and has been optimized for conditions between 1000 and 2500 K, 1.333·103 to $1.013 \cdot 10^6$ Pa, and equivalence ratios from 0.1 to 5 in premixed systems.

The Konnov mechanism [155] was developed to model the combustion of H_2, CO, CH_2O, CH_3OH, CH_4 and C2-C3 hydrocarbons [158]. The mechanism involves 129 species and 1231 reactions. The original mechanism underwent modifications related to the prompt NO pathway: instead of the HCN route, the NCN route was implemented. The same route is present in the GDF-Kin® 3.0 NCN mechanism [156], as the authors compared the performance of the mechanism with both routes. Intended to simulate natural gas combustion, the mechanism is composed of 119 species and 883 reactions.

Lastly, the POLIMI C1C3HT [157] was developed to simulate the combustion and pyrolysis of hydrocarbons with up to 3 carbon atoms. Its development was mostly based on flame speed data for several species (H_2 and H_2/CO mixtures, small and large hydrocarbons, alcohols and hydrocarbon mixtures). The prompt NO_x HCN route was adopted in this mechanism. The mechanism contains 115 species and 2141 reactions.

In order to quantify the contributions of each formation pathway, the CRN was also run with deactivated reactions. The deactivated reactions for each pathway in each chemical reaction mechanism are listed in Appendix A.

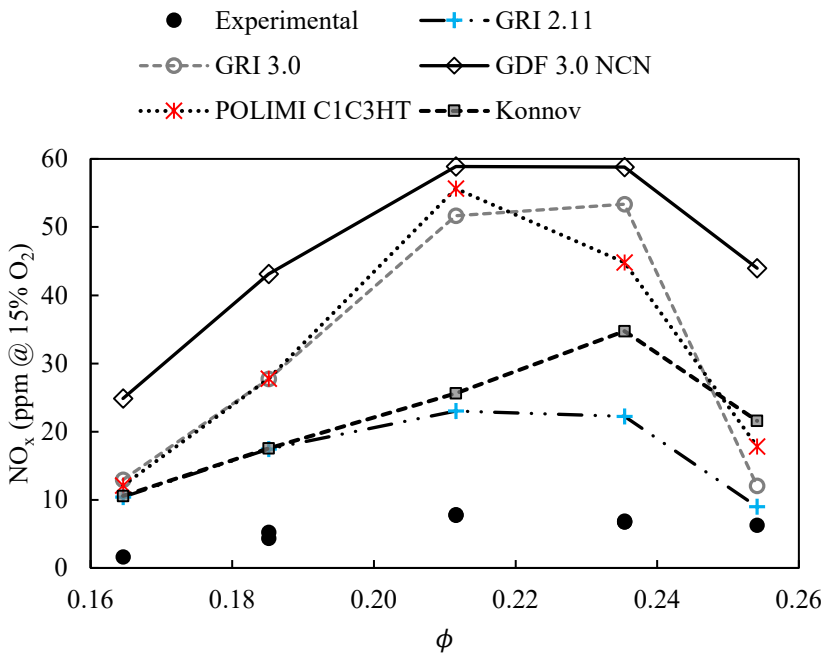

Figure 7.5: NO_x emissions as a function of the global equivalence ratio for various chemical reaction mechanisms.

Comparing the various available chemical reaction mechanisms is important in order to understand as to how they differ in their performance and to check the dependency of the resulting emission trend on the mechanism. The results of Figure 7.5 show that all mechanisms are able to predict the non-monotonic trend while over predicting the emissions of the ITB obtained through the experiments. The reason for the overprediction appears to be the prompt NO_x formation, which plays an important role according to all chemical reaction mechanisms. Apparently, the results are independent of the NCN pathway for prompt formation (instead of HCN), as it is nowadays known to be the way reactions proceed [152]. The POLIMI and both GRI mechanisms (2.11 and 3.0) consider prompt NO_x via the HCN route, while the other two mechanisms employ the NCN route.

Previous studies have shown that the relative importance of the NNH and N_2O-intermediate pathways increases under FC [159]. However, the contribution of prompt NO_x is responsible for the difference between the mechanisms in this case. Table 7.1 shows that the overprediction of NO_x in Figure 7.5 is correlated with the mean contribution of prompt NO_x.

The results suggest that prompt NO_x is systematic overpredicted. It is unclear whether this is universal for every combustion system with recirculation of products. However, further studies should be focused on prompt NO_x chemistry in order to clarify if reaction rates should be lower when vitiated conditions are attained, or if reactions progress through different routes.

Table 7.1: Results for the different chemical reaction mechanisms across the investigated equivalence ratios with respect to prompt NO_x contribution and deviation from experiments.

Mechanism	Prompt NO_x Mean Contribution	Mean Deviation from Experiments
GRI 2.11	43.1 %	1.93
Konnov	45.5 %	2.98
GRI 3.0	67.7 %	4.71
POLIMI C1C3HT	76.3 %	4.76
GDF-Kin® 3.0 NCN	85.0 %	7.30

7.4 Effect of Different Operating Conditions

The investigation of the effect of higher temperatures and pressures on NO_x emissions was conducted using the GRI 2.11 mechanism, due to its better performance when compared to experiments. These conditions were investigated to achieve settings closer to those expected in the dual combustor engine [18].

Increasing temperatures cause the overall contribution of prompt NO_x to decrease, as thermal NO_x tends to increase its contribution (Figure 7.6). Moreover, the role of prompt NO_x in causing the non-monotonic behaviour is no longer important for higher inlet temperatures. Instead, the NNH pathway becomes the most important driver.

The overall trend of NO_x emissions is maintained with increasing temperatures. However, the higher the T_{in}, the leaner is the condition in which NO_x peak occurs. This is partially explained by the effect of residence time, in a similar fashion to what is discussed in Section 2.2. As the power input is maintained for every case, higher T_{in} causes lower residence times due to the decrease in density. This demonstrates that the volume of the ITB (for a given design) can be optimized for a given inlet temperature. In turn, T_{in} is determined by the power setting, the energy fraction between the main combustor and the ITB, and the high-pressure turbine pressure ratio.

For conventional combustors, the scaling of NO_x has been reported to follow the expression of Eq. 7.2. The exponent *n* usually has a value between 0.5 and 0.8 for values closer to stoichiometry [52], while leaner equivalence ratios are not usually affected by *p*, having *n* equal to 0 [53]. For the comparison carried out in Figure 7.7, the value of *n* was assumed to be 0 at the leanest condition and it was increased linearly up to 0.65 for the richest case.

$$NO_x = (p^n)\ NO_x@\ 1\ atm \qquad \text{Eq. 7.2}$$

The effect of pressure on NO_x emissions is more complex than that of temperature, as shown in Figure 7.7. The NO_x emissions on the leaner portion of the investigated ϕ behave similarly to NO_x emissions of conventional combustors: higher pressures increase NO_x emissions as in Eq. 7.2. The increase is caused by the increase in residence times at higher p, similarly to the effect described in Section 2.2. At $\phi \approx 0.21$, NO_x emissions drop below the value attained at 1 bar.

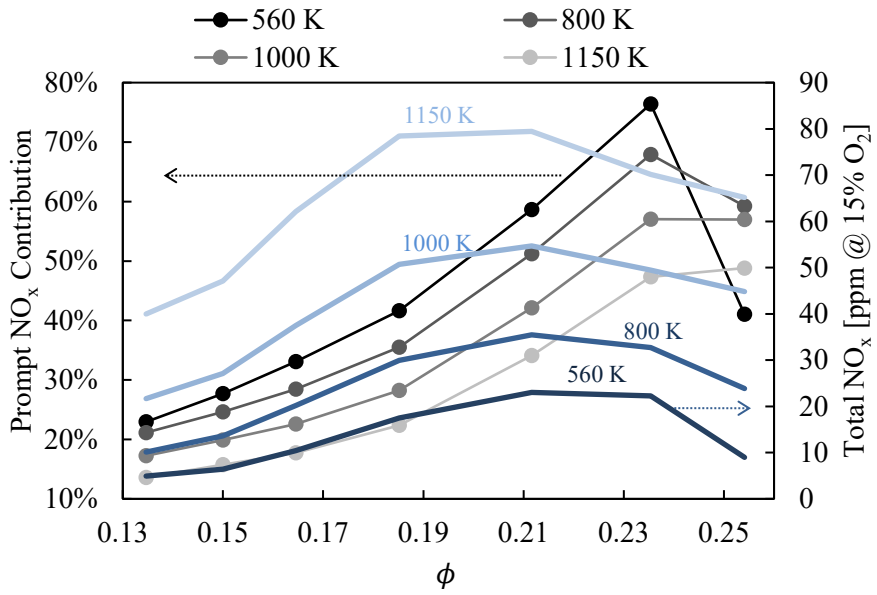

Figure 7.6: Total NO_x emissions and relative prompt NO_x contribution as functions of global equivalence ratio for various T_{in}.

It was shown in Section 6.7 that at this point thermal NO_x starts decreasing (for p = 1 bar), while reburning and prompt increase, with the former becoming dominant along with the NNH pathway. The reduction of the thermal pathway (caused by the favourable conditions for reburning) and the increase in reburning still occurs for higher p. However, the prompt NO_x contribution is lower, a known effect of increasing p [27,53]. Additionally, the NNH pathway has lower NO_x production than it does at p = 1 bar. Subsequently, NO_x emissions increase at the richer condition due to an increase in the thermal and N_2O-intermediate pathways, indicating that the higher temperatures attained at higher ϕ play a more important role for the overall NO_x formation.

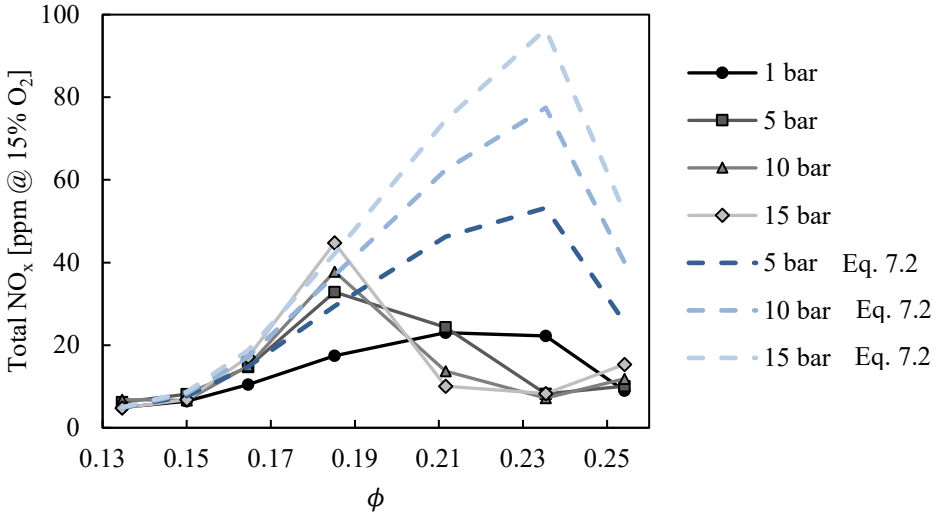

Figure 7.7: NO_x emissions as a function of the global equivalence ratio for various operational pressure values of the ITB CRN. Dashed lines represent the values obtained when considering the correlation of Eq. 7.2.

The results suggest that experimental data on emissions at high pressures for combustors intended to operate in the FC regime are necessary. Given the reported importance of prompt NO_x as a contributor at atmospheric pressures, the design of an ITB may take advantage of its suppression at higher pressures.

7.5 Overall Comments

The non-monotonic NO_x emission curves with lean ϕ shown in Figure 7.1 were explained differently by the authors of those publications. Given the complexity of the phenomena involved, as shown in the current analysis, it may be the case that the results are truly caused by different reasons.

In view of the influence of the residence time displayed in Figure 7.4, the results of Sorrentino et al. [154] may be a consequence of this effect. As temperatures were higher for higher ϕ, residence times tended to be lower due to the reduction in density, justifying the lower NO_x emissions. This effect is not likely to be the most prominent for the cases of Veríssimo et al.[62] and the ITB, since leaner conditions had higher mass flows as fuel input was maintained. A more likely explanation is related to the alteration of prompt NO_x and the effect of RR, similarly to what is shown in Fig. 6. Due to the different mass flows and heat release characteristics, the amount and composition of recirculated gases is different for each ϕ. Nonetheless, it is also important to take local phenomena into account, as changes in mixing patterns and heat losses have the potential to greatly influence the progress of chemistry.

7.6 CONCLUSIONS

The development of new combustion technologies aimed at reducing pollutant emissions is highly dependent on the capability of computational tools to predict emissions. This chapter examines the trends in NO_x emissions of an ITB intended to be operated under the FC regime by analysing the combustion of CH_4. The analysis was performed by means of CRNs, and the effects of different chemical reaction mechanisms, reactants temperature, operating pressure, and recirculation ratio were shown.

The conclusions of the analysis are summarized as follows:

- the overall behaviour of NO_x emissions in systems with high recirculation ratios is complex and is dependent on several factors, chiefly reactants temperature, heat losses, amount of recirculation, and residence time;
- the presence of combustion products and recirculation increase the relative importance of the prompt and NNH pathways, as well as NO reburning. The contribution of thermal NO_x tends to decrease with RR;
- all investigated chemical reaction mechanisms resulted in overprediction of NO_x and in dominance of the prompt pathway. Prompt NO_x contribution was proportional to the overprediction, indicating that the reaction subset and its reaction rates for vitiated conditions may require revisions;
- the role of prompt NO_x was shown to be prominent in the ITB experiments at atmospheric pressure and relatively low reactants temperature;
- increasing reactants temperature in the simulations did not alter the behaviour of NO_x with ϕ. The overall emissions increased with increasing T_{in} and the NO_x peak moved to lower ϕ due to lower residence times in case of higher temperatures;
- the simulations in which the operational pressure was set to a high value put in evidence that higher pressures entail complex effects on the behaviour of emissions with ϕ. Leaner conditions cause a behaviour similar to that of conventional combustors (increase in NO_x). However, NO_x drops with further increase in ϕ due to the suppression of prompt NO_x production and due to the presence of reburning;
- given that all simulations herein presented were performed with CRN models, it is advisable to conduct experiments and simulations taking into account the fluid dynamics and turbulence effects in order to confirm these findings.

The consequences of the results discussed in this paper for the design of an ITB or any design intended to apply FC to aeronautical gas turbines are:

- a successful ITB design should take advantage of the particularities of NO_x formation in lean conditions. Emissions can be optimized by altering residence times, operating pressure, and volume;
- classical correlations for the effect of pressure on the NO_x emissions of gas turbine combustors should not be employed for combustors with high recirculation rates;
- the split of oxidiser between primary and dilution zones has more complex consequences in combustors with high recirculation than in conventional combustors. Besides influencing the amount of recirculation, the split also influences the chemistry of pollutant species;
- the presence of extra degrees of freedom (energy split between primary and secondary combustors, and the design parameters of the ITB), as well as the existence of local minima in the pollutant emissions, makes the design of a dual combustor system challenging but promising.

Chapter 8 Automatic CRN Generation

Following the encouraging results achieved by manually setting up CRN models as shown in Chapters 6 and 7, it was decided to develop a procedure to automatically post-process CFD solutions and generate CRNs associated with them based on user-defined parameters. The main objective of the method is to avoid the lack of repeatability affecting CRNs which are generated manually. A test case related to FC and available in open literature was chosen.

8.1 INTRODUCTION

The lack of detailed chemical schemes has been pointed out as the main cause of discrepancy often seen between CFD-based simulations and reference experimental results when dealing with combustion emissions [104]. Therefore, the use of CRNs to predict pollutant emissions has gained attention because detailed chemical reaction mechanisms can be introduced in the simulations at relatively low computational costs. However, most approaches developed for CRNs neglect turbulence-chemistry interaction and complex flow structures.

The ad hoc design of CRNs has provided valuable results. The developments are usually based on experimental results or CFD simulations. The work of Lebedev et al. [106] presented a CRN composed of six reactors to model a gas turbine combustor. The authors defined the CRN based on the mixture fraction field predicted via CFD. Likewise, utilizing velocity, temperature and species fields coming from CFD simulations, Park et al. [105] developed a CRN to model a lean-premixed gas turbine combustor and obtained good matches with respect to experimental data.

More recently, Prakash et al. [160] studied the effect of exhaust gas recirculation (EGR) on the emissions of a lean premixed gas turbine combustor using a manually designed CRN. The adoption of EGR might cause the required conditions for FC to occur, as O_2 concentrations drop and reactants temperatures rise. The findings of Chapters 6 and 7 are good examples of similar results.

The application of CRNs to predict emissions from FC systems has, in principle, advantages if compared to CRNs modelling conventional combustion systems. The highly distributed reaction zones, as well as lower gradients of species and temperatures, are better represented by ideal reactors [30]. However, this observation is valid for the largest scales, as there is evidence FC might be composed of highly interactive flamelets at the smaller scales [99,100,161].

Contents of this chapter appeared in:

Perpignan AAV, Sampat R, Rao AG. *Modelling pollutant emissions of Flameless Combustion with a joint CFD and Chemical Reactor Network approach*. Frontiers in Mechanical Engineering 2019;5(63):1-19, DOI: 10.3389/fmech.2019.00063.

The manual generation of CRNs is, nonetheless, particularly reliant on the experience of the designer and suffers from the lack of repeatability as a significant amount of trial and error is involved. Additionally, creating networks manually impedes the reproducibility of results and hampers systematic studies. As an attempt to avoid these limitations, strategies to generate CRNs automatically based on CFD solutions have been developed.

Early applications of automatic CRN generation were employed in simulations for analysing furnaces [162-164]. Promising results were achieved by post-processing 3D CFD simulations to generate CRNs. Those authors' works utilized temperature and stoichiometry to define the ideal reactors, which could be PSRs or PFRs, based on the angle of the velocity vector. The underlying assumption was that the simplified chemistry models employed in the CFD were enough to predict temperature, velocity and major species. Moreover, the results documented in these studies provided insights into important variables to be taken into account when clustering CFD cells: temperature, a variable capturing the flow direction, and at least one measure of composition.

The same computational tool (with the same clustering criteria) was employed by Frassoldati et al. [165] in the case of the swirling flame of the TECFLAM burner test case. The authors showed the effect of varying the number of reactors on the result of NO_x emissions. For that specific case, having 300 reactors proved to be enough to guarantee no significant variation with the results obtained with a further increase in the number of reactors. Good agreement with the outlet value of NO_x was shown, however only one operating condition was simulated.

Fichet et al. [166] presented another strategy to use a CFD solution as an input to build a CRN. The authors utilized a gas turbine combustor to showcase the capabilities of the approach. They opted for discarding the temperatures calculated with CFD and recalculated the temperatures based on the heat release of the chemical reactions predicted by the CRN. Though, they did not pursue any systematic study on the advantages and disadvantages of this approach. The authors reported good agreement between measured and simulated NO_x emissions. However, also in this case only one operating condition was available.

Similarly, Monaghan et al. [167] utilized the Sandia Flame D as a test case and post-processed a CFD solution to build CRNs. The authors reported improved results for minor species (OH and NO) with respect to the initial CFD solution. The strategy to cluster CFD computational cells into reactors involved using mixture fraction, temperature and the axial coordinate.

In yet another example, Cuoci et al. [168] utilized a few test cases to assess the capabilities of their computational tool, including the test case utilized in the present work, presented in Section 8.2. The authors analysed one of the operating conditions for which they reported improved NO_x predictions, while CO was overpredicted to some extent. According to the authors, the source of deviation in NO was the incorrect temperatures calculated with the CFD simulations.

Despite these valuable developments, the full potential and limitations of using both CFD and CRN are not fully known. For example, the effect of different clustering criteria on the final solution is not clear, and that is one of the objectives of the study documented in this chapter. Additionally, there are other unknowns in this modelling approach that are worth further investigation, as, for example, the effect of neglecting turbulence chemistry-interaction or, conversely, taking it into account (via a PaSR - Partially Stirred Reactor approach, for example). In addition, the pros and cons of solving the energy equation in the CRN step should also be researched.

For these reasons, Automatic Generation of Networks for Emission Simulation (AGNES) [169] was developed at the Delft University of Technology. The computational tool uses Cantera [36], an open-source program dedicated for chemical kinetics computations. Yousefian et al. [170] reviewed the available hybrid computational tools based on CRNs for emissions predictions. In their evaluation of the different available solvers for CRNs, the authors highlighted two of the characteristics of Cantera which made it attractive for the development of AGNES: the capability of solving the energy equation and the fact that it is a free and open-source solver. Being able to modify and control the code was essential for the development of AGNES.

In this chapter, AGNES is utilized to simulate a test case related to the FC regime, in order to showcase its capabilities, limitations and improvement opportunities. Additionally, the analysis of the results aims to clarify the causes for the emission behaviour associated with the chosen test case. The unique contribution of the research discussed in the following is the assessment of different clustering criteria on the outlet emissions of an FC system involving complex NO_x formation mechanisms with varying equivalence ratio, as described in Section 8.2.

8.2 THE TEST CASE

In order to evaluate the performance of AGNES, a test case was chosen based on the available information and the relevance to FC. Data availability on emission characteristics of the combustor for various operating conditions was a stringent requirement for the selection. For these reasons, the test case described by Veríssimo et al. [62] was chosen as a test case. The combustor was developed to study FC in a non-premixed combustion mode. The combustor consists of a cylindrical combustion chamber with a central air jet surrounded by 16 fuel jets in the burner head. This configuration is a variation of the most common jet-induced recirculation geometry in which a central fuel jet is surrounded by air jets [171]. The inlet air was preheated to 673.15 K, while the fuel (pure methane) was at room temperature.

The equivalence ratio was varied by maintaining the fuel mass flow (energy input as heat of 10 kW) and altering the air mass flow. Data on OH* chemiluminescence, flue-gas temperatures and, more importantly, emissions of CO and NO_x were acquired for all operating conditions. The equivalence ratio was varied from $\phi = 0.455$ to 0.909 and the variation of CO and NO_x emissions with ϕ was found to be non-monotonic.

The authors reported a peak in NO_x at around $\phi = 0.53$, while CO was practically undetectable for the runs at approximately $\phi = 0.53$ and 0.59 (see Figure 8.1).

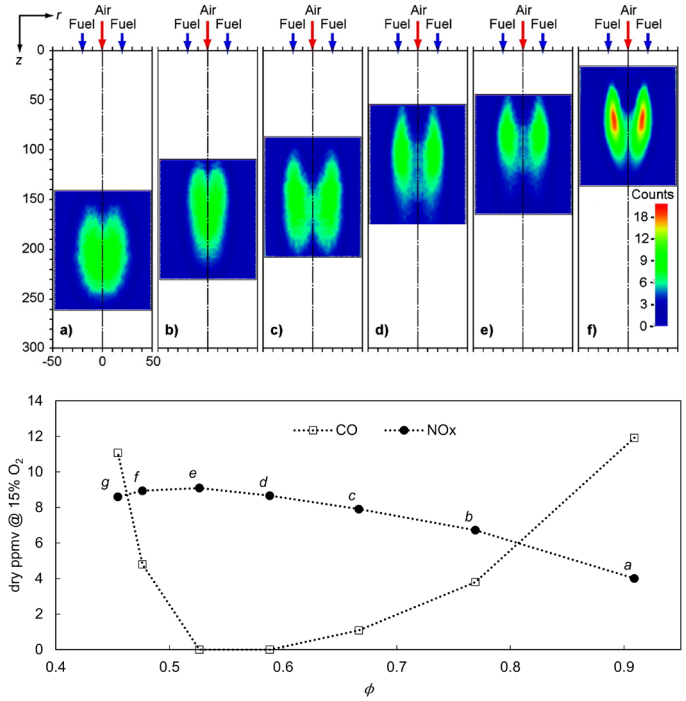

Figure 8.1: Mean OH images for diverse global equivalence ratio values. From left to right, $\phi \cong 0.91, 0.77, 0.67, 0.59, 0.53, 0.48$ (above). Emissions of NO_x and CO in dry volumetric ppm adapted from Veríssimo et al. [62] (below).*

This result was explained by the authors based on a combined effect of the global equivalence ratio and the mixing characteristics of the combustor. Starting from condition *a* in Figure 8.1 and going towards leaner conditions, more air flow was added. The higher central air jet momentum was responsible, according to the authors, for the quicker and stronger entrainment of the fuel, which featured weaker jets with respected to the central air jet. The stronger mixing of fresh reactants caused more intense reaction zones (as shown in Figure 8.1), while not allowing as much mixing of combustion products prior to the reactions. The result was therefore higher NO_x and lower CO emissions. This trend was dominant up to conditions *e* or *f*, in which the usual pattern of lower NO_x and higher CO formation at leaner conditions becomes dominant over the mixing characteristics.

In a more recent study, Zhou et al. [172] performed OH and CH_2O PLIF measurements on the same setup, and referred to operating conditions *a*, *c* and *e* as flameless, transition and conventional modes respectively. They concur with the observation that that the reaction zones generatedted for conditions *e* and *f* behave like

conventional diffusion flames, as mixing with combustion products is apparently minimal and combustion is dictated by the mixing between fuel and air. As mixing with combustion products is allowed by the weaker entrainment of fuel by the air jet, the combustion regime transitions then to FC. A summary of the operating conditions with ϕ, air mass flow rate and outlet O_2 concentration is shown in Table 8.1.

Table 8.1: Operating conditions investigated by Veríssimo et al. [62].

Run	ϕ	$\dot{m}_{\mathrm{air}}$ [kg/s $\cdot 10^{-3}$]	Outlet O_2 [% vol.]
a	0.909	3.950	1.959
b	0.769	4.594	4.356
c	0.667	5.138	6.506
d	0.588	5.804	8.035
e	0.526	6.634	9.425
f	0.476	7.279	10.440
g	0.455	7.522	10.882

For conditions *b* and *d*, Veríssimo et al. [62] provided point-measurements at various radial stations. Temperatures, major species (CO_2 and O_2) and pollutants (CO, UHC and NO_x) were measured at 10 radial positions at each of the 10 stations.

The test case was simulated before, by Cuoci et al. [168] and Lamouroux et al. [173], for example. However, the focus of these previous works was on local values and a single operating condition (Cuoci et al. [168]), and on the effect of including heat losses on local values (Lamouroux et al. [173]). The focus of the present work is instead on the outlet emissions of CO and NO_x across different operating conditions.

8.3 COMPUTATIONAL MODELLING

In an attempt to overcome the challenges in predicting emissions at affordable computational costs, a three-step approach was devised in the research documented here: 1) solution of the flow-field with CFD using simplified chemistry and a turbulence-chemistry interaction model, 2) clustering of computational cells into ideal reactors based on criteria imposed to the CFD solution and 3) solution of the generated CRN with detailed chemical reaction mechanisms. In the following subsections, the details of these steps are presented.

The specific objectives of the performed modelling are:

i. Evaluating the performance of the chosen CFD modelling

ii. Evaluating the performance of the developed computational tool

iii. Comparing the results obtained with CFD and CRNs

iv. Demonstrate whether the minor species prediction is more accurate utilizing the CRN approach than that obtained with the CFD simulations with simplified chemistry

v. Analysing the NO_x formation pathways for different operating conditions of the combustor

8.3.1 COMPUTATIONAL FLUID DYNAMICS

The simulations were performed in order to assess the performance of CFD in predicting pollutant emissions and, more importantly, to generate the inputs for the subsequent modelling steps. The RANS (Reynolds Averaged Navier-Stokes) flow modelling was adopted along with two different turbulence-chemistry interaction models: EDM (Eddy Dissipation Model) [112] and FGM (Flamelet Generated Manifolds) [95], as described in Section 3.3. The EDM was chosen in order to perform a comparison with FGM. The assumption underlying the EDM model is that reactions are chemically fast and are controlled by turbulent mixing. Therefore it was not expected that the EDM would provide accurate results, at least not for all the operating conditions of the chosen test case. The EDM is possibly the simplest turbulence-chemistry interaction model and the objective of utilizing it was to assess how the quality of the CFD simulation utilized as input affects the results obtained by solving the resulting CRNs.

The choice of FGM was based on its relatively low computational cost with respect to other models (Eddy Dissipation Concept, Conditional Source-term Estimation or transported-PDF, for example), and on its good performance for various combustion systems [174,175]. This approach has shown to be promising for the modelling of FC, provided the progress and control variables are adequately chosen. This method allows for the use of detailed chemistry in the pre-calculation generation of flamelets. Non-premixed flamelets were chosen due to the nature of the analysed burner, and were solved using the GRI 3.0 chemical reaction mechanism [37]. Tests were performed utilizing the GRI 2.11 [143] and the POLIMI C1-C3 [157] mechanisms, but no significant differences were observed.

The adopted progress variable as assumed to be dependent on the mass fraction of CO and CO_2. Tests performed including H_2O and H_2 in the definition of the progress variable, species typically adopted, did not provide better results for this case. In order to calculate NO_x species from the CFD simulations to perform a comparison with the results of AGNES, additional transport equations for NO, HCN, N_2O and NH_3 were included. Reactions representing the thermal, prompt and N_2O pathways were considered. Reaction rates of NO_x species accounted for the temperature fluctuations by means of a β-PDF.

The closure of the RANS system of equations was achieved with the k-ε turbulence model. Since the burner features round air and fuel jets, the $C_{\varepsilon 1}$ constant was adjusted

to 1.6 to correct for the well-known round jet anomaly [176,177]. Tests using a Reynolds Stress model did not provide superior results.

The modelling of heat loss is extremely important for the prediction of the temperature and the resulting emissions. The modelling of radiation was performed with the Discrete Ordinates model along with the weighted-sum-of-grey-gases approach to determine the required fluid properties. Heat conduction through the walls was imposed via wall temperature profiles. The profiles were determined partially based on the reported temperature values 5 mm from the walls for conditions *b* and *d*, as well as the outlet temperature. The profiles were first estimated by extrapolating the available experimental data at the radial locations up to the wall location. Subsequently, the resulting profile at the wall was multiplied by a factor to match the outlet temperatures obtained in the experiments, thereby resulting in the same overall heat loss. For conditions in which local measurements were not available, linear interpolations and extrapolations of the profiles were performed, based on the equivalence ratio.

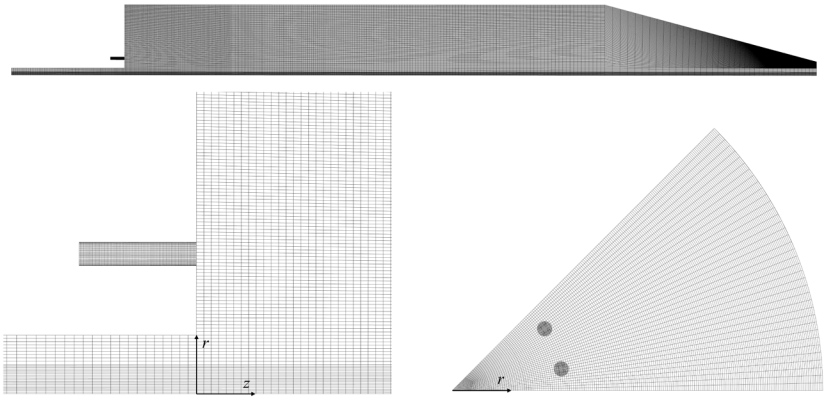

Figure 8.2: Hexahedral mesh employed for CFD simulations.

The computational mesh used was fully hexahedral and a 45° sector was simulated, which included two fuel ports, as shown in Figure 8.2. The 45° angle was selected in order to guarantee a good mesh quality in terms of skewness. The mesh refinement was defined based on monitored outlet values of chemical species, as well as mid-plane averaged quantities, to guarantee no significant changes were attained with further refinement. The initial mesh size was approximately 1 million elements and other four mesh sizes were tested until the difference in outlet species and averaged quantities was negligible. The final mesh was composed of approximately 2.5 million elements.

Periodicity was imposed on the lateral boundaries. The first set of simulations was performed with mass flow inlets of air and fuel with uniform profiles. As the effect of having a developed flow velocity profile imposed as the boundary was shown to

influence the results, this was adopted for the simulations herein reported. The developed flow velocity profile was assumed to follow Eq. 8.1, a power-law velocity profile. The turbulence intensity was assumed to be 5% of the mean velocity. Tests with increased intensity did not significantly affect the results. Turbulence length scale at the boundaries was estimated based on the pipe diameters for both air and fuel, as it was imposed to be 7% of these dimensions. The outlet boundary condition was imposed to have zero static gauge pressure.

$$\frac{w}{w_{max}} = \left(1 - \frac{r}{(D/2)}\right)^{1/7} \quad \text{Eq. 8.1}$$

8.3.2 CHEMICAL REACTOR NETWORKS

Once the results of the CFD simulations have been generated, AGNES first clusters computational cells into reactors based on user-defined criteria. Clustering is executed with a Breadth First Search (BFS) algorithm which traverses the computational domain. Such a domain traversing algorithm was chosen to ensure that the clustered cells are indeed connected to each other in the mesh, forming a continuous domain, and preventing the clustering of discontinuous pockets of cells that satisfy the user-defined criteria. The clustering process proceeds until the total number of reactors (clusters) reaches the set-point imposed by the user, or until the specified maximum tolerance is attained. The range ξ of a given quantity θ is defined as shown in Eq. 8.2, and it is dependent on a certain tolerance μ. The new local value, calculated by averaging the clustered cells, is allowed to deviate from the original local value as expressed by Eq. 8.3. Several variables can be used simultaneously as criteria and every criterion must be satisfied for a cell to be included in a cluster.

$$\xi = \mu(\theta_{max} - \theta_{min}) \quad \text{Eq. 8.2}$$

$$\xi \geq |\theta_{cluster} - \theta_{cell}| \quad \text{Eq. 8.3}$$

The resulting reactors have their properties assigned based on the properties of the CFD cells that compose the reactors. When maintaining the temperatures obtained from the CFD solution, which is the case here, averaged static temperatures are assigned, although total values are used during clustering to guarantee total enthalpy conservation.

The mass flow exchanged between reactors is calculated based on the mass flow between cells in the CFD solution. There is an inherent mass imbalance due to the precision of the CFD solution which needs to be corrected to ensure consistent mass

conservation. This is done by accounting for the mass flow between any two reactors as a fraction of the total outflow from the source reactor and by assembling a system of equations. The boundary conditions of total inflow and outflow are accounted for in the system. The system of equations (mass, species, and energy conservation) is solved for, by assigning a vector of total mass outflow from each reactor and the "corrected" mass flow between reactors is recalculated using this vector and the matrix of outflow mass fractions. The mass exchange between reactors is also stored and maintained when solving the CRN simulation.

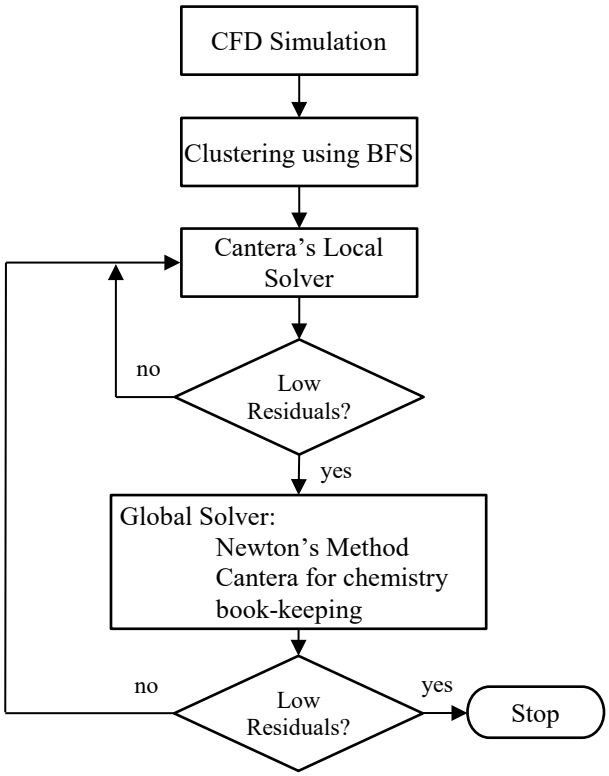

Figure 8.3: Flowchart of the calculation procedure implemented in AGNES.

The system of ODEs is characterized by non-linearity and stiffness. The stiffness of the system is attributed to the wide range of time scales characterizing the involved reactions. Some reactions, such as those responsible for energy release as heat, are much faster than those responsible for the formation of minor species such as NO_x. Therefore, both a local and a global solver are implemented. The local solver treats each reactor individually, whereas the global solver treats all the reactors simultaneously as a system. Cantera is used in the following ways:

i. As a chemistry book keeping tool, in which Cantera ensures a consistent physical and chemical state of the reactors with respect to their temperature, density and species mass fractions and storing the chemical reaction mechanism with all its thermodynamic properties.

ii. It can also be used to solve a reactor network, in which Cantera calls its internal solver to perform the ODE integration of a stiff system of equations while treating it as a dense matrix.

At the local solver level, both features are used, whereas at the global solver level Cantera is used only as a chemistry book keeping tool, as shown in Figure 8.3. This is due to Cantera's solver limitations, as it is unable to simultaneously handle a large number of reactors, hence the governing equations are written explicitly and solved using SciPy, a Python-based ecosystem for mathematics, science, and engineering, to solve a sparse matrix equation for the entire network of reactors.

Both a local and a global solver are employed. Locally, the solver available in Cantera is used to advance each reactor individually, changing its state and that of its connected reservoirs. This solver employs a different time-step for each reactor, based on its residence time. The global solver employs Cantera only to maintain the consistency of the chemical states, while all reactors are solved simultaneously with the sparse solver.

All reactors were considered to be PSRs. No turbulence fluctuation was taken into account in the CRNs. Turbulence fluctuations were neglected because approaches with and without the inclusion of fluctuations are still being successfully employed [170]. Moreover, this first application of AGNES is aimed at investigating the effect of clustering criteria on the solution. The inclusion of fluctuations may be important in some cases, as shown by Cuoci et al. [168]. For this reason AGNES will be modified to be capable of including fluctuations in the future.

The results herein presented were obtained by imposing a 3% tolerance. This resulted in different numbers of reactors for each test condition and imposed clustering criteria. Simulations were performed with both GRI 3.0 and GRI 2.11 mechanisms, to investigate the effect on NO_x formation, as it has been shown that there are relevant differences in the NO_x formation pathways under FC conditions, as shown in Chapters 6 and 7.

Several tests with various clustering criteria were performed in order to evaluate their efficacy in relation to the considered test case [169]. Apart from the obvious choice of temperature as a clustering criterion, it was observed that the inclusion of velocity direction as a clustering criterion was fundamental to capture the recirculation within the combustor, a key for capturing the chemistry within FC. Additionally, a variable acting as a tracer of the fuel, as well as a variable indicating the progress of reactions were required. In the present work, these are the Y_{CH4} and Y_{H2O}, respectively. Two sets of criteria are explored, one with the aforementioned variables, and one with the inclusion of Y_{O2}.

8.4 RESULTS

In this section, the results obtained from CFD simulations are presented and discussed. The extent to which the CFD modelling was able to replicate the experimental data is shown, in terms of temperatures, major species and pollutant emissions. Subsequently, the results obtained with AGNES are thoroughly analysed.

8.4.1 CFD RESULTS

As expected, the FGM simulations achieved better results if compared to the EDM, as shown in Figure 8.4. The temperature rise occurs at a lower z/D if computed with FGM, better representing the experimental data points. Figure 8.4 also evidences the discrepancy between experimental and simulation for z/D = 0.11. This difference might be attributed to the heating of the burner head and its piping, which might have caused the pre-heating of air to a temperature higher than that reported by the authors. Another hypothesis would be the effect of radiation on the thermocouple, although the authors assessed this effect. The error in temperature measurements was estimated by Veríssimo et al. [62] to be around 5% (as is shown by the error bars in Figure 8.4).

Although the centreline values of temperature shown in Figure 8.4 demonstrate that FGM was superior, this superiority is not sufficiently explained by the centreline results. The peak temperatures attained in the combustor are not located on the centreline, but in the region where fuel and air mix. In this region, EDM peak temperatures are much higher than those predicted by FGM, as seen in the contours of Figure 8.4. Additionally, if one observes only the centreline values shown in Figure 8.4 it may seem that reactions calculated with FGM occur faster than those calculated with EDM, but this is not the case.

A major difficulty in simulating the case at hand is the uncertainties related to heat losses. Radiative heat losses play a role in the combustor, as well as conduction through the walls. The total heat loss can be derived by the reported values of outlet temperatures, although the exact location where the temperatures were measured is not fully clear. Therefore, a wall temperature profile was imposed based on the results available at 5 mm from the wall (r/D = 0.45), in the attempt of maintaining the values as close as possible to the experimental results. The temperature at this position is, however, not only dependent on the wall temperatures, but also on the reaction rates, recirculation, and radiation. The extent to which the simulations are able to reproduce these values is shown in Figure 8.5.

The centreline values of O_2 and CO_2 shown in Figure 8.6 indicate that predictions for condition *d* were more accurate than those for the condition *b*. The reasons for this result may be related to the fact that condition *d* is, according to Veríssimo et al. [62] and Zhou et al. [172], closer to the condition typical of conventional diffusion flame, while condition *b* would be more representative of FC, making it more difficult to model, as a control variable representing vitiated recirculated gases may be required for the representation of FC with FGM [178]. However, the values of CO_2 and O_2 close to the outlet should not be dependent on the combustion regime or the type of

modelling. As also shown in Figure 8.6, simulations for condition *b* feature higher CO_2 and lower O_2 values at the outlet. The discrepancy between simulations and experimental O_2 values close to the outlet for condition *b* has been shown before in the results of Cuoci et al. [168]. The experimental uncertainty of 10% in the composition data does not justify the difference alone. Therefore, the uncertainty of the reported mass flows is probably causing the discrepancies.

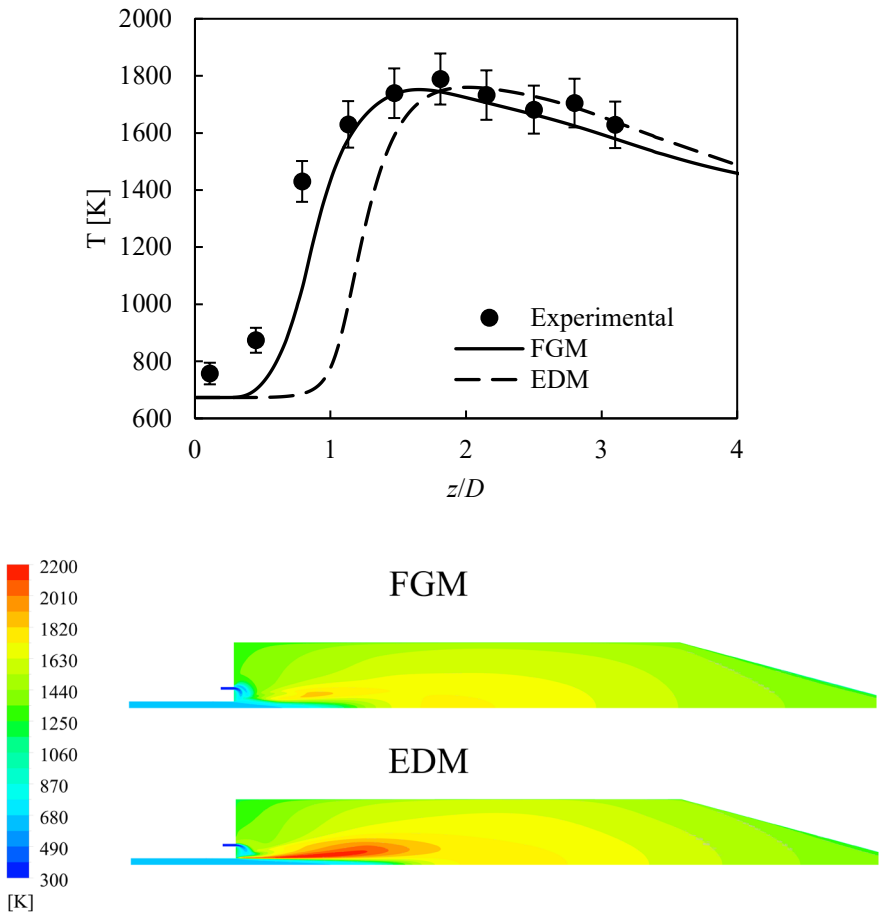

Figure 8.4: Experimental and CFD temperature results along the centreline of the combustor (above) and temperature contour plots (below) for condition b ($\phi \cong 0.77$) using FGM and EDM. Error bars represent experimental uncertainty.

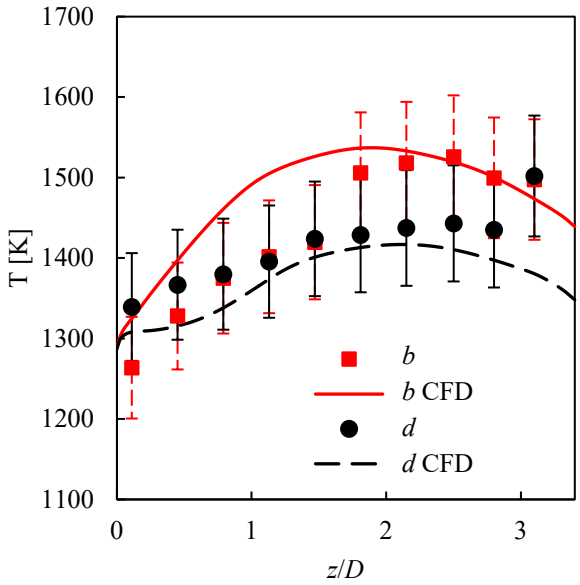

Figure 8.5: Experimental and CFD temperature results along the axial line where r = 45 mm for conditions b (ϕ≅0.77) and d (ϕ≅0.59). Error bars represent experimental uncertainty.

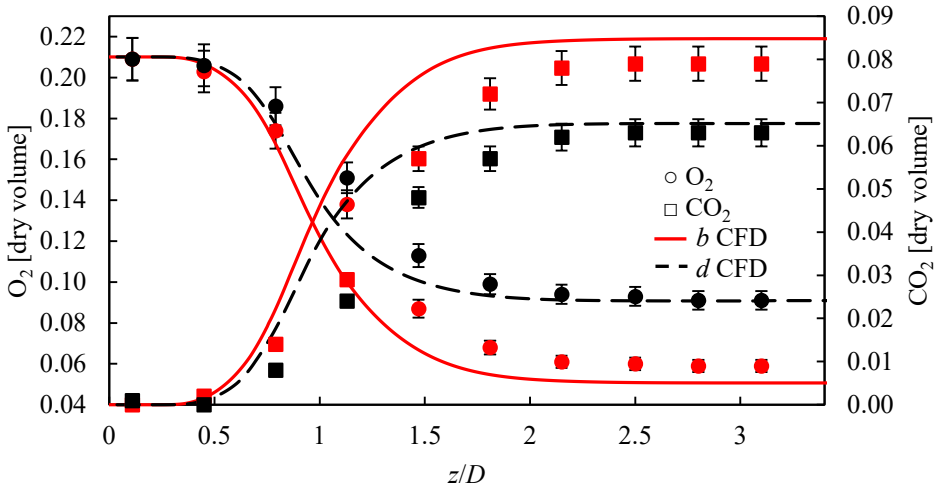

Figure 8.6: Experimental and CFD results along the centreline of the combustor for O_2 and CO_2 concentrations for conditions b (ϕ≅0.77) and d (ϕ≅0.59). Error bars represent experimental uncertainty.

The overall agreement between experimental data and the FGM simulations is good (Figures 8.7 and 8.8). The largest deviations for temperatures occur closer to the burner head (z/D = 0.11), especially for condition *b*. Further downstream in the combustion chamber, the agreement is better. Simulations presented the overall characteristic of retaining lower temperatures near the centreline for longer axial distances, while combustion reactions were further developed (i.e. lower O_2 and higher CO_2 concentrations). This can be explained by a possible imperfect prediction of the mixing between burnt gases and reactants, as well as the effect that burnt gases have on the incoming reactants. Moreover, the aforementioned apparent inconsistency in temperature modelling (or measurements) close to the burner head, as well as the uncertainty related to mass flows might also have contributed to the discrepancy.

The radial profiles (Figures 8.7 and 8.8) show that the effects of the central jet spreading rate seem to be overpredicted by the simulations. This is evidenced by the fact that the gradients of the profiles tend to be lower than those obtained in the experiments for intermediate axial positions (z/D = 1.13 and 1.81). This was also the case in the reported previous computational works related to the same test case [168,173]. However, the discrepancies could also be a result of poor prediction of reaction rates or heat transfer, instead of an artefact of the jet spreading prediction.

The estimations of pollutant emissions from the CFD modelling are poor, both in terms of the absolute values as well as in terms of trends (Figure 8.9). The emission of CO is highly overpredicted, in some conditions up to two orders of magnitude. The NO prediction is, on the other hand, underpredicted. The trend of NO is also not captured, as values increase monotonically with increasing ϕ. These results were to a certain extent expected, as the accurate prediction of CO with FGM is challenging [179] and the NO_x species modelling was not based on a detailed chemical reaction mechanism.

Finally, the CFD results based on FGM were in reasonable agreement with experiments in order to be used as an input to the CRN simulations. Most of the variables are computed with good level of agreement (apart from pollutants). Better results could be expected by utilizing an FGM approach that is more suitable for modelling FC, such as the diluted-FGM, developed by Huang et al. [178]. Perhaps the mixing in the combustor has strong unsteady characteristics which can be captured adequately only by LES. However, previous attempts of simulating the test case with LES along with tabulated chemistry did not provide improved results [173].

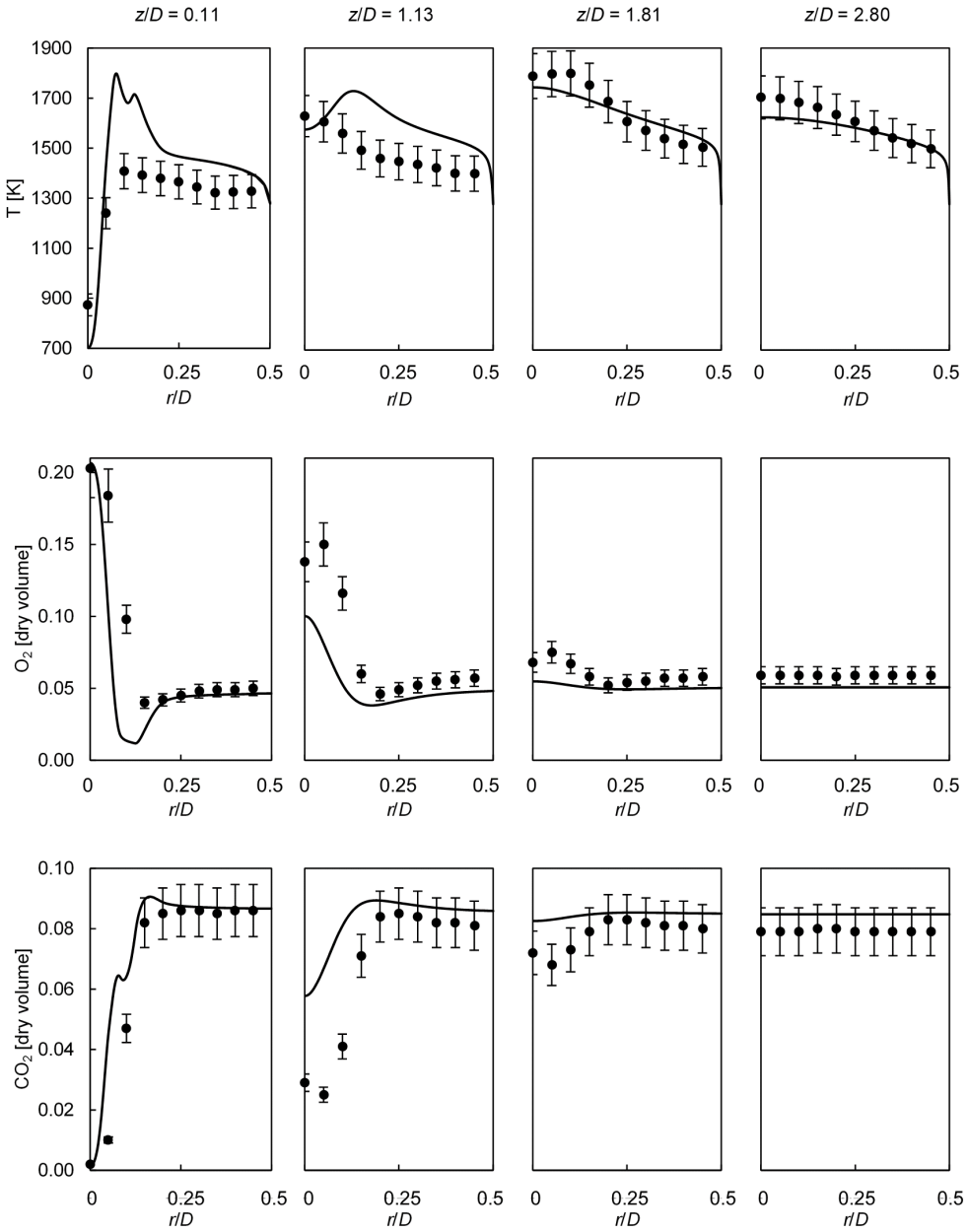

Figure 8.7: Comparisons of experimental and CFD (FGM) parameters: temperature, O_2 concentration, and CO_2 concentration results along radial lines for condition b ($\phi \cong 0.77$). Error bars represent experimental uncertainty.

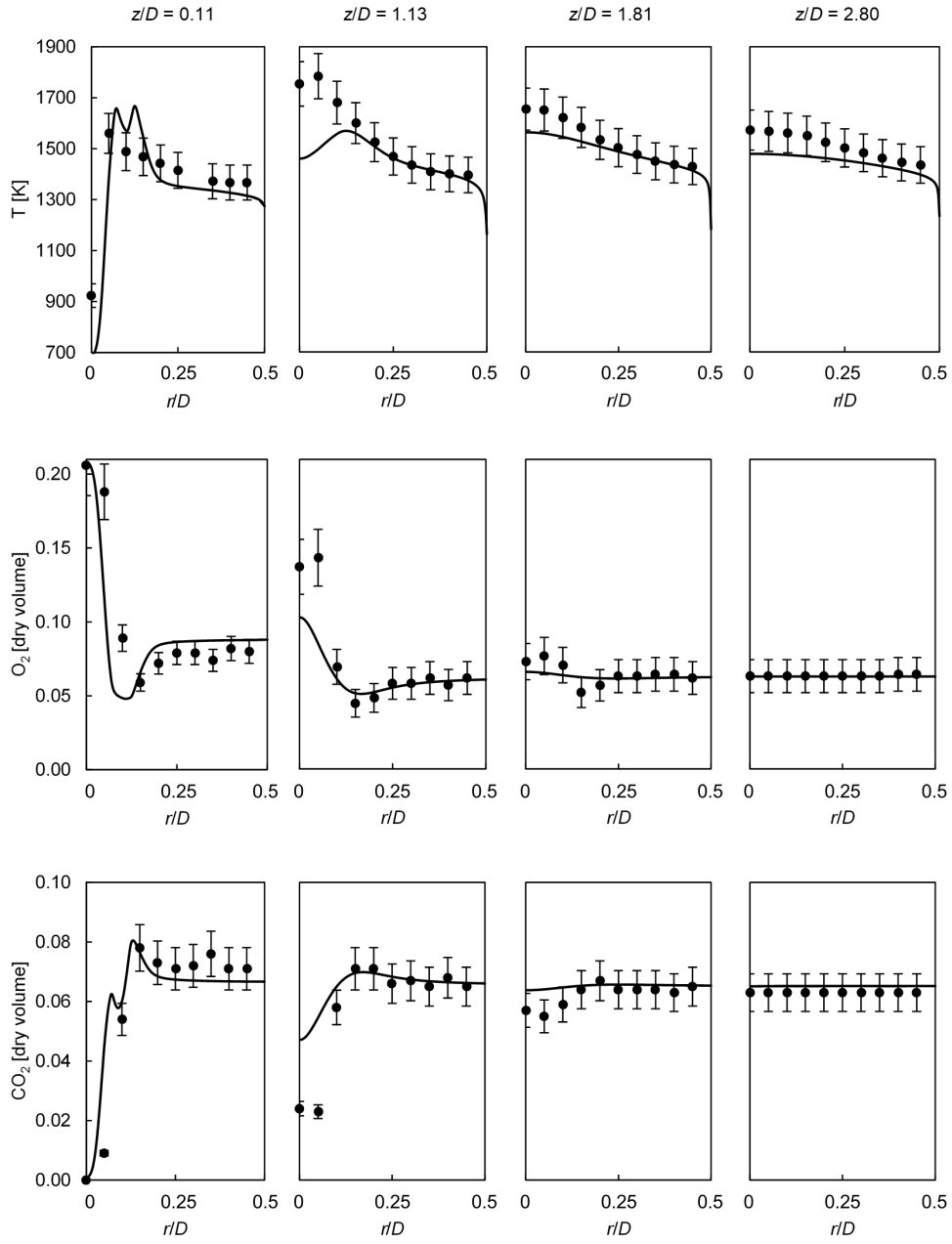

Figure 8.8: Comparisons of experimental and CFD (FGM) parameters: temperature, O_2 concentration, and CO_2 concentration results along radial lines for condition d ($\phi \cong 0.59$). Error bars represent experimental uncertainty.

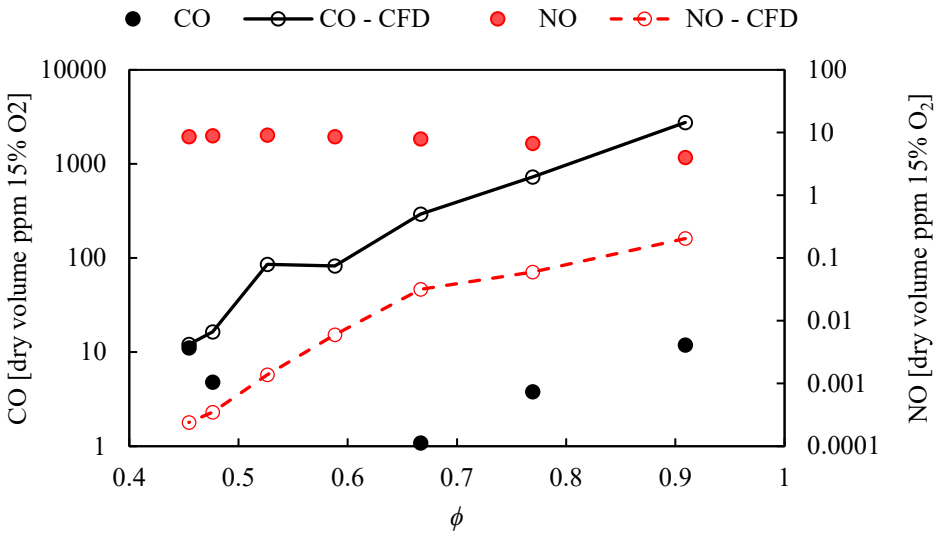

Figure 8.9: Outlet CO and NO results from CFD performed with FGM compared with experimental values. CO values come from tabulated FGM calculations. NO values come from the transported NO calculation.

8.4.2 AGNES Results

The results obtained from the CRN simulations performed with AGNES are discussed herein with respect to the combustion model obtained from the CFD simulation results (FGM or EDM), and also with respect to the clustering criteria, and chemical reaction mechanism.

The CO predictions are improved significantly with respect to the CFD simulations performed with FGM, regardless of the clustering criteria (Figure 8.10). The same is valid for simulations based on the EDM, in which the main difference with respect to FGM is in the predictions of CO for conditions closer to stoichiometry. All results predict the trend of CO and have fairly similar values with respect to the experimental data. Additionally, no significant difference between results calculated with GRI 3.0 and GRI 2.11 can be noticed.

The calculated NO_x values based on the EDM simulations are overpredicted, as expected (Figure 8.11). The high peak temperatures attained with the modelling are responsible for the results being up to one order of magnitude higher. The results obtained from FGM are more complex to analyse (Figure 8.12). When temperature, velocity direction, Y_{CH4} and Y_{H2O} are employed as clustering criteria, the NO_x trend obtained with GRI 2.11 reaction mechanism is monotonic and its slope is the opposite of that of the experimental data: condition *a* had the highest NO_x value. For GRI 3.0, overall values are higher than those calculated with GRI 2.11 (a behaviour previously reported in Chapter 6), but condition *a* features a lower NO_x value than condition *b*,

making the overall trend non-monotonic. The values, however, are not in good agreement with experiments for both chemical reaction mechanism.

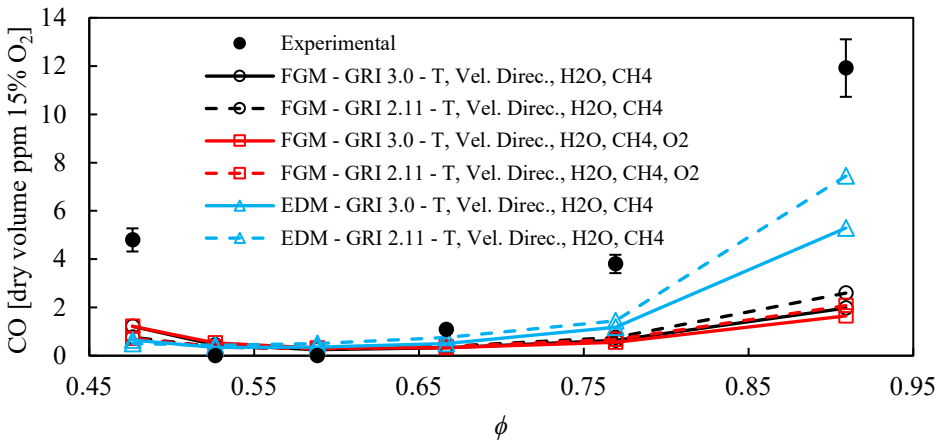

Figure 8.10: Outlet CO results from AGNES compared with experimental results. Different input simulations for AGNES (FGM or EDM) and post-processing options (GRI 3.0 or GRI 2.11, as well as clustering criteria). Error bars represent experimental uncertainty.

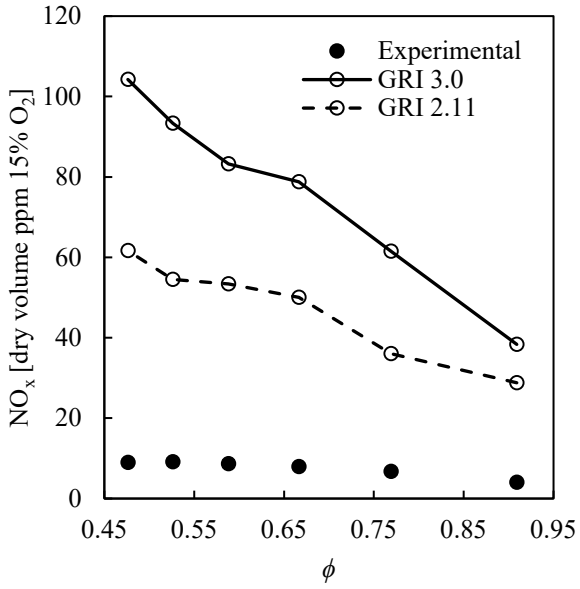

Figure 8.11: Outlet NO_x results from AGNES having CFD simulations performed with EDM as input compared with experimental results.

The inclusion of Y_{O2} as a clustering criterion is fundamental to attain a trend closer to experimental data with respect to the non-monotonic behaviour of the emissions. The results obtained with GRI 2.11 feature values of the same order of magnitude as that of the experimental values (below 10 ppm). Such difference highlights that the choice of clustering criteria has an effect on the accuracy of the solution. The computational time can also be affected by the choice of criteria, as the required number of reactors changes. Additionally, the variables ultimately available from the CFD input can potentially influence the choice for a given CFD modelling approach, provided it has advantageous variables to be employed as clustering criteria. The comparison between the clusters in each of the two criteria sets for condition *b* is shown in Figure 8.13. Differences can be spotted at the region close to the jets, in which recirculation occurs. The addition of Y_{O2} causes this area to have more reactors.

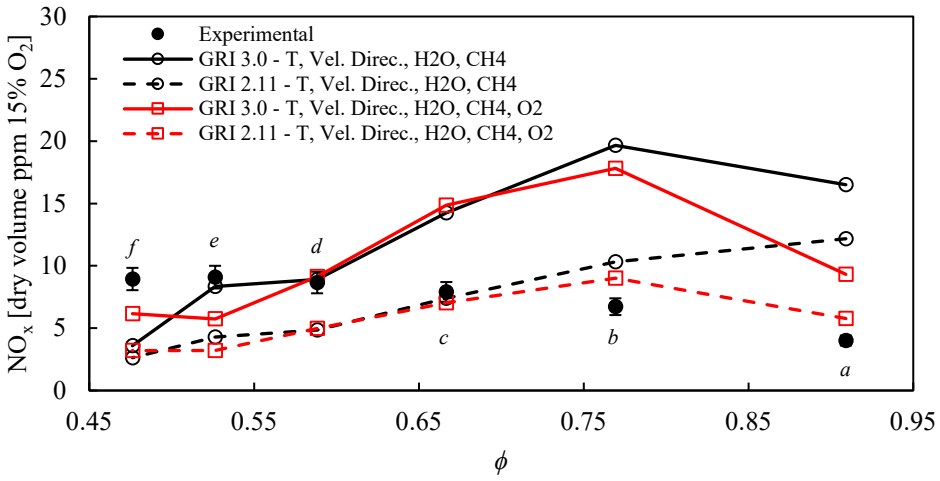

Figure 8.12: Outlet NO_x results from AGNES having CFD simulations performed with FGM as input compared with experimental results. Two different clustering criteria sets. Error bars represent experimental uncertainty.

One should bear in mind that all experimental values were below 10 ppm, and such low values pose a significant challenge for computational simulations. The improvement with respect to the values predicted directly via CFD is remarkable, it can be argued that AGNES is a suitable tool for design of FC combustors. The peak of NO_x emissions is, however, not correctly predicted by any simulation method. While experiments reported the highest values of NO_x for condition *e*, simulations estimate the maximum values for condition *b*. The best match between experimental and simulation NO_x values for condition *b* are for the case of GRI 2.11 that included Y_{O2} as a clustering criterion.

The analysis of local NO_x values for condition *b* presented in Figure 8.14 shows that there are significant discrepancies. Similarly to the results obtained with CFD (Figure 8.7), the radial profiles display larger differences between central ($r/D \sim 0$) and peripheral ($r/D \sim 0.5$) locations than the experimental profiles for locations close to the burner head. Further downstream ($z/D = 1.81$ and 2.80), the opposite is true, as computations predict flatter profiles than what is observed in experiments. On the other hand, the centreline profile shows that the results are satisfactory and certainly represent an improvement with respect to the original CFD calculations. The overprediction of temperatures in locations close to the burner head (as shown in Figure 8.7) also plays a role, as NO_x values are increased at $z/D = 0.11$. The fact that NO_x formation takes place in a relatively short axial region (around $z/D = 1.13$) and then NO_x concentration stays relatively constant is remarkable, as seen in both simulations and experiments.

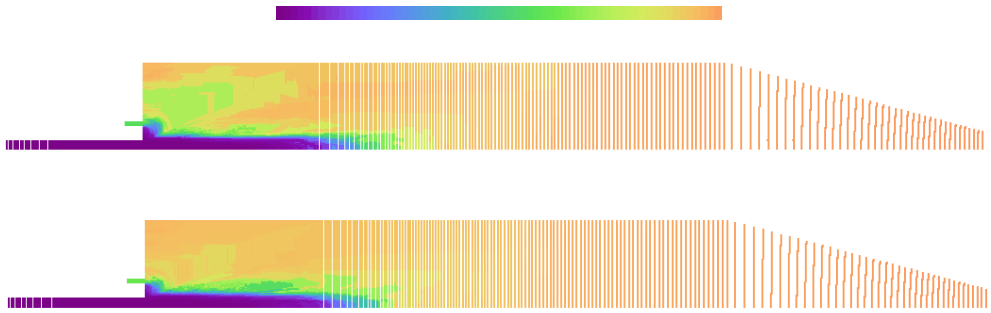

Figure 8.13: Reactors on a plane of the combustor for condition b ($\phi \cong 0.77$). Reactors clustered utilizing T, velocity direction, H_2O and CH_4 (above), and T, velocity direction, H_2O, CH_4 and O_2 (below). Each PSR is represented by a dot located at its centre. The colour scale is arbitrary and was generated based on reactor numbers attributed during the clustering.

Additionally, some features should be further investigated. The fact that the GRI 2.11 can lead to more accurate results raises doubts regarding the prompt NO_x formation, as discussed in Chapter 7. The GRI 2.11 mechanism is supposedly inferior to its successor, GRI 3.0, but the apparent better estimation of the prompt NO_x pathway might be related to different reaction rates in vitiated environments. The chemistry of NO_x formation was shown to be different in previous literature, not only because of thermal NO_x abatement [147,180].

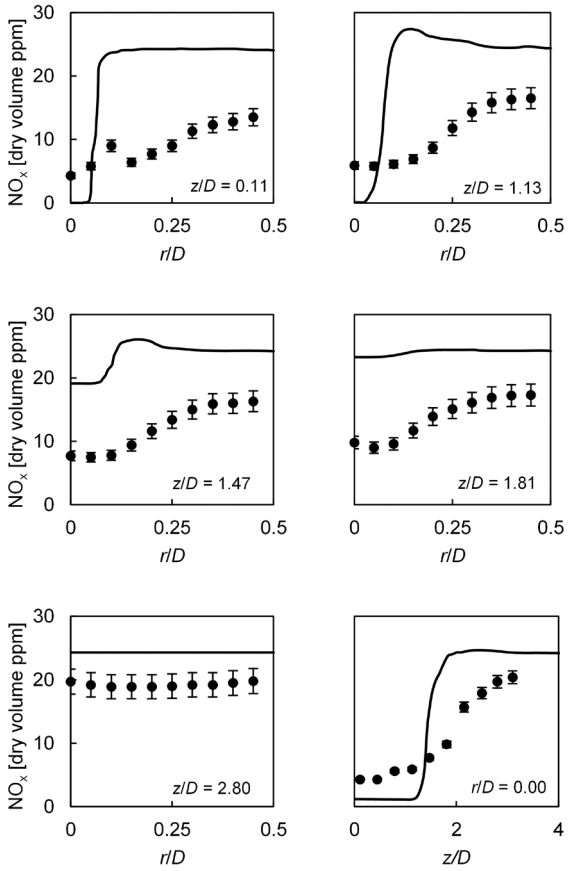

Figure 8.14: NO_x values at selected local profiles. Comparison between experimental data and AGNES results obtained using an FGM simulation as input, GRI 2.11 and T, velocity direction, Y_{H2O}, Y_{CH4}, and Y_{O2} as clustering criteria for condition b ($\phi \cong 0.77$). Error bars represent experimental uncertainty.

In order to understand what causes the non-monotonic behaviour of NO_x, the rates of formation by each pathway were estimated. The rates of the reactions responsible for NO formation at the end of each pathway were taken into account. It is important to highlight that the pathways are not independent and interact with each other. Therefore, isolating their respective contributions is not entirely possible. Nonetheless, the analysis herein performed serves as an indication. The largest source of uncertainty is related to the thermal and prompt pathways. The N atoms that are products along the prompt pathway tend to react via the second reaction of the Zel'dovich pathway [52]. Therefore, the NO formation coming from the second and third reactions of the Zel'dovich pathway was neglected. The thermal NO contribution is considered to be that of the first equation, which is the rate limiting step of the pathway [152].

As far as the prompt pathway is concerned, the GRI 2.11 mechanism considers the route to follow the HCN → CN → NCO → NO pathway, which was for long believed to be pathway through which the reactions progressed [52]. Currently, it is known that the NCN route is active instead [152]. In the present analysis, the prompt pathway is considered as it was in the development of GRI 2.11. Therefore, the NO forming reactions shown in Eqs. 8.4 to 8.8 were taken into account to calculate the NO formation rate.

$$NCO + O \leftrightarrow NO + CO \quad \text{Eq. 8.4}$$

$$NCO + OH \leftrightarrow NO + H + CO \quad \text{Eq. 8.5}$$

$$NCO + O_2 \leftrightarrow NO + CO_2 \quad \text{Eq. 8.6}$$

$$CH + NO \leftrightarrow HCN + O \quad \text{Eq. 8.7}$$

$$CH + NO \leftrightarrow H + NCO \quad \text{Eq. 8.8}$$

The contribution of the N_2O pathway was calculated by the NO formation rates of Eqs. 8.9 to 8.11. It is clear that the N_2O pathway interacts with the prompt pathway via the formation of NCO as shown in Eq. 8.10. That interaction, however, does not directly interfere with the calculation of the NO formation rate by each pathway, as N_2O and NCO are on opposite sides of the reaction.

$$N_2O + O \leftrightarrow 2NO \quad \text{Eq. 8.9}$$

$$NCO + NO \leftrightarrow N_2O + CO \quad \text{Eq. 8.10}$$

$$NH + NO \leftrightarrow N_2O + H \quad \text{Eq. 8.11}$$

Finally, the NNH pathway was taken into account by means of the only reaction forming NO in the pathway present in the GRI 2.11 mechanism (Eq. 8.12).

$$NNH + O \leftrightarrow NH + NO \quad \text{Eq. 8.12}$$

In Figure 8.15, a comparison between the NO formation rates for conditions *a*, *b* and *e* is displayed for the case with GRI 2.11 and Y_{O2} included as a clustering criterion. The figure displays the results along an axial line at the radial position *r* = 15 mm. This position was found to feature the highest rates of formation and, therefore, it was selected. Several conclusions can be drawn from this analysis. The first important fact is that thermal NO decreases as ϕ is reduced (going from condition *a* to *f*). In fact, the rates of thermal NO reduces as much as 3 orders of magnitude, showing that the contribution of thermal NO cannot explain the overall trend.

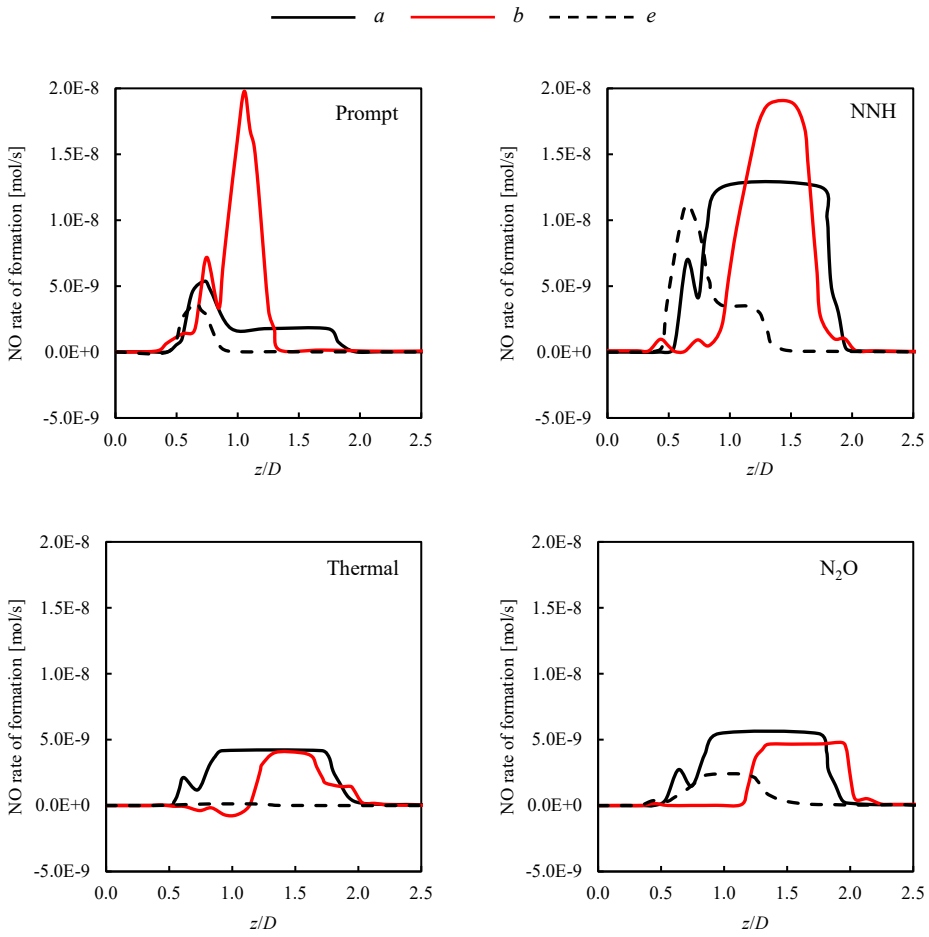

Figure 8.15: NO formation rates at r = 15 mm along the axial direction for the different formation pathways. Values presented for conditions a ($\phi \cong 0.91$), b ($\phi \cong 0.77$), and e ($\phi \cong 0.53$).

Secondly, the role of the prompt pathway is shown to be important. The rates of NO production by prompt are the highest for condition *b*, which explains why this condition has the highest total value of NO_x. Possibly, this peak was predicted for

condition *b* in the simulations while it occurs for condition *e* according to the experimental data. The prompt pathway was shown to be responsible for the peak in NO at lean values for systems operating under FC or with high recirculation, see Chapters 6 and 7.

Thirdly, the role of the NNH pathway is also prominent. The peak value of NO formation via the NNH pathway is higher at condition *b* than at condition *a*. It should be noted that reactions tend to occur further downstream for condition *b* if compared to the other two conditions. This is an indication of how important the predictions of jet development, recirculation and entrainment coming from the CFD solutions are, since NO formation via pathways other than thermal is dependent on slight variations in composition.

8.5 Conclusions & Recommendations

The work presented in this chapter is related to CFD and CRN simulations of a test case combustor developed to investigate FC. The FGM model and the EDM were employed in RANS CFD simulations for predicting several operating conditions of the combustor. The CFD results were post-processed and CRNs were automatically generated via clustering of the mesh cells and solved with AGNES.

The following conclusions can be drawn from the study:

- The RANS CFD simulations performed with FGM are able to reproduce experimental data with sufficient accuracy. The main differences with respect to experimental results were found for the main variables near the burner head region.
- CFD simulations performed slightly better for the conditions in which a conventional combustion regime was attained (*d*) if compared to the conditions leading to FC (*b*).
- The CO emission predictions resulting from simulations performed with AGNES are in fairly good agreement with measured values. The proposed approach allows to obtain good CO estimations even when AGNES is associated with CFD simulations relying on the EDM, which is computationally cheap and robust.
- The use of the AGNES software framework significantly improved the NO_x predictions if compared to the considered CFD methods, and a reasonable agreement with experimental results was achieved.
- Simulations showed that, remarkably, the NO_x is formed in a relatively narrow region (from z/D = 1.5 to 2.0, approximately).
- The variables chosen for the formulation of clustering criteria proved to have a significant influence on the obtained results. For a given case, a certain set of criteria could prove to be necessary or optimal with respect to the number

of reactors. To the best of the author's knowledge, this finding has not been previously presented in the literature.

- NO formation in the combustor seems to be dictated by the prompt and NNH pathways. The variation of prompt NO_x is responsible for the non-monotonic variation of NO_x with ϕ.

Further investigations should be carried out to improve or clarify the following issues:

- The proposed method should be explored further in order to optimize the clustering criteria.
- The estimation of outlet emissions for the selected case may require the use of a CFD model able to reasonably model both the FC regime as well as a conventional combustion regime, as different operating conditions result in different combustion regimes.
- The validation and subsequent use of chemical reaction mechanisms for highly vitiated conditions would probably improve the performance of AGNES.
- The assessment of the effect of modelling turbulent fluctuations on the CRN results should be performed in the future. This can be done by clustering the computational cells based on fluctuation values and/or by employing a Partially Stirred Reactor approach.
- The prompt pathway in the FC regime, thus with highly vitiated environments, should be investigated due to its key role.

Chapter 9 Conclusions and Recommendations

This chapter summarizes the most important conclusions that can be drawn based on the results documented in this PhD dissertation. More importantly, recommendations for future investigations are presented in order to facilitate more work building upon the research conducted so far.

9.1 CONCLUSIONS

Combustors operating under the FC regime could solve the problem of the increase in NO_x emissions with the increasing operating pressures and temperatures which benefit the efficiency of turbines. An important part of the work documented here involved the understanding of the current state of the science regarding the FC regime and its development for gas turbines. In this regard the most important conclusions are that

- the existing definitions of FC are not representative of the physics of the regime. The utilization of global parameters to define FC is problematic because the occurrence of the regime depends on local conditions;
- previous attempts to design gas turbine combustors operating under FC relied on the recirculation of combustion products. Recirculation is attained by jet entrainment, a large recirculation zone, or a combination of both. When utilizing jet entrainment, recirculation is directly proportional to the jets momenta, which causes the operating range of the combustor to be limited for practical applications;
- many of the design attempts so far have resulted in low combustion efficiency (high CO emissions), higher pressure losses, narrow operational range, higher complexity, or unfeasibility of integration in the engine.

The conclusions with respect to the utilization of the CFD-CRN approach for emission modelling can be summarized as:

- the CRN models improved the predictions of emissions as compared to those from CFD;
- the CRN calculations performed to model the ITB emissions were able to estimate the trends in NO_x emissions to a reasonable extent, which is valuable in the design process.. However, absolute values were overestimated;
- the predictions of of CO emission from manual CRNs, as well as with AGNES are in fairly good agreement. The emission trends were captured and deviations were below 20% for the ITB. The proposed modelling CFD-CRN method allows to obtain sufficiently accurate estimations of CO emissions even with a computationally cheap and robust CFD method as the EDM;
- the accuracy of NO_x predictions was improved with the use of AGNES (when compared to the CFD calculations), and a reasonable agreement with

experimental results was achieved for the chosen test case, with NO_x values in the same order of magnitude as the experimental data;

- the choice of variables for clustering the CFD computational cells into CRN reactors has a large influence on the results;
- the clustering criteria should be customised for every case in order to capture the physics as closely as possible.

With respect to the NO_x formation in the ITB and in systems with high recirculation, the following concluding remarks hold:

- the presence of combustion products and recirculation increase the relative importance of the prompt and NNH pathways, as well as that of NO reburning. The contribution of thermal NO_x tends to decrease with an increase in the recirculation ratio;
- the emissions from the ITB are primarily determined by the prompt NO_x pathway. The thermal pathway provides a relatively low contribution to the overall NO_x formation, being less important than the NNH and N_2O-intermediate pathways;
- all investigated chemical reaction mechanisms showed the dominance of the prompt NO mechanism. Additionally, the overprediction with respect to experiments was shown to be proportional to the prompt NO contribution, suggesting that studies on prompt NO reaction rates in highly vitiated environments are required;
- increasing reactants temperature did not alter the trend of NO_x with respect to ϕ. The overall emissions increased with increasing T_{in} and the NO_x peak moved to lower ϕ due to lower residence times for higher temperatures;
- the increase in operational pressure causes complex effects on the variation of emissions with ϕ. At the leaner investigated conditions, the emissions had a trend similar to that of conventional combustors (increase in NO_x). However, NO_x dropped with further increase in ϕ, due to the suppression of prompt NO_x production and due to the presence of reburning.

With respect to the ITB simulations, performance and design, the following can be deduced:

- higher levels of oxidiser dilution with N_2 lead to a transition to FC, as evidenced by the low Da in the simulations and by the spreading of the reaction zone observed during the experiments;
- both CFD simulations and experiments point to the occurrence of reactions close the combustor walls and not within the large recirculation zone, as envisioned by the conceptual design. Modifications in fuel injection position and direction, as well as air split, should be considered to improve the ITB design;

- classical correlations for the prediction of the effect of pressure on NO_x emissions from gas turbine combustors should not be employed for combustors with high recirculation rates;
- the presence of extra degrees of freedom (energy split between primary and secondary combustors, and the design parameters of the ITB), as well as the existence of local minima in the pollutant emissions, makes the design of a dual combustor system challenging, but promising.

With respect to the evolution of minor pollutant species in the HPT, it can be concluded that

- chemical species seem to undergo relevant variations through the turbine, as much as a two-fold increase in the initial amount of NO and CO or an 80% decrease in CO. The predicted variation in the pollutant species was, therefore, high. The predicted amount and trend of these variations are dependent on the operating conditions, the composition at the turbine inlet, and the modelling approach;
- the inclusion of turbulence-chemistry interaction in the simulations is necessary. The EDC model predicts lower reaction rates if compared to the FRC without turbulence-chemistry interaction;
- the adopted model of blade wall cooling has shown to have a minor impact on the evolution of CO and NO_x. Variations are related to the fact that the increase in the reaction rate occurs along the blades boundary layers and trailing edge wakes;
- the progression of CO along the turbine stator depends on the initial temperatures as well as the local maxima attained. The dissociation of CO_2 may occur if temperature maxima are high enough and operating pressures are not too high, causing an increase in CO;
- the changes in species concentration along the HPT poses more consequences to the design of a dual combustor configuration than it does to the design of conventional configurations, as the chemistry in the ITB depends on the inlet conditions.

9.2 RECOMMENDATIONS

Regarding the current state of development of FC for GT, as well as the state of knowledge about FC in general, it is recommended to

- establish a new and widely accepted definition of FC to correctly evaluate experiments performed in the past, to establish combustor design requirements, and to guide modelling. The evaluation of local Da and Ka should be performed, as the FC regime is dependent on these variables;

- perform experiments at high pressures, featuring local measurements of CO and NO_x species, and to use advanced diagnostic techniques in order to increase our understanding and allow for better model validation;
- explore innovative engine architecture, as it may pave the ground to the successful attainment of FC in gas turbines. The dual combustor configuration is an example.

Recommendations about the design of an ITB are as follows:

- the presented ITB design may be improved by assuring that the reactions take place in the main recirculation zone and that the dilution oxidiser stream is well-mixed before leaving the combustor;
- a successful ITB design should take advantage of the particularities of NO_x formation in lean conditions. The reduction of emissions can be optimized by altering residence times, operating pressure, and volume;
- the experimental data utilized as a reference to the computational modelling was acquired with CH_4 as fuel and at atmospheric pressure. The implications of these simplifications should be investigated.

Regarding the modelling of pollutant emissions utilizing the automated clustering and CRN solving tool AGNES, it is recommended to:

- explore the use of AGNES further in order to understand and optimize clustering criteria;
- include effects of turbulent fluctuations. This can be done by clustering the computational cells based on fluctuation values and/or by employing a PaSR approach.

Regarding the evolution of minor species downstream the combustor outlet, the following can be suggested:

- the HPT must be included in the modelling in order to correctly predict pollutant emissions of modern gas turbines;
- the precision of the chemistry solver implemented in a CFD is a concern for this type of calculation. Small convergence tolerances must be imposed in order to achieve consistent solutions, which causes long computational times;
- experimental data is key to validate the modelling;
- including non-uniform inlet compositions and properties may cause different results and, therefore, it should be investigated;
- further investigation on the effect of cooling, taking into account the injection of air usually performed in stator vanes is recommended.

Appendix A Deactivated Reactions to Calculate NO_x Formation Pathways Contributions

The tables below shows the deactivated reaction for each chemical reaction mechanism employed for each reaction pathway. The overall guideline was to deactivate the least amount of reactions, prioritizing initiation reactions in order to impose less disturbance to the remainder of the mechanism. The error was estimated by summing the NO_x emissions obtained with each set of deactivated reactions and comparing the obtained value to that of the full mechanism.

A.1 GRI 2.11

Pathway	Reactions	
	GRI 2.11	
N_2O-Intermediate	$N_2O + OH \rightleftarrows N_2 + HO_2$	(184)
	$N_2O\ (+M) \rightleftarrows N_2 + O\ (+M)$	(185)
NNH	$NNH \rightleftarrows N_2 + H$	(204)
	$NNH\ (+M) \rightleftarrows N_2 + H\ (+M)$	(205)
	$NNH + O_2 \rightleftarrows HO_2 + N_2$	(206)
Prompt	$CH + N_2 \rightleftarrows HCN + N$	(240)
	$C + N_2 \rightleftarrows CN + N$	(239)
	$CH_2 + N_2 \rightleftarrows HCN + NH$	(242)
Reburning	$C + NO \rightleftarrows CN + O$	(244)
	$C + NO \rightleftarrows CO + N$	(245)
	$CH + NO \rightleftarrows HCN + O$	(246)
	$CH + NO \rightleftarrows H + NCO$	(247)
	$CH + NO \rightleftarrows HCO + N$	(248)
	$CH_2 + NO \rightleftarrows H + HNCO$	(249)
	$CH_2 + NO \rightleftarrows HCN + OH$	(250)
	$CH_2 + NO \rightleftarrows H + HCNO$	(251)
	$CH_2(S) + NO \rightleftarrows H + HNCO$	(252)
	$CH_2(S) + NO \rightleftarrows HCN + OH$	(253)
	$CH_3 + NO \rightleftarrows H_2O + HCN$	(255)
	$HCCO + NO \rightleftarrows CO + HCNO$	(274)
	$HO_2 + NO \rightleftarrows NO_2 + OH$	(186)
	$HO_2 + NO \rightleftarrows O_2 + HNO$	(216)
	$H + NO\ (+M) \rightleftarrows HNO\ (+M)$	(212)
	$NO + O\ (+M) \rightleftarrows NO_2\ (+M)$	(187)

	$NO_2 + O \rightleftarrows NO + O_2$	(188)
Thermal	$N + NO \rightleftarrows N_2 + O$	(178)
	$N + O_2 \rightleftarrows NO + O$	(179)
	$N + OH \rightleftarrows NO + H$	(180)

A.2 GRI 3.0

Pathway	Reactions	
N_2O-Intermediate	$N_2O + OH \rightleftarrows N_2 + HO_2$	(257)
	$N_2O\ (+M) \rightleftarrows N_2 + O\ (+M)$	(258)
NNH	$NNH \rightleftarrows N_2 + H$	(280)
	$NNH\ (+M) \rightleftarrows N_2 + H\ (+M)$	(281)
	$NNH + O_2 \rightleftarrows HO_2 + N_2$	(283)
Prompt	$CH + N_2 \rightleftarrows HCN + N$	(322)
	$C + N_2 \rightleftarrows CN + N$	(321)
	$CH_2 + N_2 \rightleftarrows HCN + NH$	(327)
Reburning	$C + NO \rightleftarrows CN + O$	(329)
	$C + NO \rightleftarrows CO + N$	(330)
	$CH + NO \rightleftarrows HCN + O$	(331)
	$CH + NO \rightleftarrows H + NCO$	(332)
	$CH + NO \rightleftarrows HCO + N$	(333)
	$CH_2 + NO \rightleftarrows H + HNCO$	(334)
	$CH_2 + NO \rightleftarrows HCN + OH$	(335)
	$CH_2 + NO \rightleftarrows H + HCNO$	(336)
	$CH_2(S) + NO \rightleftarrows H + HNCO$	(337)
	$CH_2(S) + NO \rightleftarrows HCN + OH$	(338)
	$CH_2(S) + NO \rightleftarrows H + HCNO$	(339)
	$CH_3 + NO \rightleftarrows H_2O + HCN$	(340)
	$CH_3 + NO \rightleftarrows H_2CN + OH$	(341)
	$HCCO + NO \rightleftarrows CO + HCNO$	(360)
	$HO_2 + NO \rightleftarrows NO_2 + OH$	(261)
	$HO_2 + NO \rightleftarrows O_2 + HNO$	(294)
	$H + NO\ (+M) \rightleftarrows HNO\ (+M)$	(289)
	$NO + O\ (+M) \rightleftarrows NO_2\ (+M)$	(262)
	$NO_2 + O \rightleftarrows NO + O_2$	(264)
Thermal	$N + NO \rightleftarrows N_2 + O$	(251)
	$N + O_2 \rightleftarrows NO + O$	(252)

	$N + OH \rightleftarrows NO + H$	(253)

A.3 KONNOV

Pathway	Reactions	
N_2O-Intermediate	$N_2O\ (+M) \rightleftarrows N_2 + O\ (+M)$	(60)
	$N_2O + O \rightleftarrows N_2 + O_2$	(61)
	$N_2O + O \rightleftarrows NO + NO$	(62)
	$N_2O + H \rightleftarrows N_2 + OH$	(134)
	$N_2O + H \rightleftarrows NH + NO$	(135)
NNH	$NNH \rightleftarrows N_2 + H$	(102)
	$NNH\ (+M) \rightleftarrows N_2 + H\ (+M)$	(103)
	$NNH + O_2 \rightleftarrows HO_2 + N_2$	(245)
	$NH + NH \rightleftarrows NNH + H$	(87)
	$NNH + H \rightleftarrows N_2 + H_2$	(104)
	$NNH + N \rightleftarrows N_2 + NH$	(105)
	$NNH + NH \rightleftarrows N_2 + NH_2$	(106)
	$NNH + NH_2 \rightleftarrows N_2 + NH_3$	(107)
	$NNH + NNH \rightleftarrows N_2H_2 + N_2$	(108)
	$N_2O + H \rightleftarrows NNH + O$	(136)
	$NNH + O \rightleftarrows N_2 + OH$	(243)
	$NNH + O \rightleftarrows NH + NO$	(222)
Prompt	$CH + N_2 \rightleftarrows NCN + H$	(1)
	$C + N_2 \rightleftarrows CN + N$	(1112)
	$N + N_2O \rightleftarrows NCN + NO$	(2)
	$NCN + H \rightleftarrows HCN + N$	(16)
	$NCN + O \rightleftarrows CN + NO$	(17)
	$NCN + OH \rightleftarrows HCN + NO$	(22)
	$NCN + OH \rightleftarrows HCN + NO$	(23)
	$NCN + O_2 \rightleftarrows NO + NCO$	(24)
	$NH2(+M) \rightleftarrows NH + H(+M)$	(90)
	$NH + H_2 \rightleftarrows NH_2 + H$	(91)

	$NH_3(+M) \rightleftarrows NH_2 + H(+M)$	(98)
	$NH_3 + H \rightleftarrows NH_2 + H_2$	(100)
	$HNNO + H \rightleftarrows NH_2 + NO$	(143)
	$HNO + O_2 \rightleftarrows NO + HO2$	(169)
	$HNO + NH \rightleftarrows NH_2 + NO$	(172)
	$HNO + NH_2 \rightleftarrows NH3 + NO$	(173)
	$NH3 + O \rightleftarrows NH_2 + OH$	(194)
	$NH3 + OH \rightleftarrows NH_2 + H_2O$	(195)
	$NH_2 + HO_2 \rightleftarrows NH3 + O_2$	(197)
	$NH_2 + O \rightleftarrows HNO + H$	(199)
	$NH_2 + O \rightleftarrows NH + OH$	(200)
	$NH_2 + OH \rightleftarrows NH + H_2O$	(201)
	$NH_2 + HO_2 \rightleftarrows H_2NO + OH$	(204)
	$NH_2 + O_2 \rightleftarrows HNO + OH$	(205)
	$NH_2 + O_2 \rightleftarrows H_2NO + O$	(206)
	$NH_2 + NO \rightleftarrows NNH + OH$	(207)
	$NH_2 + NO \rightleftarrows N_2 + H_2O$	(208)
	$NH_2 + NO_2 \rightleftarrows N_2O + H_2O$	(210)
	$NH_2 + NO_2 \rightleftarrows H_2NO + NO$	(211)
	$NH + O_2 \rightleftarrows HNO + O$	(218)
	$NH + O_2 \rightleftarrows NO + OH$	(219)
	$NH + NO \rightleftarrows N_2 + OH$	(223)
	$H_2NO + O_2 \rightleftarrows HNO + HO_2$	(259)
	$CH_2 + NO \rightleftarrows HCN + OH$	(1025)
	$HCN(+M) \rightleftarrows H + CN(+M)$	(1026)
	$C2 + N_2 \rightleftarrows CN + CN$	(1114)
	$H_2CN + O \rightleftarrows HCN + OH$	(1117)
	$CH + NO \rightleftarrows HCN + O$	(1127)
	$CH_2(S) + NO \rightleftarrows HCN + OH$	(1139)
	$HCNO \rightleftarrows HCN + O$	(1140)
	$HCNO + H \rightleftarrows HCN + OH$	(1141)
	$HCNH + O \rightleftarrows HCN + OH$	(1158)

	$CN + H_2O \rightleftarrows HCN + OH$	(1162)
	$OH + HCN \rightleftarrows HOCN + H$	(1164)
	$OH + HCN \rightleftarrows HNCO + H$	(1165)
	$OH + HCN \rightleftarrows NH_2 + CO$	(1166)
	$HCN + O \rightleftarrows NCO + H$	(1168)
	$HCN + O \rightleftarrows NH + CO$	(1169)
	$HCN + O \rightleftarrows CN + OH$	(1170)
	$CN + H_2 \rightleftarrows HCN + H$	(1171)
	$CN + O_2 \rightleftarrows NCO + O$	(1173)
	$HNCO + H \rightleftarrows H_2 + NCO$	(1181)
	$HNCO + H \rightleftarrows NH_2 + CO$	(1182)
	$HNCO + O \rightleftarrows NCO + OH$	(1184)
	$HNCO + O \rightleftarrows NH + CO_2$	(1185)
	$HNCO + O \rightleftarrows HNO + CO$	(1186)
	$HNCO + OH \rightleftarrows NCO + H_2O$	(1187)
	$HNCO + OH \rightleftarrows NH_2 + CO_2$	(1188)
	$NCO + H \rightleftarrows NH + CO$	(1193)
	$NCO + O \rightleftarrows NO + CO$	(1194)
	$NCO + NO \rightleftarrows N_2O + CO$	(1199)
	$NCO + NO \rightleftarrows N_2 + CO_2$	(1200)
	$NCO + O_2 \rightleftarrows NO + CO_2$	(1201)
Reburning	$C + NO \rightleftarrows CN + O$	(1126)
	$C + NO \rightleftarrows CO + N$	(1218)
	$CH + NO \rightleftarrows HCN + O$	(1127)
	$CH + NO \rightleftarrows H + NCO$	(1130)
	$CH_2 + NO \rightleftarrows H + HNCO$	(1131)
	$CH_2 + NO \rightleftarrows HCN + OH$	(1025)
	$CH_2 + NO \rightleftarrows H + HCNO$	(1132)
	$CH_2(S) + NO \rightleftarrows HCN + OH$	(1139)
	$CH_3 + NO \rightleftarrows H_2O + HCN$	(1135)
	$HCCO + NO \rightleftarrows CO + HCNO$	(1137)
	$HO_2 + NO \rightleftarrows NO_2 + OH$	(153)
	$HO_2 + NO \rightleftarrows O_2 + HNO$	(169)
	$H + NO\ (+M) \rightleftarrows HNO\ (+M)$	(164)
	$NO + O\ (+M) \rightleftarrows NO_2\ (+M)$	(65)

	$NO_2 + O \rightleftarrows NO + O_2$	(67)
Thermal	$N + NO \rightleftarrows N_2 + O$	(56)
	$N + O_2 \rightleftarrows NO + O$	(57)
	$N + OH \rightleftarrows NO + H$	(133)

A.4 GDF-KIN ® 3.0

Pathway	Reactions	
N_2O-Intermediate	$N_2O + OH \rightleftarrows N_2 + HO_2$	(776)
	$N_2O\ (+M) \rightleftarrows N_2 + O\ (+M)$	(778)
NNH	$NNH + H \rightleftarrows N_2 + H_2$	(740)
	$NNH\ (+M) \rightleftarrows N_2 + H\ (+M)$	(738)
	$NNH + OH \rightleftarrows N_2 + H_2O$	(741)
	$NNH + O \rightleftarrows N_2O + H$	(744)
Prompt	$CH + N_2 \rightleftarrows NCN + H$	(868)
	$C + N_2 \rightleftarrows CN + N$	(826)
	$CH_2 + N_2 \rightleftarrows HCN + NH$	(867)
Reburning	$C + NO \rightleftarrows CN + O$	(783)
	$CN + NO \rightleftarrows NCO + N$	(819)
	$CH + NO \rightleftarrows HCN + O$	(784)
	$CH_2 + NO \rightleftarrows HCN + OH$	(787)
	$CH_2 + NO \rightleftarrows H + HCNO$	(786)
	$CH_2(S) + NO \rightleftarrows HCN + OH$	(785)
	$CH_3 + NO \rightleftarrows H_2O + HCN$	(788)
	$HCCO + NO \rightleftarrows CO + HCNO$	(790)
	$HO_2 + NO \rightleftarrows NO_2 + OH$	(762)
	$HO_2 + NO \rightleftarrows O_2 + HNO$	(751)
	$H + NO\ (+M) \rightleftarrows HNO\ (+M)$	(764)
	$NO + O\ (+M) \rightleftarrows NO_2\ (+M)$	(769)
	$NO_2 + O \rightleftarrows NO + O_2$	(768)
Thermal	$N + NO \rightleftarrows N_2 + O$	(699)
	$N + O_2 \rightleftarrows NO + O$	(702)
	$N + OH \rightleftarrows NO + H$	(703)

A.5 POLIMI C1C3HT

Pathway	Reactions	
N_2O-Intermediate	$N_2O + OH \rightleftarrows N_2 + HO_2$	(815)
	$N_2O\ (+M) \rightleftarrows N_2 + O\ (+M)$	(809)
NNH	$NNH \rightleftarrows N_2 + H$	(643)
	$NNH + O_2 \rightleftarrows HO_2 + N_2$	(648)
Prompt	$CH + N_2 \rightleftarrows HCN + N$	(769)
	$C + N_2 \rightleftarrows CN + N$	(771)
	$CH_2 + N_2 \rightleftarrows HCN + NH$	(767)
Reburning	$C + NO \rightleftarrows CN + O$	(772)
	$C + NO \rightleftarrows CO + N$	(773)
	$CH + NO \rightleftarrows HCN + O$	(774)
	$CH + NO \rightleftarrows H + NCO$	(775)
	$CH + NO \rightleftarrows HCO + N$	(776)
	$CH_2 + NO \rightleftarrows H + HNCO$	(781)
	$CH_2 + NO \rightleftarrows HCN + OH$	(779)
	$CH_2 + NO \rightleftarrows H + HCNO$	(783)
	$CH_2(S) + NO \rightleftarrows H + HNCO$	(782)
	$CH_2(S) + NO \rightleftarrows HCN + OH$	(780)
	$CH_3 + NO \rightleftarrows H_2O + HCN$	(764)
	$HCCO + NO \rightleftarrows CO + HCNO$	(805)
	$HO_2 + NO \rightleftarrows NO_2 + OH$	(665)
	$HO_2 + NO \rightleftarrows O_2 + HNO$	(673)
	$H + NO\ (+M) \rightleftarrows HNO\ (+M)$	(669)
	$NO + O\ (+M) \rightleftarrows NO_2\ (+M)$	(666)
	$NO_2 + O \rightleftarrows NO + O_2$	(701)
Thermal	$N + NO \rightleftarrows N_2 + O$	(623)
	$N + O_2 \rightleftarrows NO + O$	(622)
	$N + OH \rightleftarrows NO + H$	(621)

BIBLIOGRAPHY

[1] IPCC, 2014: Climate Change 2014: Synthesis Report. Contribution of Working Groups I, II and III to the Fifth Assessment Report of the Intergovernmental Panel on Climate Change [Core Writing Team, R.K. Pachauri and L.A. Meyer (eds.)]. IPCC, Geneva, Switzerland, 151 pp.

[2] Cook J, Oreskes N, Doran PT, Anderegg WR, Verheggen B, Maibach EW, Carlton JS, Lewandowsky S, Skuce AG, Green SA, Nuccitelli D. Consensus on consensus: a synthesis of consensus estimates on human-caused global warming. Environmental Research Letters 2016;11(4):048002.

[3] United Nations Framework Convention on Climate Change. Report of the Conference of the Parties on its twenty-first session, held in Paris from 30 November to 13 December 2015. In Addendum. Part Two: Action taken by the Conference of the Parties at its twenty-first session. 2015.

[4] IPCC-SR15 Global Warming of 1.5 °C. Summary for Policymakers. 2018.

[5] International Energy Agency. CO_2 emissions from fuel combustion. 2017.

[6] Bellarby J, Foereid B, Hastings A. Cool Farming: Climate impacts of agriculture and mitigation potential. 2008.

[7] Garnett T. Where are the best opportunities for reducing greenhouse gas emissions in the food system (including the food chain)?. Food Policy 2011;36:S23-S32.

[8] Bauen A, Gomez I, Nanaki E, OudeNijeweme D, Paraschiv M, Schoentgen R. STRIA – Alternative Fuels. 2019.

[9] Lee DS, Fahey DW, Forster PM, Newton PJ, Wit RC, Lim LL, Owen B, Sausen R. Aviation and global climate change in the 21st century. Atmospheric Environment 2009;43(22-23):3520-3537.

[10] Dessens O, Köhler MO, Rogers HL, Jones RL, Pyle JA. Aviation and climate change. Transport Policy 2014;34:14-20.

[11] Kärcher B. Formation and radiative forcing of contrail cirrus. Nature Communications 2018;9(1):1824.

[12] Owen B, Lee DS, Lim L. Flying into the future: aviation emissions scenarios to 2050. Environmental Science and Technology 2010;44(7),2255-2260.

[13] Blanco GR, Gerlagh S, Suh J, Barrett HC, de Coninck CF, Diaz Morejon R, Mathur N, Nakicenovic A, Ofosu Ahenkora J, Pan H, Pathak J, Rice R, Richels SJ, Smith DI, Stern FL, Toth, and P. Zhou, 2014: Drivers, Trends and Mitigation. Climate Change 2014: Mitigation of Climate Change. Contribution of Working Group III to the Fifth Assessment Report of the Intergovernmental

Panel on Climate Change. Cambridge University Press, Cambridge, United Kingdom and New York, NY, USA.

[14] Chapman L. Transport and climate change: a review. Journal of Transport Geography 2007;15(5):354-367.i4

[15] Macintosh A, Wallace L. International aviation emissions to 2025: Can emissions be stabilised without restricting demand? Energy Policy 2009;37(1):264-273.

[16] Zhou W, Wang T, Yu Y, Chen D, Zhu B. Scenario analysis of CO_2 emissions from China's civil aviation industry through 2030. Applied Energy 2016;175:100-108.

[17] Gohardani AS, Doulgeris G, Singh R. Challenges of future aircraft propulsion: A review of distributed propulsion technology and its potential application for the all electric commercial aircraft. Progress in Aerospace Sciences 2011;47:369-391.

[18] Yin F, Rao AG. Performance analysis of an aero engine with interstage turbine burner. The Aeronautical Journal 2017;121:1605-1626.

[19] ICAO Engine Exhaust Emissions Databank, ICAO, Doc 9646- AN/943, Version 23, November 2016.

[20] Flightpath, A. C. A. R. E. 2050-Europe's Vision for Aviation. Advisory Council for Aeronautics Research in Europe, 2011.

[21] Klein M. Overview of worldwide ground-based regulatory framework. In: Lieuwen TC, Yang V, editors. Gas Turbine Emissions. New York: Cambridge University Press; 2013. p. 95-120.

[22] Nathan GJ, Jafarian M, Dally BB, Saw WL, Ashman PJ, Hu E, Steinfeld A. Solar thermal hybrids for combustion power plant: A growing opportunity. Progress in Energy and Combustion Science 2017;64,4-28.

[23] Brouwer AS, van den Broek M, Seebregts A, Faaij A. Impacts of large-scale intermittent renewable energy sources on electricity systems, and how these can be modelled. Renewable and Sustainable Energy Reviews 2014;33,443-466.

[24] Chen H, Cong TN, Yang W, Tan C, Li Y, Ding Y. Progress in electrical energy storage system: a critical review. Progress in Natural Science 2009;19,291-312.

[25] Overman N, Cornwell M, Gutmark EJ. Application of Flameless Combustion in gas turbine engines. 42nd AIAA/ASME/SAE/ASEE Joint Propulsion Conference & Exhibit; 2006 Jul 9-12; Sacramento, USA.

[26] Pompei F, Heywood JB. The role of mixing in burner-generated carbon moNO_xide and nitric oxide. Combustion and Flame 1972;19:407-418.

[27] Biagioli F, Güthe F. Effect of pressure and fuel–air unmixedness on NO_x emissions from industrial gas turbine burners. Combustion and Flame 2007;151:274-288.

[28] Dederichs S, Zarzalis N, Habisreuther P, Beck C, Prade B, Krebs W. Assessment of a gas turbine NO_x reduction potential based on a spatiotemporal unmixedness parameter. Journal of Engineering for Gas Turbines and Power 2013;135:1-8.

[29] Plessing T, Peters N, Wünning JG. Laseroptical investigation of highly preheated combustion with strong exhaust gas recirculation. Symposium (International) on Combustion 1998;27:3197-3204.

[30] Cavaliere A, de Joannon M. Mild Combustion. Progress in Energy and Combustion Science 2004;30:329-366.

[31] Li PF, Mi JC, Dally BB, Wang FF, Wang L, Liu ZH, Chen S, Zheng CG. Progress and recent trend in MILD combustion. Science China Technological Sciences 2011;54: 255-269.

[32] Wünning JA, Wünning JG. Flameless oxidation to reduce thermal NO-formation. Progress in Energy and Combustion Science 1997;23:81-84.

[33] Evans MJ, Medwell PR, Wu H, Stagni A, Ihme M. Classification and lift-off height prediction of non-premixed MILD and autoignitive flames. Proceedings of the Combustion Institute 2017;36:4297-4304.

[34] Rao AG, Levy Y. A new combustion methodology for low emission gas turbine engines. 8th International Symposium on High Temperature Air Combustion and Gasification; 2010 Jul 5-7; Pozan, Poland.

[35] Oberlack M, Arlitt R, Peters N. On stochastic Damköhler number variations in a homogeneous flow reactor. Combustion Theory and Modelling 2000;4:495-509.

[36] Goodwin G, Moffat HK, Speth RL. Cantera: an object-oriented software toolkit for chemical kinetics, thermodynamics, and transport processes. Version 2.3.0. doi:10.5281/zenodo.170284, http://www.cantera.org, 2017.

[37] Smith GP, Golden DM, Frenklach M, Moriarty NW, Eiteneer B, Goldenberg M, Bowman CT, Hanson RK, Song S, Gardiner Jr. WC, Lissianski VV, Qin Z. http://www.me.berkeley.edu/gri_mech/

[38] Galletti C, Parente A, Tognotti L. Numerical and experimental investigation of a mild combustion burner. Combustion and Flame 2007;151:649-664.

[39] Cabra R, Chen JY, Dibble RW, Karpetis AN, Barlow RS. Lifted methane-air jet flames in a vitiated coflow. Combustion and Flame 2005;143:491-506.

[40] Yoo CS, Sankaran R, Chen JH. Three-dimensional direct numerical simulation a of turbulent lifted hydrogen jet flame in heated coflow: flame stabilization and structure. Journal of Fluid Mechanics 2009;640:453-481.

[41] Borghi R. Turbulent combustion modelling. Progress in Energy and Combustion Science 1988;14:245-292.

[42] Peters N. Turbulent combustion. Cambridge University Press; 2000.

[43] Law CK. Combustion physics. Cambridge University Press; 2006.

[44] Derudi M, Villani A, Rota R. Sustainability of mild combustion of hydrogen-containing hybrid fuels. Proceedings of the Combustion Institute 2007;31:3393-3400.

[45] Tunçer O, Kaynaroğlu B, Karakaya MC, Kahraman S, Çetiner-Yıldırım O, Baytaş C. Preliminary investigation of a swirl stabilized premixed combustor. Fuel 2014;114,870-874.

[46] Li H, ElKady AM, Evulet AT. Effect of exhaust gas recirculation on NO_x formation in premixed combustion system. 47th AIAA Aerospace Sciences Meeting Including the New Horizons Forum and Aerospace Exposition; 2009 Jan 5-8; Orlando, USA.

[47] Ravi S, Morones A, Petersen EL. Effects of hydrogen addition on the flame speeds of natural gas blends under uniform turbulent conditions. ASME Turbo Expo 2015. Proceedings of ASME Turbo Expo; 2015 Jun 15-19; Montreal, Canada.

[48] Isaac BJ, Parente A, Galletti C, Thornock JN, Smith PJ, Tognotti L. A novel methodology for chemical time scale evaluation with detailed chemical reaction kinetics. Energy & Fuels 2013;27:2255-2265.

[49] Dally BB, Karpetis AN, Barlow RS. Structure of turbulent non-premixed jet flames in a diluted hot coflow. Proceedings of the Combustion Institute 2002;29:1147-1154.

[50] Li X, Dai Z, Wang F. Characteristic chemical time scale analysis of a partial oxidation flame in hot syngas coflow. Energy & Fuels 2017;31:4382-4390.

[51] McDonell V, Klein M. Ground-based gas turbine combustion: metrics, constraints, and system interactions. In: Lieuwen TC, Yang V, editors. Gas Turbine Emissions. New York: Cambridge University Press; 2013. p. 24-80.

[52] Lefebvre AH, Ballal DR. Gas turbine combustion: alternative fuels and emissions. Boca Raton: CRC press; 2010.

[53] Correa SM. A review of NO_x formation under gas-turbine combustion conditions. Combustion Science and Technology 1992;87:329-362.

[54] Vishwa Chandran NM. Combustion of hydrogen rich syngas fuels in gas turbines: an integrated modelling to address fuel flexibility issues [M.Sc. thesis]. Delft University of Technology; 2012.

[55] Rolls Royce plc. The jet engine. Chichester: John Wiley & Sons; 2015.

[56] Farokhi S. Aircraft propulsion. Chichester: John Wiley & Sons; 2009.

[57] Sander F, Carroni R, Rofka S, Benz E. Flue gas recirculation in a gas turbine: impact on performance and operational behavior. ASME Turbo Expo 2011. Proceedings of ASME Turbo Expo; 2011 Jun 6-11; Vancouver, Canada.

[58] American Society for Testing and Materials, Standard specification for diesel fuel oil, biodiesel blend (B6 to B20). In: Annual Book of ASTM Standards, ASTM International, West Conshohocken, PA, Method D7467, 2008.

[59] ICAO Airport Air Quality Manual, ICAO, Doc 9889, First Edition, 2011.

[60] The California Air Resources Board, Rule 2.34 stationary gas turbines, Revised November, 2014.

[61] Lückerath R, Meier W, Aigner M. FLOX® combustion at high pressure with different fuel compositions. Journal of Engineering for Gas Turbines and Power 2008;130:1-7.

[62] Veríssimo AS, Rocha AMA, Costa M. Operational, combustion, and emission characteristics of a small-scale combustor. Energy and Fuels 2011;25:2469-2480.

[63] Duwig C, Stankovic D, Fuchs L, Li G, Gutmark E. Experimental and numerical study of flameless combustion in a model gas turbine combustor. Combustion Science and Technology 2008;180:279-295.

[64] Lammel O, Schütz H, Schmitz G, Lückerath R, Stöhr M, Noll B, et al. FLOX® combustion at high power density and high flame temperatures. Journal of Engineering for Gas Turbines and Power 2010;132:1-10.

[65] Sadanandan R, Lückerath R, Meier W, Wahl C. Flame characteristics and emissions in flameless combustion under gas turbine relevant conditions. Journal of Propulsion and Power 2011;27:970-980.

[66] Schütz H, Lammel O, Schmitz G, Rödiger T, Aigner M. EZEE®: a high power density modulating FLOX® combustor. ASME Turbo Expo 2012. Proceedings of ASME Turbo Expo; 2012 Jun 11-15; Copenhagen, Denmark.

[67] Roediger T, Lammel O, Aigner M, Beck C, Krebs W. Part-load operation of a piloted FLOX® combustion system. Journal of Engineering for Gas Turbines and Power 2013;135:1-9.

[68] Zanger J, Monz T, Aigner M. Experimental investigation of the combustion characteristics of a double-staged FLOX®-based combustor on an atmospheric and a micro gas turbine test rig. ASME Turbo Expo 2015. Proceedings of ASME Turbo Expo; 2015 Jun 15-19; Montreal, Canada.

[69] Guillou E, Cornwell M, Gutmark E. Application of "flameless" combustion for gas turbine engines. 47th AIAA Aerospace Sciences Meeting Including The New Horizons Forum and Aerospace Exposition; 2009 Jan 5-8; Orlando, USA.

[70] Zizin A, Lammel O, Severin M, Ax H, Aigner M. Development of a jet-stabilized low-emission combustor for liquid fuels. ASME Turbo Expo 2015. Proceedings of ASME Turbo Expo; 2015 Jun 15-19; Montreal, Canada.

[71] Gounder JD, Zizin A, Lammel O, Aigner M. Spray characteristics measured in a new FLOX® based low emission combustor for liquid fuels using laser and

optical diagnostics. ASME Turbo Expo 2016. Proceedings of ASME Turbo Expo; 2016 Jun 13-17; Seoul, South Korea.

[72] Gounder JD, Zizin A, Lammel O, Rachner M, Aigner M, Kulkarni SR. Experimental and numerical investigation in a new FLOX® based combustor for liquid fuels for Micro Gas Turbine Range Extender (MGT-REX). AIAA Propulsion and Energy Forum 2016. 52nd AIAA/SAE/ASEE Joint Propulsion Conference; 2016 Jul 25-27; Salt Lake City, USA.

[73] Arghode VK, Gupta AK. Role of thermal intensity on operational characteristics of ultra-low emission colorless distributed combustion. Applied Energy 2013;111:930-956.

[74] Lammel O, Stöhr M, Kutne P, Dem C, Meier W, Aigner M. Experimental analysis of confined jet flames by laser measurement techniques. Journal of Engineering for Gas Turbines and Power 2012;134:1-9.

[75] Yin Z, Boxx I, Stöhr M, Lammel O, Meier W. Confinement-induced instabilities in a jet-stabilized gas turbine model combustor. Flow, Turbulence and Combustion 2016;98:217-235.

[76] Severin M, Lammel O, Meier W, Aigner M. Flame stabilization regimes of lean premixed confined jet flames at different Reynolds numbers. AIAA Propulsion and Energy Forum. 53rd AIAA/SAE/ASEE Joint Propulsion Conference; 2017 Jul 10-12; Atlanta, USA.

[77] Levy Y, Sherbaum V, Arfi P. Basic thermodynamics of FLOXCOM, the low-NO_x gas turbines adiabatic combustor. Applied Thermal Engineering 2004;24:1593-1605.

[78] Levy Y, Sherbaum V, Erenburg V. Fundamentals of low-NO_x gas turbine adiabatic combustor. Proceedings of ASME Turbo Expo 2005, June 6-9th 2005, USA, 2005.

[79] Levy Y, Sherbaum V, Erenburg V. The role of the recirculating gases in the MILD combustion regime formation. ASME Turbo Expo 2007. Proceedings of ASME Turbo Expo; 2007 May 14-17; Montreal, Canada.

[80] Melo MJ, Sousa JMM, Costa M, Levy Y. Experimental investigation of a novel combustor model for gas turbines. Journal of Propulsion and Power 2009;25:609-617.

[81] Melo MJ, Sousa JMM, Costa M, Levy Y. Flow and combustion characteristics of a low-NO_x combustor model for gas turbines. Journal of Propulsion and Power 2011;27:1212-1217.

[82] Levy Y, Rao AG, Sherbaum V. Preliminary analysis of a new methodology for flameless combustion in gas turbine combustors. ASME Turbo Expo 2007. Proceedings of ASME Turbo Expo; 2007 May 14-17; Montreal, Canada.

[83] Levy Y, Rao AG, Sherbaum V. Chemical kinetic and thermodynamics of flameless combustion methodology for gas turbine combustors. 43rd

AIAA/ASME/SAE/ASEE Joint Propulsion Conference & Exhibit; 2007 June 8-11; Cincinnati, USA.

[84] Levy Y, Christo FC, Gaissinski I, Erenburg V, Sherbaum V. Design and performance analysis of a gas turbine flameless combustor using CFD simulations. ASME Turbo Expo 2012. Proceedings of ASME Turbo Expo; 2012 Jun 11-15; Copenhagen, Denmark.

[85] Joos F, Brunner P, Schulte-Werning B, Syed K. Development of the sequential combustion system for the ABB GT24/GT26 gas turbine family. International Gas Turbine and Aeroengine Congress & Exhibition; 1996 Jun 11-15; Birmingham, UK.

[86] Rao AG, Yin F, van Buijtenen JP. A hybrid engine concept for multi-fuel blended wing body. Aircraft Engineering and Aerospace Technology: An International Journal 2014;86:483-493.

[87] Yin F, Rao AG. Off-design performance of an interstage turbine burner turbofan engine. Journal of Engineering for Gas Turbine and Power 2017;139:1-8.

[88] Levy Y, Erenburg V, Sherbaum V, Gaissinski I. Flameless oxidation combustor development for a sequential combustion hybrid turbofan engine. ASME Turbo Expo 2016. Proceedings of ASME Turbo Expo; 2016 Jun 13-17; Seoul, South Korea.

[89] Vaz DC, Borges ARJ, van Buijtenen JP, Spliethoff H. On the stability range of a cylindrical combustor for operation in the FLOX regime. ASME Turbo Expo 2004. Proceedings of ASME Turbo Expo; 2004 Jun 14-17; Vienna, Austria.

[90] Li G, Gutmark EJ, Overman N, Cornwell M, Stankovic D, Fuchs L, Vladimir M. Experimental study of a flameless gas turbine combustor. ASME Turbo Expo 2006. Proceedings of ASME Turbo Expo; 2006 May 8-11; Barcelona, Spain.

[91] Vaz DC. Towards the application of flameless combustion to micro gas turbines [Ph.D. thesis]. Universidade Nova de Lisboa; 2007.

[92] Zhou Z, Xiong Y, Huang M, Zhang Z, Xiao Y. Experimental and numerical investigations of a MILD combustor applied for gas turbune. ASME Turbo Expo 2016. Proceedings of ASME Turbo Expo; 2016 Jun 13-17; Seoul, South Korea.

[93] Seliger H, Stöhr M, Yin Z, Huber A, Aigner M. Experimental and numerical analysis of a FLOX®-based combustor for a 3 kW micro gas turbine under atmospheric conditions. ASME Turbo Expo 2017. Proceedings of ASME Turbo Expo; 2017 Jun 26-30; Charlotte, USA.

[94] Bilger RW, Pope SB, Bray KNC, Driscoll JF. Paradigms in turbulent combustion research. Proceedings of the Combustion Institute 2005;30:21-42.

[95] van Oijen JA, de Goey PH. Modelling of premixed laminar flames using flamelet-generated manifolds. Combustion Science and Technology 2000;161:113-137.

[96] Pierce CD, Moin P. Progress-variable approach for large-eddy simulation of non-premixed turbulent combustion. Journal of Fluid Mechanics 2004;504:73-97.

[97] Abtahizadeh E, de Goey P, van Oijen J. LES of Delft Jet-in-Hot Coflow burner to investigate the effect of preferential diffusion on autoignition of CH4/H2 flames. Fuel 2017;191:36-45.

[98] Abtahizadeh E, de Goey P, van Oijen J. Development of a novel flamelet-based model to include preferential diffusion effects in autoignition of CH4/H2 flames. Combustion and Flame 2015;162:4358-4369.

[99] Minamoto Y, Dunstan TD, Swaminathan N, Cant RS. DNS of EGR-type turbulent flame in MILD condition. Proceedings of the Combustion Institute 2013;34:3231-3238.

[100] Minamoto Y, Swaminathan N, Cant RS, Leung T. Reaction zones and their structure in MILD combustion. Combustion Science and Technology 2014;186:1075-1096.

[101] Klimenko AY, Bilger RW. Conditional moment closure for turbulent combustion. Progress in Energy and Combustion Science 1999;25:595-687.

[102] Labahn JW, Dovizio D, Devaud CB. Numerical simulation of the Delft-Jet-in-Hot-Coflow (DJHC) flame using conditional source-term estimation. Proceedings of the Combustion Institute 2015;35:3547-3555.

[103] Haworth DC. Progress in probability density function methods for turbulent reacting flows. Progress in Energy and Combustion Science 2010;36:168–259.

[104] Lyra S, Cant RS. Analysis of high pressure premixed flames using Equivalent Reactor Networks. Fuel 2013;107:261-268.

[105] Park J, Nguyen TH, Joung D, Huh KY, Lee, MC. Prediction of NO_x and CO emissions from an industrial lean-premixed gas turbine combustor using a chemical reactor network model. Energy & Fuels 2013;27:1643-1651.

[106] Lebedev AB, Secundov AM, Starik AM, Titova NS, Schepin AM. Modeling study of gas-turbine combustor emission. Proceedings of the Combustion Institute 2009;32:2941-2947.

[107] Starik AM, Kozlov VE, Lebedev AB, Titova NS. Application of reactor net models for the simulation of gas-turbine combustor emissions. International Journal of Sustainable Aviation 2014;1(1):43-57.

[108] Nicol DG, Steele RC, Marinov NM, Malte PC. In The importance of the nitrous oxide pathway to NO_x in lean-premixed combustion, ASME International Gas Turbine and Aeroengine Congress and Exposition, Cincinnati, USA, May 24-27, 1993.

[109] Guethe F, García MC, Burder A. Flue gas recirculation in gas turbine: investigation of combustion reactivity and NO_x emission. Proceedings of ASME Turbo Expo; 2009 Jun 8-12; Orlando, USA.

[110] Modest MF. The weighted-sum-of-grey-gases model for arbitrary solution methods in radiative transfer. Journal of Heat Transfer 1991;113:650-656.

[111] Coelho PJ, Mancini M, Roekaerts DJEM. 'Thermal Radiation', in Vervisch, L, Roekaerts, D.J.E.M. (ed.) Best Practice Guidelines for Computational Fluid Dynamics of Turbulent Combustion. ERCOFTAC. 2015:77-144.

[112] Magnussen BF, Hjertager BH. On mathematical modeling of turbulent combustion with special emphasis on soot formation and combustion. In Symposium (international) on Combustion 1977;16(1):719-729.

[113] Gran IR, Magnussen BF. A numerical study of a bluff-body stabilized diffusion flame. Part 1. Influence of turbulence modeling and boundary conditions. Combustion Science and Technology 1996;119:171-190.

[114] Reichel TG, Terhaar, S, Paschereit CO. Increasing flashback resistance in lean premixed swirl-stabilized hydrogen combustion by axial air injection. Journal of Engineering for Gas Turbines and Power 2015;137(7):071503.

[115] Reichel TG, Paschereit CO. Interaction mechanisms of fuel momentum with flashback limits in lean-premixed combustion of hydrogen. International Journal of Hydrogen Energy 2017;42(7):4518-4529.

[116] Reichel TG, Terhaar S, Paschereit CO. Flashback Resistance and Fuel–Air Mixing in Lean Premixed Hydrogen Combustion. Journal of Propulsion and Power 2017;34(3):690-701.

[117] Talboom MG. Chemical kinetics study of the Hybrid combustion system. Master of Sciences Thesis, Delft University of Technology, 2016.

[118] Levy Y, Sherbaum V, Erenburg V, Krapp V, Paschereit CO, Göke S, Reichel T, Grey J. Chemical kinetics of the hybrid combustion system – Deliverable 2.1. Advanced Hybrid Engines for Aircraft Development, 2012.

[119] Rao AG, Bhat A. Hybrid combustion system for future aero engines, Proceedings of the 2nd National Propulsion Conference; 2015 Feb 23-24; Bombay, India.

[120] Visser WP, Broomhead MJ. GSP, a generic object-oriented gas turbine simulation environment. Proceedings of ASME Turbo Expo; 2000 May 8-11; Munich, Germany.

[121] Lukachko SP, Waitz IA, Miake-Lye RC, Brown RC, Anderson MR. Production of sulfate aerosol precursors in the turbine and exhaust nozzle of an aircraft engine. Journal of Geophysical Research: Atmospheres 1998;103(D13):16159-16174.

[122] Starik AM, Savel'ev AM, Titova NS, Schumann U. Modeling of sulfur gases and chemiions in aircraft engines. Aerospace Science and Technology 2002;6(1):63-81.

[123] Moniruzzaman CG, Yu F. A 0D aircraft engine emission model with detailed chemistry and soot microphysics. Combustion and Flame 2012;159(4):1670-1686.

[124] Wey CC, Anderson BA, Wey C, Miake-Lye RC, Whitefield P, Howard R. Overview on the aircraft particle emissions experiment (APEX). Journal of Propulsion and Power 2007;23(5):898-905.

[125] Bisson J, Seers P, Huegel M, Garnier F. Numerical prediction of gaseous aerosol precursors and particles in an aircraft engine. Journal of Propulsion and Power 2016;32(1):918-928.

[126] Nguyen TH, Nguyen-Tri P, Vancassel X, Garnier F. 2018. Aero-thermodynamic and chemical process interactions in an axial high-pressure turbine of aircraft engines. International Journal of Engine Research 2018; 20(6).

[127] Timko LP. Energy Efficient Engine high pressure turbine component test performance report. Technical Report No. NASA CR-168289, NASA Lewis Research Center 1984.

[128] Murari S, Sunnam S, Liu JS. Steady state and transient CFD studies on aerodynamic performance validation of a high pressure turbine. Proceedings of ASME Turbo Expo; 2012 Jun 11-15; Copenhagen, Denmark.

[129] Zhang Q, Xu H, Wang J, Li G, Wang L, Wu X, Ma S. Evaluation of CFD predictions using different turbulence models on a film cooled guide vane under experimental conditions. Proceedings of ASME Turbo Expo; 2015 Jun 15-19; Montreal, Canada.

[130] Celik IB, Ghia U, Roache PJ, Freitas CJ, Coleman H, Raad PE. Procedure for estimation and reporting of uncertainty due to discretization in CFD applications. Journal of Fluids Engineering, 2008;130(7).

[131] Efimov DV, de Goey P, van Oijen JA. FGM with REDx: chemically reactive dimensionality extension. Combustion Theory and Modelling, 2018;22(6):1103-1133.

[132] “Chemical-Kinetic Mechanisms for Combustion Applications", San Diego Mechanism web page, Mechanical and Aerospace Engineering (Combustion Research), University of California at San Diego (http://combustion.ucsd.edu)

[133] Frassoldati A, Faravelli T, Ranzi E. A wide range modelling study of NO_x formation and nitrogen chemistry in hydrogen combustion. International Journal of Hydrogen Energy 2006;31(15):2310-2328.

[134] Reaction Design, 2011. CHEMKIN Tutorials Manual CHEMKIN® Software. 10112/15112.

[135] Yin F. Modeling and Characteristics of a Novel Multi-Fuel Hybrid Engine for Future Aircraft [PhD Thesis]. Delft University of Technology; 2016.

[136] Glarborg P, Bentzen LL. Chemical effects of a high CO2 concentration in oxy-fuel combustion of methane. Energy & Fuels 2007;22(1):291-296.

[137] Myhrvold T. Combustion Modeling in Turbulent Boundary-Layer Flows [PhD Thesis]. Norwegian University of Science and Technology; 2003.

[138] Levy Y, Reichel TG. Feasibility of the hybrid combustion concept. Advanced Hybrid Engines for Aircraft Development – Deliverable 2.7: December, 2014.

[139] Tu Y, Su K, Liu H, Wang Z, Xie Y, Zheng C, Li W. MILD combustion of natural gas using low preheating temperature air in an industrial furnace. Fuel Processing Technology 2017;156:72-81.

[140] Dally BB, Riesmeier E, Peters N. Effect of fuel mixture on moderate and intense low oxygen dilution combustion. Combustion & Flame 2004;137:418-431.

[141] Loenen E, van der Tempel L. Determination of absorption coefficients of glasses at high temperatures, by measuring the thermal emission; Philips Research – Unclassified Report 020/96, 1996.

[142] Zimont V, Polifke W, Bettelini M, Weisenstein W. An efficient computational model for premixed turbulent combustion at high Reynolds numbers based on a turbulent flame speed closure. Proceedings of ASME International Gas Turbine and Aeroengine Congress and Exposition; 1997 Jun 2-5; Orlando, USA.

[143] Bowman CT, Hanson RK, Davidson DF, Gardiner Jr. WC, Lissianski V, Smith GP, Golden DM, Frenklach M, Goldenberg M. http://www.me.berkeley.edu/gri_mech/

[144] Lee KW, Choi DH. Prediction of NO in turbulent diffusion flames using Eulerian particle flamelet model. Combustion Theory and Modelling 2008;12: 905-927.

[145] Barlow RS, Karpetis AN, Frank JH, Chen J-Y. Scalar profiles and NO formation in laminar opposed-flow partially premixed methane/air flames. Combustion & Flame 2001;127:2102-2118.

[146] Kim SH, Huh KY, Dally BB. Conditional moment closure modeling of turbulent nonpremixed combustion in diluted hot coflow. Proceeding of the Combustion Institute 2005;30:751-757.

[147] Nicolle A, Dagaut P. Occurrence of NO-reburning in MILD combustion evidenced via chemical kinetic modeling. Fuel 2006;85:2469-2478.

[148] Hewson JC, Bollig M. Reduced mechanisms for NO_x emissions from hydrocarbon diffusion flames. Proceedings of the International Combustion Symposium 1996;26:2171-2179.

[149] Zhao D, Yamashita H, Kitagawa K, Arai N, Furuhata T. Behavior and effect on NO_x formation of OH radical in methane-air diffusion flame with steam addition. Combustion & Flame 2002;130:352-360.

[150] Mancini M, Schwöppe P, Weber R, Orsino S. On mathematical modelling of flameless combustion. Combustion & Flame 2007;150:54-59.

[151] Li P, Wang F, Mi J, Dally BB, Mei Z, Zhang J, Parente A. Mechanisms of NO formation in MILD combustion of CH4/H2 fuel blends. International Journal of Hydrogen Energy 2014;39:19187-19203.

[152] Glarborg P, Miller JA, Ruscic B, Klippenstein SJ. Modeling nitrogen chemistry in combustion. Progress in Energy and Combustion Science 2018;67:31-68.

[153] Rink KK, Lefebvre AH. Influence of fuel composition and spray characteristics on nitric oxide formation. Combustion Science and Technology 1989;68:1-14.

[154] Sorrentino G, Sabia P, De Joannon M, Bozza P, Ragucci R. Influence of preheating and thermal power on cyclonic burner characteristics under mild combustion. Fuel 2018;233:207-214.

[155] Konnov AA. Detailed reaction mechanism for small hydrocarbons combustion, Release 0.5, 2000.

[156] Pillier L, Desgroux P, Lefort B, Gasnot L, Pauwels JF, Da Costa I. NO prediction in natural gas flames using GDF-Kin® 3.0 mechanism NCN and HCN contribution to prompt-NO formation. Fuel 2006;85(7-8):896-909.

[157] Ranzi E, Frassoldati,A, Grana R, Cuoci A, Faravelli T, Kelley AP, Law CK. Hierarchical and comparative kinetic modeling of laminar flame speeds of hydrocarbon and oxygenated fuels. Progress in Energy and Combustion Sciences 2012;38(4):468-501.

[158] Konnov AA. Implementation of the NCN pathway of prompt-NO formation in the detailed reaction mechanism. Combustion & Flame 2009;156(11):2093-2105.

[159] Galletti C, Ferrarotti M, Parente A, Tognotti L. Reduced NO formation models for CFD simulations of MILD combustion. International Journal of Hydrogen Energy 2015;40(14):4884-4897.

[160] Prakash V, Steimes J, Roekaerts DJEM, Klein SA. Modelling the effect of external flue gas recirculation on NO_x and CO emissions in a premixed gas turbine combustor with chemical reactor networks. Proceedings of ASME Turbo Expo; 2018 Jun 11-15; Oslo, Norway.

[161] Minamoto Y, Swaminathan N. Scalar gradient behaviour in MILD combustion. Combustion and Flame 2014;161(4):1063-1075.

[162] Benedetto D, Pasini S, Falcitelli M., La Marca C, Tognotti L. (2000). Emission Prediction from 3-D Complete Modelling to Reactor Network Analysis. Combustion Science and Technology 2000;153:279-294.

[163] Faravelli T, Bua L, Frassoldati A, Antifora A, Tognotti L, Ranzi E. A new procedure for predicting NO_x emissions from furnaces. Computers & Chemical Engineering 2001;25:613-618.

[164] Falcitelli M, Tognotti L, Pasini S. An algorithm for extracting chemical reactor network models from CFD simulation of industrial combustion systems. Combustion Science and Technology, 2002;174(11-12):27-42.

[165] Frassoldati A, Frigerio S, Colombo E, Inzoli F, Faravelli T. Determination of NO_x emissions from strong swirling confined flames with an integrated CFD-based procedure. Chemical Engineering Science 2005;60(11):2851-2869.

[166] Fichet V, Kanniche M, Plion P, Gicquel O. A reactor network model for predicting NO_x emissions in gas turbines. Fuel 2010;89(9):2202-2210.

[167] Monaghan RF, Tahir R, Cuoci A, Bourque G, Füri M, Gordon RL, Faravelli T, Frassoldati A, Curran HJ. Detailed multi-dimensional study of pollutant formation in a methane diffusion flame. Energy & Fuels 2012;26(3):1598-1611.

[168] Cuoci A, Frassoldati A, Stagni A, Faravelli T, Ranzi E, Buzzi-Ferraris G. Numerical modeling of NO_x formation in turbulent flames using a kinetic post-processing technique. Energy & Fuels 2013;27:1104-1122.

[169] Sampat RP. Automatic Generation of Chemical Reactor Networks for Combustion Simulations [Master of Sciences Thesis]. Delft University of Technology; 2018.

[170] Yousefian S, Bourque G, Monaghan RF, 2017, June. Review of hybrid emissions prediction tools and uncertainty quantification methods for gas turbine combustion systems. American Society of Mechanical Engineers Digital Collection. Proceedings of ASME Turbo Expo; 2017 Jun 26-30; Charlotte, USA.

[171] Hosseini SE, Wahid MA. Biogas utilization: experimental investigation on biogas flameless combustion in lab-scale furnace. Energy Conversion and Management 2013;74:426-432.

[172] Zhou B, Costa M, Li Z, Aldén M, Bai XS. Characterization of the reaction zone structures in a laboratory combustor using optical diagnostics: from flame to flameless combustion. Proceedings of the Combustion Institute 2017;36(3):4305-4312.

[173] Lamouroux J, Ihme M, Fiorina B, Gicquel O. Tabulated chemistry approach for diluted combustion regimes with internal recirculation and heat losses. Combustion and Flame 2014;161(8):2120-2136.

[174] Verhoeven LM, Ramaekers WJS, van Oijen JA, de Goey LPH. Modeling non-premixed laminar co-flow flames using flamelet-generated manifolds. Combustion and Flame 2012;159(1):230-241.

[175] van Oijen JA. Modeling of turbulent premixed flames using flamelet-generated manifolds. In Modeling and Simulation of Turbulent Combustion (pp. 241-265) 2018;Springer, Singapore.
[176] Pope SB. An explanation of the turbulent round-jet/plane-jet anomaly. AIAA Journal 1978;16(3):279-281.
[177] Shih TH, Liou WW, Shabbir A, Yang Z, Zhu J. A new k-ϵ eddy viscosity model for high Reynolds number turbulent flows. Computers & Fluids 1995;24(3):227-238.
[178] Huang X, Tummers MJ, Roekaerts DJEM. Experimental and numerical study of MILD combustion in a lab-scale furnace. Energy Procedia 2017;120:395-402.
[179] Ramaekers WJS, van Oijen JA, de Goey LPH. A priori testing of flamelet generated manifolds for turbulent partially premixed methane/air flames. Flow, turbulence and combustion 2010;84(3):439-458.
[180] Fortunato V, Mosca G, Lupant D, Parente A. Validation of a reduced NO formation mechanism on a flameless furnace fed with H_2-enriched low calorific value fuels. Applied Thermal Engineering 2018;144:877-889.

ACKNOWLEDGEMENTS

The first person I need to thank is my promotor and supervisor, Arvind. I appreciate your friendly and open approach to supervision and I believe that we were able to cooperate in a very nice fashion. Thank you for always be willing to help me out and for your friendship.

My gratitude and admiration for Prof. Dirk Roekaerts certainly has to be highlighted. Your profound knowledge, commitment to education and constructive criticism, the honest and measured comments are admirable. The fact that you have been a part of my PhD has been a privilege, and being your co-author is an honour. I see you as a role-model for academics, researchers and mentors in general.

I also need to acknowledge and thank the contribution of Prof. Piero Colonna. Being my co-promotor, you had useful inputs during our meetings and also provided valuable comments that improved this thesis.

The committee selected to evaluate this thesis has also contributed with valuable comments and criticism. I am grateful for the participation of such highly respected experts.

I appreciate the efforts of Martijn and Nando in translating my propositions and summary to Dutch.

The effort and dedication of the master students I've worked with during my PhD was also important. Rishikesh, Stefan, Melchior, Cristian, Thijs, Maaike, Stella, Sneha, and Fernando, thank you. Some of you directly contributed to this thesis. Special thanks to Rishikesh for all the help he provided and discussions we have had.

I should acknowledge all the colleagues and friends I shared office with in the past years. Going through the risk of forgetting some people, thank you: Adam, Andrea, Antonio, Federica, Federico, Feijia, Francesco, Imco, Josh, Leonardo, Lex, Lucia, Matteo, Nando, Nitish2, Salvo, Sebastian and Stefano. Special thanks to Adam, Nando, Nitish and Sebastian for all the commiseration and self-loathing. You guys made the work environment be less about work, and that is positive.

I also need to thank everyone who went bouldering or climbing with me. These activities helped me maintain a socially acceptable level of sanity, which was fundamental to complete this thesis. Therefore, Federico, Josh, Maurice, Martijn, Nando, Reynard, Riccardo, Sonia, Sumit, and Tom, thanks a lot.

I am also thankful for the friendships, some of them relatively recent, and others from the previous century. You all have somehow participated and helped creating memorable moments in the past years. Felipe, Paula, Di, Pedro, Ca, Kholo, Seto, Max and Robin, you are all part of it.

Finally, my family has to receive a big part of my gratitude. My parents, for their continuous support and willingness to help even from distance. Your support was very important to me. Lis and Âmbar, you have been a daily support, and a source of smiles, laughs and extraordinary moments. Thank you for your patience and sweetness, and for embarking with me in yet another adventure.

PUBLICATIONS RELATED TO THIS THESIS

Perpignan AAV, Gangoli Rao A, Roekaerts DJEM. Flameless combustion and its potential towards gas turbines. Progress in Energy & Combustion Science 2018;69:28-62.

Perpignan AAV, Talboom MG, Yeshayahou L, Gangoli Rao A. Emission modeling of an interturbine burner based on flameless combustion. Energy & Fuels 2018;32(1):822-838.

Perpignan AAV, Gangoli Rao A. Effects of chemical reaction mechanism and NO_x formation pathways on an inter-turbine burner. The Aeronautical Journal 2019;123(1270):1898-1918.

Perpignan AAV, Sampat R, Gangoli Rao A. Modelling pollutant emissions of Flameless Combustion with a joint CFD and Chemical Reactor Network approach. Frontiers in Mechanical Engineering 2019;5(63).

Perpignan AAV, Tomasello SG, Gangoli Rao A. Evolution of minor chemical species in a gas turbine stator. Submitted to Applied Energy.

CURRICULUM VITAE

2020 – present	R&D Engineer *Siemens HTT, Zoeterwoude, The Netherlands*
2019 – 2020	Researcher *Delft University of Technology, Delft, The Netherlands*
2015 – 2019	PhD Candidate Thesis: Emission modelling from a multi-fuel dual combustor gas turbine *Delft University of Technology, Delft, The Netherlands*
2013 – 2014	Simulations Engineer CFD and FEA related to the cement, mining and food industries *Dynamis Mecânica Aplicada Ltda, São Paulo, Brazil*
2011 – 2013	MSc in Mechanical Engineering Thesis: Development of a radial compressor for a small-scale gas turbine *University of São Paulo, São Paulo, Brazil*
2011 – 2013	MBA in Quality Management and Engineering Thesis: Application of Design for Six Sigma to the conceptual and preliminary design of gas turbines *University of São Paulo, São Paulo, Brazil*
2010	Engineering Intern Internal combustion engine calibration and control *Ford Motor Company, Tatuí, Brazil*
2006 – 2010	Aeronautical Engineering (Brazilian Degree BA + MSc) Thesis: Laminar fuselage CFD study *University of São Paulo, São Carlos, Brazil*